# Astrophysical Laboratories and Advanced Imaging Techniques for Testing Stellar Models:
# Eclipsing Binaries, High Contrast Imaging, and Optical Interferometry

By

E. Victor Garcia

Dissertation

Submitted to the Faculty of the

Graduate School of Vanderbilt University

in partial fulfillment of the requirements

for the degree of

DOCTOR OF PHILOSOPHY

in

PHYSICS

May, 2016

Nashville, Tennessee

Approved:

Professor Keivan Stassun

Dr. Gerard van Belle

Professor Andreas Berlind

Professor Kelly Holley-Bocklemann

Professor Robert Scherrer

TABLE OF CONTENTS

LIST OF TABLES

LIST OF FIGURES

# CHAPTER I

# INTRODUCTION AND BACKGROUND

## 1.1 A brief summary of this dissertation

This dissertation is about testing stellar formation, evolution, stellar structure and atmosphere models.

Chapter II is on testing stellar evolution models (see §1.3 below) by analyzing 40 years of time series photometry and spectroscopy of eclipsing binary V578 Mon. Chapter III is on testing brown dwarf formation models (§1.2) by imaging young brown dwarfs in the Pleiades open cluster.

In Chapter IV, and summarized in §1.4 below, I detail the commissioning of the Visible Imaging System for Interferometric Observations at NPOI (VISION), a new visible-light interferometric beam combiner for the Navy Precision Optical Interferometer (NPOI). VISION promises to obtain the first direct images of main sequence stars at visible wavelengths other than the Sun.

## 1.2 Chapter II: Testing 1D Stellar Evolution and Structure Models with Observations of Eclipsing Binaries

Eclipsing binaries (EBs) are spectroscopic binary stars that have their orbit aligned such that they eclipse each other as viewed from Earth. EBs are ideal laboratories to

test 1D stellar evolution and stellar structure models. This is because EBs allow us to directly measure:

- radii for both the primary (hotter) and secondary (cooler) star from the primary and secondary eclipse durations of the light curve,
- masses for both stars from observations of radial velocity motion, and
- temperatures from spectral disentangling techniques and depths of the light curve eclipses.

EBs can serve as anchor points on which stellar evolution models are calibrated (see review by Torres et al., 2010).

As detailed in Chapter II and published in Garcia et al. (2011, 2013, 2014), we measured the masses, radii, temperatures, and rotational velocities of detached benchmark eclipsing binary V578 Mon. We combined 40 years of time series photometry spanning one full apsidal motion period ($\approx$ 35 yrs) of the binary V578 Mon with high resolution ($R \approx 85000$) spectroscopy to obtain stellar parameters of V578 Mon to within $\lesssim$ %2 accuracy. We compared the absolute dimensions of V578 Mon to 1D stellar evolution and structure models using the isochrone and apsidal motion test.

We performed the isochrone test on V578 Mon, which requires that the ages of both components of a detached eclipsing binary predicted from separate stellar evolution tracks be the same within the uncertainty of the absolute dimensions ($M$, $R$, $T_{\rm eff}$, $v_{\rm rot}$). Here we assume that both components of the eclipsing binary likely

formed at the same time in a single gas cloud. We compared the absolute dimensions of V578 Mon to the rotating and non-rotating models from several groups. Models with larger convective overshoot, $\alpha_{\rm ov} > 0.35$.

V578 Mon also has significant orbital precession which allowed us to perform the apsidal motion test of stellar structure. Physically, the observed apsidal motion rate in an eclipsing binary is a result of the tidal forces of each star on the other. This tidal force is linked to the density profile of each star. Thus, a careful analysis of apsidal motion offers the only window into the internal structure of a star other than asteroseismology. The internal structure is quantified by the constant log $k_2$, which is the logarithm of twice the tidal Love number (Kramm et al., 2011). We found that the prediction of log $k_{2,\rm theo}$ of the Granada models fully agrees with our observed log $k_2$.

## 1.3 Chapter III: Testing Brown Dwarf Stellar Formation Models with High Contrast Imaging

Brown dwarfs occupy a range of mass greater than planets ($\gtrsim$ 14 Jupiter masses) and less than the hydrogen burning lower limit for stars ($\lesssim$ 75 Jupiter masses). Given that brown dwarfs do not have thermonuclear fusion, their radius to first order is defined by an equilibrium between the force of gravity and the electron degeneracy pressure, and thus these objects cool over time and evolve through the M, L and T spectral types (see review by Chabrier & Baraffe, 2000). Brown dwarfs serve as the

transition between planets and stars. Thus, their study can shed light simultaneously on the lower mass limit of star formation, and upper mass limit of planet formation. The formation mechanism(s) for brown dwarfs remain relatively unconstrained. A few of these formation scenarios, which are detailed in a review by Luhman (2012) and references therein are:

- brown dwarfs could form with other stars in a single core, and suffer an early ejection via 3-body interactions, thus halting accretion of material, or
- they could form in massive disks that collapse under gravitational instability and then get ejected via 3-body interactions, and finally
- they could form in a very low mass core, which is photo-ionized by nearby massive stars thus preventing mass accretion.

All or none of the above scenarios could be the mechanism(s) by which brown dwarfs form. One way to differentiate between them is taking a census of the number of brown dwarfs with companions, known as the brown dwarf binary frequency. The observed binary frequency as function of mass, semi-major axis, and eccentricity must be reproduced by predictions from the above formation scenarios (Burgasser et al., 2007; Luhman, 2012).

As detailed in chapter III and published in Garcia et al. (2015a), I searched for brown dwarf binaries by imaging 11 of the lowest mass brown dwarfs in the Pleiades star forming region with the Wide Field Camera 3 on board the Hubble Space Tele-

scope. I developed a new semi-empirical PSF fitting technique and a careful treatment of false positive detections, to search for companions as close as 30 milli-arcseconds to their target stars, pushing the limit of HST/WFC3 angular resolution at I-band to $\approx \frac{\lambda}{2D}$. We found no binaries implying a low brown dwarf binary frequency, in good agreement with simulations of low-mass star formation by Bate (2012) which favors the ejection scenario for brown dwarf formation. This work however remains preliminary given that we only observed 11 stars.

## 1.4 Chapter IV: Testing 2D and 3D Stellar Atmosphere Models with Optical Interferometry

Stars are inherently three dimensional objects that exhibit differential rotation, convection, and gravity darkening across their surfaces. However, the vast majority of stellar models are one dimensional, and either ignore or approximate the underlying three dimensional physical processes of stars. We have revolutionized our understanding of the Sun by using three dimensional models to match the observed stellar surface features at optical wavelengths Asplund et al. (2009).

However, we have yet to constrain 3D or even 2D stellar models of stars other than the Sun with observations at visible wavelengths. This is because no direct images of main sequence stars at visible wavelengths exist other than the Sun. At first glance, this goal may seem intractable, given that main sequence stars are typically 1-5 milli-arcseconds in diameter, $10-100\times$ smaller than even the best angular resolution with

the Hubble Space Telescope at optical wavelengths.

Fortunately, visible-light long baseline interferometry provides the required $\approx 1$ mas angular resolution to produce model-independent image reconstruction of the surfaces of main-sequence stars. Long baseline interferometry at optical wavelengths operates similarly to the Atacama Long Millimeter Array (ALMA) at millimeter wavelengths: by interfering light collected from widely separated telescopes to form interferograms, thus gaining angular resolution. The angular resolution goes as $\propto \frac{\lambda}{B}$ where $B$ is the separation between the telescopes. There are two basic interferometric observables from these cosine-like interferograms: the amplitude of the light to dark pattern known as the squared visibility, and a linear combination of the phase, known as the closure phase. Both are necessary to reconstruct images of the surfaces of stars using an inverse Fourier transform, which is based in the van-Cittert Zernike theorem (Born & Wolf, 1999).

Other groups have had the goal of directly imaging the surfaces of main sequence stars at visible wavelengths (Ireland et al., 2008; Mourard et al., 2012). However, this goal typically faces two major difficulties: A) Most visible light interferometry is done by combining light of two or three telescopes, thus there is not enough interferometric information for model-independent image reconstruction and B) Data analysis techniques must deal with biases in the closure phase, the interferometric observable that directly measures the brightness asymmetries across the stellar disk.

As detailed in chapter IV, I have led a team of collaborators from Tennessee

State University, Lowell Observatory, University of Michigan and the Navy in commissioning the first 6 telescope beam combiner at visible wavelengths, the Visible Imaging System for Interferometric Observations at NPOI (VISION) for the Navy Precision Optical Interferometer (NPOI). VISION combines light from 6 telescopes on an electron-multiplying CCD, using single-mode polarization-maintaining fibers to guide and filter atmospheric turbulence. We completed commissioning of the VISION beam combiner for the Navy Precision Optical Interferometer in September 2015 (Garcia et al., 2015b, submitted), we addressed the technological hurdles that have so far prevented visible-light stellar surface imaging:

- A) VISION can combine 6 telescopes simultaneously, thus providing enough interferometric information for model independent image reconstruction.

- B) We demonstrated a new data analysis technique to subtract off the bias in the closure phase. We successfully tested our new technique by observing O-type supergiant binary $\zeta$ Orionis and recovering the predicted orbit from the literature (Hummel et al., 2013) using closure phases.

REFERENCES

Asplund, M., Grevesse, N., Sauval, A. J., & Scott, P. 2009, ARA&A, 47, 481

Bate, M. R. 2012, MNRAS, 419, 3115

Born, M., & Wolf, E. 1999, Principles of Optics, by Max Born and Emil Wolf and With contributions by A. B. Bhatia and P. C. Clemmow and D. Gabor and A. R. Stokes and A. M. Taylor and P. A. Wayman and W. L. Wilcock, pp. 986. ISBN 0521642221. Cambridge, UK: Cambridge University Press, October 1999.

Burgasser, A. J., Reid, I. N., Siegler, N., et al. 2007, Protostars and Planets V, 427

Chabrier, G., & Baraffe, I. 2000, ARA&A, 38, 337

Luhman, K. L. 2012, ARA&A, 50, 65

Garcia, E. V., Stassun, K. G., Hebb, L., Gómez Maqueo Chew, Y., & Heiser, A. 2011, AJ, 142, 27

Garcia, E. V., Stassun, K. G., & Torres, G. 2013, ApJ, 769, 114

Garcia, E. V., Stassun, K. G., Pavlovski, K., et al. 2014, AJ, 148, 39

Garcia, E. V., Dupuy, T. J., Allers, K. N., Liu, M. C., & Deacon, N. R. 2015a, ApJ, 804, 65

Garcia, E. V., Muterspaugh, M. W., van Belle, G., Monnier, J. D., Stassun, K. G., Ghasempour, A., Clark, J. H., Zavala, R. T., Benson, J. A., Hutter, D. J., Schmitt, H. R., Baines, E. K., Jorgensen, A. M., Strosahl, S. G., Sanborn, J., Zawicki, S. J., Sakosky, M. F., Swihart, S., 2015b, submitted to PASP

Hummel, C. A., Rivinius, T., Nieva, M.-F., et al. 2013, A&A, 554, A52

Ireland, M. J., Mérand, A., ten Brummelaar, T. A., et al. 2008, proc. SPIE, 7013, 701324

Kramm, U., Nettelmann, N., Redmer, R., & Stevenson, D. J. 2011, A&A, 528, A18

Mourard, D., Challouf, M., Ligi, R., et al. 2012, proc. SPIE, 8445, 84450K

Torres, G., Andersen, J., & Giménez, A. 2010, A&A Rev., 18, 67

# CHAPTER II

## Testing 1D Stellar Evolution and Structure Models with Observations of Eclipsing Binaries

**This chapter appears as:**

1. **Garcia et al.(2011), Apsidal Motion of the Massive, Benchmark Eclipsing Binary V578 Mon, Astronomical Journal, 142, 27**

2. **Garcia et al. (2013), Reanalysis of the Radii of the Benchmark Eclipsing Binary V578 Mon, Astrophysical Journal, 769, 114**

3. **Garcia et al.(2014), A Strict Test of Stellar Evolution Models: The Absolute Dimensions of Massive Benchmark Eclipsing Binary V578 Mon, Astronomical Journal, 148, 39**

### 2.1 Summary

We determine the absolute dimensions of the eclipsing binary V578 Mon, a detached system of two early B-type stars (B0V + B1V, P=2.40848 d) in the star-forming region NGC 2244 of the Rosette Nebula. From the light curve analysis of 40 yr of photometry and the analysis of HERMES spectra, we find radii of $5.41 \pm 0.04$ $R_{\odot}$ and $4.29 \pm 0.05$ $R_{\odot}$, and temperatures of $30000 \pm 500$ K and $25750 \pm 435$ K respectively. We find that our disentangled component spectra for V578 Mon agree well

previous spectral disentangling from the literature. We also reconfirm the previous spectroscopic orbit of V578 Mon finding that masses of $14.54 \pm 0.08$ $M_{\odot}$ and $10.29 \pm 0.06$ $M_{\odot}$ are fully compatible with the new analysis. We compare the absolute dimensions to the rotating models of the Geneva and Utrecht groups and the models of Granada group. We find all three sets of models marginally reproduce the absolute dimensions of both stars with a common age within uncertainty for gravity-effective temperature isochrones. However - there are some apparent age discrepancies for the corresponding mass-radius isochrones. Models with larger convective overshoot $> 0.35$ worked best. Combined with our previously determined apsidal motion of $0.07089^{+0.00021}_{-0.00013}$ deg cycle$^{-1}$, we compute the internal structure constants (tidal Love number) for the newtonian and general relativistic contribution to the apsidal motion, $\log k_2 = -1.975 \pm 0.017$ and $\log k_2 = -3.412 \pm 0.018$ respectively. We find the relativistic contribution to the apsidal motion of be small $< 4\%$. We find that the prediction of $\log k_{2,\mathrm{theo}} = -2.005 \pm 0.025$ of the Granada models fully agrees with our observed $\log k_2$.

## 2.2 Introduction

Detached eclipsing binary stars (dEBs) provide accurate observed stellar masses, radii, effective temperatures, and rotational velocities. See a recent review by Torres et al. (2010) for a discussion of 94 dEBs with accurate masses and radii used to test stellar evolution models. There are only nine total massive dEBs, or equivalently 18

stars whose physical parameters have been determined with an accuracy of better than 3%, making V578 Mon one of only nine EBs with $M_1 \geq M_2 > 10$ $M_\odot$ and with sufficient accuracy to be included in the Torres et al. (2010) compilation of benchmark-grade EBs. Figure 1 demonstrates the upper main sequence of all dEBs with $M_1 \geq M_2 > 10$ $M_\odot$ and masses and radii determined to 3% (adapted from Torres et al. (2010)). V578 Mon is therefore a benchmark system for testing stellar evolution models of newly formed massive stars. The accurate absolute dimensions of eclipsing binary stars provide a unique opportunity to test stellar evolution models in two ways: the "isochrone test" and the"apsidal motion test".

The "isochrone test" of stellar evolution models requires that the ages of both components of a dEB predicted from separate stellar evolution tracks to be the same within uncertainty of the absolute dimensions $(M, R, T_{\rm eff}, v_{\rm rot})$. For the "isochrone test", we assume that both components of the dEB formed together in the same initial gas cloud. Therefore, both components of a dEB are assumed to arrive at the zero age main sequence (ZAMS) at nearly the same time. Furthermore, their initial chemical compositions must be the same. Finally, we assume that each component of the binary evolves in isolation, where the effects of the companion star on the evolution is small or negligible.

The "isochrone test" is strongest for eclipsing binaries with low mass ratios $q = \frac{M_2}{M_1} < 1$. For dEBs where component masses $M_1 \approx M_2$, both stars will evolve on the same evolutionary track. This does not allow for strict tests of stellar evolution

models unless the chemical composition or effective temperature of the stars is known. Stellar evolution models will predict two stars of the same mass and composition to have the same age. Conversely, the larger the difference in initial mass between the components of the binary star, the larger the difference in main sequence (MS) lifetimes of the two stars. Therefore, the stellar models must have the accurate input physics to correctly predict how quickly stars of different mass evolve relative to each other. The correct input physics in turn yields correct predictions of the observed absolute dimensions of the detached eclipsing binary.

Detached eclipsing binary stars with apsidal motion (precession of the argument of periastron) also allow for the "apsidal motion test" of the stellar internal structure (Claret & Giménez, 2010). Physically, the observed apsidal motion rate in an eclipsing binary is a result of the tidal forces of each star on each other. In turn, this tidal force is linked to the internal structure of each star, the star's separation, their mass ratio $q$ and their radii $R_1$ and $R_2$. The internal structure is quantified by the constant $\log k_2$ which is the logarithm of twice the tidal Love number (Kramm et al., 2011). The "apsidal motion" test compares the theoretical internal structure constant $\log k_{2,\mathrm{theo}}$ to the observed internal structure constant $\log k_{2,\mathrm{obs}}$. The observed internal structure constant is a function the observed absolute dimensions and apsidal motion of the eclipsing binary. The observed internal structure constant is very sensitive to the radii ($k_{2,\mathrm{obs}} \propto R^5$) - therefore, this test can only be performed with accurate stellar radii. However, including this study of massive dEB V578 Mon, there are only five massive,

eccentric eclipsing binaries available for these tests of internal structure (Claret & Giménez, 2010).

Here we combine the previous determination of $\dot{\omega}$ and $e$ from Garcia et al. (2011) with a reanalysis of 40 years worth of photometry to re-determine the fundamental properties of V578 Mon. We include the photometry used by the previous light curve analysis (Hensberge et al., 2000). We compare the masses, temperatures and radii of V578 Mon with rotating high mass stellar evolution models by Granada (Claret, 2004, 2006), Geneva (Georgy et al., 2013; Ekström et al., 2012), and Utrecht (Brott et al., 2011) groups. We also compare the observed internal structure constant $\log k_{2,\mathrm{obs}}$ with theoretical $\log k_{2,\mathrm{theo}}$ using the methods of Claret & Giménez (2010).

### 2.3 The Eclipsing Binary V578 Mon in NGC 2244

The photometric variability of the bright (V=8.5), 2.408 day period, eccentric, massive detached eclipsing binary (dEB) V578 Mon (HDE 259135, BD+4°1299), comprising a B1V type primary star and a B2V type secondary star was first identified in the study by Heiser (1977) of NGC 2244 within the Rosette Nebula (NGC 2237, NGC 2246). The identifications, locations and photometric parameters for V578 Mon are listed in Table 1. The absolute dimensions of V578 Mon have been determined from three seasons of Strömgren *uvby* photometry and one season of radial-velocity data by Hensberge et al. (2000). An analysis of the metallicity and evolutionary status of V578 Mon was undertaken by Pavlovski & Hensberge (2005) and Hensberge

et al. (2000). The masses and radii of V578 Mon determined from these data are $14.54 \pm 0.08$ $M_\odot$ and $10.29 \pm 0.06$ $M_\odot$, and $5.23 \pm 0.06$ $R_\odot$ and $4.32 \pm 0.07$ $R_\odot$ for the primary and secondary respectively (Hensberge et al., 2000). V578 Mon was included in the list of 94 detached eclipsing binaries with masses and radii accurate to 2% by Torres et al. (2010). The radii for V578 Mon listed in Torres et al. (2010) were found to be incorrect by Garcia et al. (2013) given system's eccentric orbit and asynchronous rotation. The apsidal motion $\dot{\omega}$ and a new eccentricity $e$ were determined in Garcia et al. (2011). V578 Mon was observed by MOST (Pribulla et al., 2010).

Given the inclination of V578 Mon, its eclipses are partial, meaning that neither star is fully out of view of Earth. Partial eclipses can translate into a degeneracy between the radii, preventing the component radii $R_1$ and $R_2$ from being individually measured. However, V578 Mon also has an eccentric orbit, meaning that the eclipse durations are not equal, which helps breaks this degeneracy and allows the radii to be determined separately. V578 Mon is observed to not have tidally locked yet. The system has a low mass ratio $q$=0.7078 as compared to similar systems with well-determined absolute parameters such as V1034 Sco, V478 Cyg, AH Cep, V453 Cyg, and CW Cep (Bouzid et al., 2005; Popper & Etzel, 1981; Popper & Hill, 1991; Bell et al., 1986; Holmgren et al., 1990; Southworth et al., 2004; Popper, 1974; Stickland et al., 1992). Of all of these systems, V578 Mon is also the youngest, making this system a benchmark case for testing stellar evolution models at the youngest ages.

## 2.4 Data

### 2.4.1 Johnson UBV and Strömgren *uvby* Photometry

The available time-series photometry of V578 Mon covers nearly 40 yr and more than one full apsidal motion period. A summary of the various light curve epochs, including filters and observing facilities used, is presented in Table 2. Photometry from Heiser (2010) includes multi-band light curves spanning 1967–2006 from the 16-in telescope at Kitt Peak National Observatory (KPNO) and from the Tennessee State University(TSU) -Vanderbilt 16-in Automatic Photoelectric Telescope (APT) at Fairborn Observatory. The KPNO Johnson $UBV$ light curves comprise 725 data points spanning 1967–1984 with average uncertainties per data point of 0.004 mag computed by Heiser (2010). The APT Johnson $BV$ light curves span 1994–2006 and consist of 1783 data points with average uncertainties per data point of 0.001 mag for B and 0.002 mag for V (Heiser, 2010). Light curves from Hensberge et al. (2000) span 1991–1994 from the 0.5-m Strömgren Automatic Telescope (SAT) at La Silla, with 248 data points in each of the *uvby* filters and average uncertainty per data point of 0.003 mag (Hensberge et al., 2000). We begin our light curve analysis with the observational errors originally estimated by Heiser (2010) and Hensberge et al. (2000). Table 2 lists these average uncertainties, $\sigma_0$, as reported by the original authors. However, from our light curve fits (see below) we found that these uncertainties were in most cases underestimated. Thus we also report as $\sigma$ in Table 2 the uncertainties that we ultimately adopted for each light curve.

### 2.4.2 HERMES Spectroscopy

A new series of high-resolution echelle spectra were secured in December 2011 (36 exposures) and February 2012 (8 exposures) with HERMES, the fiber-fed high-resolution spectrograph on the Mercator telescope located at the Observatorio del Roque de los Muchachos, La Palma, Canary Islands. HERMES samples the entire optical wavelength range (3800-9000 Å) with a resolution of $R = 85\,000$ (Raskin et al., 2011). The observations listed in Table 3 cover the orbital cycle uniformly. Groups of two concatenated exposures allow us to obtain a robust estimation of random noise as a function of wavelength, and a check on cosmic ray events surviving the detection algorithm in the data reduction. In total, 44 exposures were obtained at 19 epochs, 16 of which are out of eclipse. One series of six exposures starts near the primary mid-eclipse; One series of two concatenated exposures taken around secondary mid-eclipse has a significantly lower exposure level, but another one consisting of four concatenated exposures starting around secondary mid-eclipse is available.

Exposure times close to 2100 s were used for most spectra, but in case of one out-of-eclipse epoch the exposure time was significantly shorter, 1200 s. The signal-to-noise ratio of the spectra is 50 to 100 at 4000 Å, then rapidly increasing to 120 up to 200 at 5000 Å and remaining close to this level at longer wavelengths. The numbers apply to the sum of two concatenated exposures. The reduction of the spectra has been performed using the HERES pipe-line software package. The spectra resampled directly in constant-size velocity bins ($\ln \lambda$), very nearly in size to the detector pixels,

were used. Normalization to the continuum is done separately.

The HERMES spectra outnumber the CASPEC spectra used by Hensberge et al.(2000), but fall short with regard to signal-to-noise ratio. However, they cover a much larger wavelength region, include epochs in both eclipses and cover the orbit more homogeneously. In the wavelength region covered by both sets, the reconstruction has better signal-to-noise ratio in the CASPEC set, but the risk of bias due to phase gaps might be higher with the CASPEC data. Both data sets were obtained in different parts of the apsidal motion cycle.

## 2.5 Analysis

### 2.5.1 Spectral Disentangling & Light Ratio

In V578 Mon binary system the eclipses are partial which causes degeneracy in the light curve solution for the radii of the components. It was checked whether a spectroscopic light ratio has sufficient precision to reduce the degeneracy. This light ratio might be constrained either by the changing line dilution during the eclipse, or/and by constrained fitting of the reconstructed component spectra by theoretical spectra, simultaneously deriving the light ratio as well as the photospheric parameters (Tamajo et al., 2011). In the latter implementation, the light ratio is assumed identical in all observed spectra, hence eclipse spectra are not used.

With partial eclipses of roughly 0.1 mag depth, and less for the secondary eclipse at the epoch of the spectroscopy, line depth in the composite spectrum is affected

at the level of 0.5% of the continuum only when the two components have in their intrinsic spectra a line differing by 7% of the continuum depth. The similarity of the components and the rotational broadening in the spectra imply that no metal line approaches this level. Hence, using the changing line dilution to measure the light ratio precisely is challenging. Exceedingly large signal-to-noise ratios would be required to be able to use single or few lines. Including many lines, i.e. large stretches of spectrum offers the opportunity to reduce the requirements on the signal-to-noise ratio. However, bias in tracing the continuum is expected to put an upper limit to the precision with which the light ratio can be measured in a system with components with similar spectra and substantial rotation.

Therefore, we explored the alternative option of constrained fitting, although it is model-sensitive. Spectral disentangling (Hadrava, 1995), further referred as SPD is performed in a spectral range of about 100 - 150 Å (of the order of 4000 bins) in the wavelength range 3900 - 5000 Å, centered on prominent lines of He I, He II and stronger metal lines. The apsidal motion study (Garcia et al., 2011) permitted us to fix the eccentricity $e$, the longitude of the periastron, $\omega$, for the epoch of the spectra, and the time of periastron passage. The SPD code used is FDBINARY[1] (Ilijic et al., 2004).

SPD applied to selected spectral regions of the HERMES spectra, well distributed over the full range of Doppler shifts in the orbit (see orbital phases in Table 3),

[1] http://sail.zpf.fer.hr/fdbinary/

leads to radial velocity amplitudes K1 and K2 compatible with Hensberge et al. (2000) within better than 1 km/s. Thus the spectra are reconstructed using the mean orbital elements (Table 4), now also including regions around $H_\gamma$ and $H_\delta$ ($H_\beta$ has a broad interstellar band centered on its red wing). For the constrained fitting, optimization was done for hydrogen and helium lines only, and for combinations of them. The reconstructed spectra for both out-of-eclipse and in-eclipse phases are shown in Figures 2 and 3.

The component spectra for different dilution factors can be obtained from a single disentangling computation, followed by an adequate renormalisation. As starting point for the photospheric parameters, $T_{\rm eff,1} = 30\,000$ K, and $T_{\rm eff,2} = 26\,400$ K is used, based on the extensive study of Hensberge et al. (2000) and Pavlovski & Hensberge (2005). The surface gravities of the components are fixed to $\log g_1 = 4.133 \pm 0.018$ and $\log g_2 = 4.185 \pm 0.021$ as derived in this paper. This suppresses the degeneracy of line profiles of hot stars in the (temperature, gravity) plane. Calculations for a small grid in $\log g$ has shown that the effect of fixing $\log g$ might produce deviations of about a few tenths of the percentage in determining the light dilution factors.

Optimization of relative light factors includes a search through a grid of theoretical spectra, using a genetic algorithm. A grid of synthetic spectra was calculated assuming non-LTE line formation. The calculations are based on the so-called hybrid approach of Nieva & Przybilla (2007) in which model atmospheres are calculated in LTE approximation and non-LTE spectral synthesis with detailed statistical balance.

Model atmospheres are constructed with ATLAS9 for solar metallicity, [M/H] = 0, and helium abundance by number density, $N_{\rm He}/N_{\rm tot} = 0.089$ (Castelli et al., 1997). Non-LTE level populations and model spectra were computed with recent versions of DETAIL and SURFACE (Butler & Giddings, 1985). Further details on the method, grid and calculations can be found in Tamajo et al. (2011) and Pavlovski et al. (2009).

Depending on the line(s) included, the primary is found to contribute 68 to 72 percent of the total light, with hydrogen lines supporting the larger fractions. Hydrogen suggests a few percent lower temperature for the primary, compared to the starting values. This is compatible with the tendency seen in Figure 7 of Hensberge et al. (2000), that H and He lines for the primary only marginally agree on effective temperature (taking minimum $\chi^2$ at the relevant gravity, a 1000 K difference in temperature estimation occurs).

The inconsistency between different indicators underlines the importance to develop a more consistent atmosphere model for these stars. One way, following Nieva & Przybilla (2012), is to include more ionization equilibria by analyzing the full wavelength range covered by the new spectra. This work-intensive analysis is out of the scope of the present paper, but probably indispensable to constrain better the degeneracy in the determination of the radii. Its success might be limited by the rotational broadening in the spectra. Another point of attention is the need to take into account temperature and gravity variations over the surface, due to the slightly non-spherical shape of the stars. Our work shows that the purely photometrically estimated light

factors (Table 5) lie within the broader range $0.68 - 0.72$ of light factors (primary to total light) derived here from the HERMES spectra. However, there are some warnings that improvement is needed - the spectroscopic estimates may be biased as different indicators are not yet fully compatible.

### 2.5.2 Light Curve Analysis

We use EB modeling software PHOEBE (Prša & Zwitter, 2005) based on Wilson-Devinney code (Wilson & Devinney, 1971; Wilson, , 1979) for our light curve analysis. We fit light curves spanning 40 yrs, covering one full apsidal motion cycle and in Johnson $UBV$ and Strömgren $uvby$ photometry.

Figures 4, 5, 6, 7 are the residuals (data-model) for our global best fit model to the light curves for every light curve epoch and filter in Table 2. Overall, the residuals are small - typically $\approx 0.005$ mag. The residuals are significantly larger for light curve epochs 1970-1984, since error bars on the photometry data points measured using photometric plates is larger. We explore ranges for our light curve parameters as listed in Table 6. Our global best fit matches observations well - the final light curve parameters $\Omega_1$, $\Omega_2$, $i$, and $\frac{T_2}{T_1}$ are listed in Table 7.

#### 2.5.2.1 Setup

For our global best fit light curve model, we adopt a square root limb darkening law (Claret, 2000), a B1V spectral type for the primary star implying $T_1 = 30000$ K

(Hensberge et al., 2000), no light reflection, and no third light.

We have four light curve parameters of interest - primary potential $\Omega_1$, secondary potential $\Omega_2$, inclination $i$ and temperature ratio $\frac{T_2}{T_1}$. A "parameter of interest" is defined as a parameter that is varied to compute our confidence intervals. We determine these parameters and their uncertainties by mapping $\chi^2$ space. Potential $\Omega$ is a modified Kopal potential for asynchronous, eccentric orbits (Wilson, , 1979). The potential ($\Omega \propto R^{-1}$) takes into account contributions from the star itself, its companion, the star's rotation about its axis, and the star's rotation in its orbit.

Our fixed parameters are the argument of periastron $w_0$, eccentricity $e$, apsidal motion $\dot{\omega}$, semi-major axis $a$, mass ratio $q$, period $P$, ephemeris $\mathrm{HJD}_0$, systemic velocity $\gamma$, gravity brightening coefficients $g_1$ & $g_2$, primary and secondary synchronicity parameters $F_1$, $F_2$ and albedos $A_1$, $A_2$. We fix the argument of periastron $w_0$, eccentricity $e$ and apsidal motion $\dot{\omega}$ to values determined by a multi-epoch light curve analysis from Garcia et al. (2011). We fix mass ratio $q \equiv \frac{M_2}{M_1}$, semi-major axis $a$, orbital period $P$, time of minima $\mathrm{HJD}_0$ and systemic velocity $\gamma$ to values from Hensberge et al. (2000) analysis of the spectroscopic orbit. As mentioned previously, our HERMES spectra analysis derives radial velocity amplitudes $K_1$ and $K_2$ in agreement with the Hensberge et al. (2000) spectroscopic orbit (see Table 4). We adopt gravity brightening coefficients $(g_1, g_2)$ and surface albedos $(A_1, A_2)$ to be 1.0 as appropriate for stars with radiative envelopes. The gravity brightening coefficient $g_1 = g_2 = 1.0$ for stars with radiative envelopes was first found by von Zeipel (1924). We fixed ro-

tational synchronicity parameters $F_1 = 1.13$ and $F_2 = 1.11$ to values from Hensberge et al. (2000). Our limb darkening coefficients follow the square-root law for hot stars (Claret, 2000) and are listed in Table 8.

#### 2.5.2.2 Fitting Method

Our fitting method is adapted from Gómez Maqueo Chew et al. (2014, in prep). We determine our best fit global light curve solution by finding a unique set of light curve parameters $\Omega_1$, $\Omega_2$, $\frac{T_2}{T_1}$ and $i$ that correspond to the minimum chi square $\chi^2_{\rm min}$ in a well mapped grid of parameter space. The chi square is a function of the light curve parameters, $\chi^2 = \chi^2(\Omega_1, \Omega_2, \frac{T_2}{T_1}, i)$. We map parameter space by computing $\chi^2$ for a grid of $> 10^5$ unique sets of these light curve parameters. We use our map of parameter space to compute the uncertainties on our light curve parameters using confidence intervals. Plots of $\Delta\chi^2$ vs stellar radii $R_1$, $R_2$, temperature ratio $\frac{T_2}{T_1}$, and inclination $i$ with confidence intervals are shown in Figure 8.

The step-by-step procedure is as follows:

1. We sample a coarse grid of $10^4$ points defined by a range of potential $\Omega_1$, potential $\Omega_2$, inclination $i$ and temperature ratio $\frac{T_2}{T_1}$. The parameter ranges and spacings are given in Table 6.

For each grid point, we fit only for the "light levels" in PHOEBE which is equivalent to the total light contribution from each star in the photometric bandpass. We avoid using the WD2003 differential corrections (DC) fitting algorithm within PHOEBE to

fit our light curve parameters. The DC algorithm can fall into local minima when fitting for many parameters. We compute the total chi square $\chi^2_k$ for each light curve fit as the sum of the chi square $\chi^2_p$ at each passband and epoch:

$$\chi^2_k(\Omega_{1k}, \Omega_{2k}, \frac{T_{2k}}{T_1}, i_k) = \sum_p^{15} \frac{\chi^2_p}{\sigma^2_p} \tag{1}$$

Where index $k$ corresponds to a unique point in parameter space ($\Omega_{1k}$, $\Omega_{2k}$, $\frac{T_{2k}}{T_1}$, $i_k$). $\chi^2_k$ is the total chi square over all light curves at a unique point $k$. Index $p$ corresponds to a unique light curve passband epoch as specified in Table 2. The chi square at specific passband $\chi^2_p$ is computed as:

$$\chi^2_p = \sum_i^N \frac{(f - f_m)^2}{\sigma^2_i} \tag{2}$$

Where $N = N_d - N_p = 3485$ is the number of photometry data points $N_d$ minus the number of parameters of interest $N_p$ over all light curve epochs. Each data point has an error bar $\sigma_i$. Each light curve at a specific epoch and filter has a multiplicative factor $\sigma_p$ which takes into account systematic error. Multiplicative factor $\sigma_p$ is used to normalize the $\chi^2$ such that $\chi^2_{\rm min} = N$ or reduced $\chi^2_{\rm min,red} = 1.0$. $f$ is the total flux of the binary at an HJD, and flux $f_m$ is the corresponding model. From our coarse grid, we find the minimum total chi square $\chi^2 = \chi^2_{\rm min}$ in parameter space.

2. We adjust the error bars of the individual photometry data points for all light curves to take into account any systematic error. For the minimum $\chi^2_{\rm min}$ solution,

the passband $\sigma_p$ is computed for each separate light curve epoch and filter using the equation:

$$\sigma_p = \sqrt{\frac{N}{\chi^2_{\rm min}}} \tag{3}$$

Where $N = 3486$ as in step 1, and $\chi^2_{\rm min}$ is the minimum total $\chi^2$ of the coarse grid. We choose compute multiplicative factor $\sigma_p$ to weight each light curve such that the minimum reduced chi squared $\chi^2_{\rm min,red} = 1.0$ for our global best fit solution. We then rescale the $\chi^2$ of all other light curve fits using the passband $\sigma_p$:

$$\chi^2_k = \sum_p^{15} \frac{\chi^2}{\sigma^2_p} \tag{4}$$

Where $\chi^2$ un-scaled and $\chi^2_k$ is the scaled chi square at a unique point in parameter space $k$.

3. We perform steps 1 and 2 for a fine grid of $> 10^5$ points in parameter space around the location of the minimum $\chi^2_{\rm min}$. In this way we carefully map out parameter space at the location of the $\chi^2_{\rm min}$. We use multiple fine grids to precisely find our global best fit minimum. The average grid spacings are 0.005, 0.005, 0.03 and 0.0005 respectively for $\Omega_1$, $\Omega_2$, $i$ and $\frac{T_2}{T_1}$.

We find that the location of the minimum $\chi^2$ moves slightly, and we recompute the multiplicative factor $\sigma_p$ for each light curve to account for this, again making $\chi^2_{\rm min,red} = 1.0$. Finally, we have a global best fit solution within a finely sampled parameter space. Our global best fit solution listed in Table 7 corresponds to the

point in parameter space where scale chi square by $\sigma_p$ such that $\chi^2_{\rm min,red} = 1.0$.

#### 2.5.2.3 A Comparison of Light Curve Models

In order to ensure our light curve solution is robust and thus our light curve parameters are accurate, we compare our best fit light curve model described above with several other models. As shown in Table 9 we find little effect on our best fit light curve parameters from using different light curve models. All other models are not as favorable due to larger $\chi^2$ or temperatures that do not agree with the analysis of the component spectra of V578 Mon from spectral disentangling of Hensberge et al. (2000).

For all the tests described below, we start at our best fit solution, then fit all light curves in PHOEBE for primary potential $\Omega_1$, secondary potential $\Omega_2$, temperature ratio $\frac{T_2}{T_1}$, and inclination $i$. Our global best fit uses a fixed primary temperature $T_1 = 30000$ K, no light reflection and no third light. Furthermore, our global best fit uses fixed square root law limb darkening coefficients, which are found to work best for hot ($T_{\rm eff} > 9000$K) stars (Diaz-Cordoves & Gimenez, 1992; van Hamme, 1993). We discuss the different light curve models in the order in which they appear in our summary Table 9:

1. **Fitting for Limb Darkening Coefficients.** We test the effect of fitting for square root law limb darkening coefficients, finding a lower chi square due to a larger number of free parameters. We find little effect on $\Omega_1$, $\Omega_2$ or $i$. However

- we do find a much lower $T_2$ =25049. We reject this light curve model since $T_2$ =25049 is significantly outside of the acceptable range for $T_2$ =26400 $\pm$ 400 from the spectral disentangling of Hensberge et al. (2000). We therefore perform another test: we keep $\frac{T_2}{T_1}$ fixed to our best fit value, and fit for the limb darkening parameters, $\Omega_1$, $\Omega_2$ and $i$. We again find little effect on $\Omega_1$, $\Omega_2$ or $i$.

2. **Using a different Limb Darkening Law.** We test the linear cosine and logarithmic limb darkening laws, finding little effect on our light curve parameters. The linear cosine law has a lower $\chi^2$ =3480.01 than our best fit model $\chi^2$ =3489.00. The light curve model with logarithmic limb darkening has a larger $\chi^2$ =3503.96 - we therefore reject this model. See Table 8 for a list of the theoretical limb darkening coefficients for each light curve model that we test.

3. **Changing the assumed Primary Star Temperature.** We test the effect of changing our adopted primary star effective temperature $T_1$. Our adopted primary temperature for our best fit solution is $T_1$ =30000 $\pm$ 500 K. Once again, we find little effect on $\Omega_1$, $\Omega_2$, $i$ or $\frac{T_2}{T_1}$.

   We start with our best fit global solution, but set $T_1$ = 31500 K and $T_1$ = 28500 K, $3\sigma$ above and below our adopted primary star effective temperature. Fits with lower primary temperature $T_1$ do result in a better $\chi^2$ - however, $T_1 <$ 29000 K does not agree with the spectral disentangling analysis from Hensberge et al. (2000). This may be due to the fact that the PHOEBE light curve analysis constrains the temperature ratio and not the individual temper-

atures themselves. Further light curve tests at lower preferred temperatures $T_1$ and $T_2$ confirmed that changing effective temperatures have little effect on the geometric parameters, $\Omega_1$, $\Omega_2$ and $i$.

4. **Light Reflection.** We fit our light curve model with one light reflection. We find an inclination $i$ larger by $2\sigma$. However, the $\chi^2$ =3522.57 is higher than our best fit $\chi^2$ =3489.00. We reject this model on this basis.

5. **Third Light.** We test the possibility of third light and its effect on our best fit parameters. We fit for a third light parameter starting from our best fit light curve solution. The third light model has a lower $\chi^2$ due to a larger number of free parameters. We find $\Omega_1$ and $i$ to be larger by $2\sigma$ and $2.5\sigma$ respectively from our best fit model.

   However, the third light parameter $L_3$ varies on the order of an apsidal period of the system. As shown in Table 10, we find at max a small contribution of third light $\frac{L_3}{L_{\rm tot}} \approx 0.045$ for Johnson B filter of light curve epochs 1967-1984 and 2005-2006. This is likely due to PHOEBE using the $L_3$ parameter to minimize the small systematic error of 0.005 mag in the residuals of the 1967-1984 and 2005-2006 light curve epochs. Furthermore, the systemic velocity measured with the HERMES spectra and the CASPEC spectra in Hensberge et al. (2000) does not give any evidence for a large third body in the system that would contribute significantly to the light. This is consistent with the third-light tests performed here.

#### 2.5.2.4 Uncertainties on Light Curve Parameters

We compute uncertainties on each parameter of interest using confidence intervals as shown in Figure 8. From Press et al. (2002), for four parameters of interest, we find that $1\sigma$, $2\sigma$, and $3\sigma$ uncertainties correspond to solutions with confidence intervals of $\Delta\chi^2 = \chi^2 - \chi^2_{\rm min,red} = 4.72$, 9.70 and 16.3 respectively. Here, $\chi^2_{\rm min}$ is the minimum $\chi^2$ of our global best fit solution.

From Figure 8 we see small degeneracies between the geometric parameters - radii $R_1$, $R_2$, and inclination $i$. However - as expected we do not see degeneracies between the geometric light curve parameters and the temperature ratio $\frac{T_2}{T_1}$.

Since $\frac{T_2}{T_1}$ is not strongly degenerate with these other parameters, we could potentially decrease the number of parameters of interest and in turn decrease the formal parameter uncertainties. Therefore, the uncertainties presented here are possibly conservative, given that we assume all degrees of freedom are parameters of interest (Avni, 1976).

The small degeneracies in our parameters leads to uncertainties on potentials $\Omega_1$ and $\Omega_2$ of less than $< 1.5\%$ error - this error already takes into account any systematic error in fitting the light curves, as detailed in §2.5.2.2. Similarly, the uncertainty on the temperature ratio $\frac{T_2}{T_1}$ and inclination are also $< 1\%$.

A source of systematic uncertainty unaccounted for from the confidence intervals and fitting procedure in §2.5.2.2 is from the comparison of light curve models detailed in §2.5.2.3 and Table 9. As shown in Table 9, all other light curve models assessed in

§2.5.2.3 with the exception of using linear cosine LD parameters are not as favorable as our best fit model. The linear cosine model has a lower $\chi^2$. Nevertheless, The inclination $i$, temperature ratio $\frac{T_2}{T_1}$ and secondary potential $\Omega_2$ are all within $1\sigma$ of our best fit model. However, the primary potential for the linear cosine model $\Omega_1$ =4.92 as compared to our best fit $\Omega_1$ =$4.88 \pm 0.03$. Therefore our uncertainty on $\Omega_1$ from our best fit model could be slightly underestimated from these model comparisons.

#### 2.5.2.5 Consistency of Light Fractions

As mentioned by Torres et al. (2010) an important consistency check of our light curve solution is that the light fraction $l_{f,1} = \frac{l_1}{l_1+l_2}$ determined from spectroscopy and photometry agree. Given the small degeneracy between $R_1$ and $R_2$ as seen in Figure 8, we compare our photometrically determined light fraction with the light fraction from the HERMES spectral disentangling and a previous combined light curve and spectral disentangling analysis from Hensberge et al. (2000). We find that all three light fractions agree with each other to within $1.2\sigma$. A comparison of light fractions is shown in Table 5.

For each of the $\approx 10^5$ light curve fits to our 40 yrs of photometry data, we compute the light fraction at each of the passbands Johnson $UBV$ and Strömgren $uvby$ photometry, $l_{f,1}(\lambda) = \frac{l_1(\lambda)}{l_1(\lambda)+l_2(\lambda)}$ where $l_1(\lambda)$ and $l_2(\lambda)$ are the contribution of the primary and secondary star to the total light at a specific passband out of eclipse. The distribution of light fractions $l_{f,1}$ for light curve models with confidence intervals

of $1\sigma$ and $2\sigma$ are shown in Figures 9 and 10.

### 2.5.3 Comparison with Hensberge et al. (2000)

Hensberge et al. (2000) uses an iterative, combined light curve and spectral disentangling analysis using the Wilson-Devinney light curve modeling program to compute their light cure parameters. We find that $R_1 = 5.23 \pm 0.06$ $R_\odot$ from Hensberge et al. (2000) is $2.5\sigma$ discrepant from our best fit $R_1 = 5.41 \pm 0.04$ $R_\odot$. We find that our inclination $i = 72.09 \pm 0.06$ deg is $1.6\sigma$ discrepant from $i = 72.58 \pm 0.30$ deg from Hensberge et al. (2000). These discrepancies are likely due to the addition of apsidal motion and an updated eccentricity determined in Garcia et al. (2011). Apsidal motion and eccentricity can affect the potentials $\Omega_1$ and $\Omega_2$ and hence the determination of the radii at a low level. The potential $\Omega$ for a non-circular orbit is a function of eccentricity (see Wilson, (1979)). The addition of more light curve epochs may also play a role. Hensberge et al. (2000) only uses the 1991-1994 light curve epoch with Strömgren *uvby* photometry. As a check, we also recover the Hensberge et al. (2000) light curve solution when we fit only the 1991-1994 light curve epoch. Finally, simply the addition of more photometry data points may play a role. We use 3489 photometry data points in our light curve solution, whereas Hensberge et al. (2000) use 992. Our best fit secondary radius $R_2 = 4.29 \pm 0.05$ $R_\odot$ is in agreement with $4.32 \pm 0.07$ $R_\odot$ from Hensberge et al. (2000). Our best fit temperature ratio $\frac{T_2}{T_1} = 0.858 \pm 0.002$ is in agreement with the temperature ratio of $0.88 \pm 0.020$ from an

analysis of the disentangled component spectra (Hensberge et al., 2000).

## 2.6 Results: Absolute Dimensions and Apsidal Motion of V578 Mon

The absolute dimensions and other fundamental properties of V578 Mon are compiled in Table 11. Here we detail how each fundamental parameter for V578 Mon is compute in order of which they appear in Table 11:

1. **Orbital Period.** We adopt the orbital period $P = 2.4084822$ d from Hensberge et al. (2000).

2. **Masses.** The component masses $M_1 = 14.54 \pm 0.08$ $M_\odot$ and $M_2 = 10.29 \pm 0.06$ $M_\odot$ are determined from the spectroscopic orbit analysis from Hensberge et al. (2000). We do not use RVs from our HERMES spectroscopy because the CASPEC spectra have higher S/N - however, our analysis of the HERMES spectroscopy reconfirm the spectroscopic orbit.

3. **Radii.** We find precise uncertainties of $< 1.5\%$ for the primary radius $R_1 = 5.41 \pm 0.04$ $R_\odot$ and secondary radius $R_2 = 4.29 \pm 0.05$ $R_\odot$ from our confidence intervals in Figure 8.

4. **Temperatures.** We find a 0.3% error on our temperature ratio $\frac{T_2}{T_1} = 0.858 \pm 0.002$ from our confidence intervals. Combined with the adopted temperature of the primary star $T_1 = 30000 \pm 500$ K (Hensberge et al., 2000), our temperature ratio of $\frac{T_2}{T_1}$ yields a secondary temperature of $T_2 = 25750 \pm 435$ K via propagation

of errors.

5. **Rotational Velocities.** We compute surface rotational velocities of $v_{1,rot}$ =123± 5 km $s^{-1}$ and $v_{2,rot}$ =99 ± 3 km $s^{-1}$ using the observed projected surface velocities $v_1 \sin i$ =117 ± 4 km $s^{-1}$ and $v_2 \sin i$ =94 ± 2 km $s^{-1}$ from Hensberge et al. (2000) and our inclination of i=72.09 ± 0.06. The uncertainty on rotational velocities are computed from propagating the error on the inclination $i$ and the observed vsin $i$.

6. **Surface Gravities.** We compute the surface gravity $\log g$ from our masses and radii, finding $\log g_1$ =4.133 ± 0.018 cm $s^{-2}$ and $\log g_2$ =4.185 ± 0.021 cm $s^{-2}$. We compute the uncertainty on $\log g$ via error propagation:

$$\sigma_{\log g} = \sqrt{(\frac{\sigma_M}{M \ln 10})^2 + (\frac{2\sigma_R}{R \ln 10})^2} \tag{5}$$

Where $\sigma_M$ is the uncertainty on the mass and $\sigma_R$ is the uncertainty on the radius.

7. **Luminosities.** From our radii and temperatures, we compute compute luminosities for the primary and secondary star of $\log \frac{L_1}{L_\odot}$ =4.33 ± 0.03 and $\log \frac{L_2}{L_\odot}$ =3.86 ± 0.03. We compute the uncertainty on the luminosity using a similar error propagation as above, using errors from the temperature and radii, $\sigma_T$ and $\sigma_R$.

8. **Synchronicity Parameters.** We find the components of V578 Mon to be close but not exactly tidally locked, with $F_1$ =1.08 ± 0.04 and $F_2$ =1.10 ± 0.03. The synchronicity parameter $F = \frac{w}{w_{\rm orb}}$, where $w$ is the rotational velocity at the surface $v_{\rm rot}$ and $w_{\rm orb} = \frac{2\pi R}{P}$ is the synchronous velocity. We compute the uncertainty via propagation of error from $\sigma_R$, error on inclination $\sigma_i$, and error on projected rotational velocities $\sigma_{v \sin i}$.

9. **Internal Structure Constant.** One of us (Dr. Claret) computes the newtonian and general relativistic contributions to the observed internal structure constant, $\log k_{2,\rm newt}$ =−1.975 ± 0.017and $\log k_{2,\rm GR}$ =−3.412 ± 0.018.

## 2.7 The Stellar Evolution Models and Tests

We compare the absolute dimensions of V578 Mon to the stellar evolution models of three separate groups: (1) Geneva models of Georgy et al. (2013) and Ekström et al. (2012) hereafter Geneva13; (2) Utrecht models of Brott et al. (2011) here after Utrecht11 [2]; and (3) Granada models of Claret (2004, 2006) hereafter Granada04. We assume that both stars have the same initial chemical composition and age, as expected for tight binary systems. We perform two tests: (1) The "isochrone test" , which tests the ability of stellar evolution models to produce stars with different masses, radii, temperatures, rotational velocities, and surface compositions at the same age; and (2) The "apsidal motion test" which tests the ability of the stellar

[2]The Utrecht Stellar Evolution group is now located in Bonn, Germany

evolution models to reproduce the observed internal structure constant $\log k_2$ as determined from the observed apsidal motion.

A comparison of the basic input physics of the models is given in Table 12. The models use the same opacity tables of Iglesias & Rogers (1996). The mixing length $\alpha_{\rm MLT} \equiv \frac{l}{H_p}$ for all three sets of models differ by only 0.18 at maximum. The stellar evolution models use similar mass loss treatment from the prescription by Vink et al. (2001). Given the probable young age of V578 Mon due to its location in the open cluster NGC 2244 of the Rosette Nebula, the components of V578 Mon are not expected to have undergone significant mass loss (Vink et al., 2001).

However, all three sets of models differ on the choice of the convective core overshoot parameter $\alpha_{\rm ov}$. For the H and He burning phases of the convective core, the convective core size of the star is enlarged by $R_{\rm cc} = R_{cc}(1 + \frac{d_{\rm over}}{H_p})$, where $\alpha_{\rm ov} \equiv \frac{d_{\rm over}}{H_p}$ in units of pressure scale height. The overshoot parameter is designed to accomodate for the non zero velocity of the material moving from the convective core to radiative zone of the star. Observationally, a larger overshoot parameter means longer MS lifetimes for a given star, and thus older ages. The Geneva13 models use a small convective core overshoot of $\alpha_{\rm ov} = 0.1$ calibrated on width of the main sequence for stars with masses $M = 1.35 - 9.0$ $\rm M_{\odot}$ which is characterized by the red most point on the B-V, $M_V$ HR diagram (see figure 8 of Ekström et al. (2012)). The width of the main sequence is defined theoretically by the end of the hydrogen burning phase. The Utrecht11 models use a high convective core overshoot of $\alpha_{\rm ov} = 0.335$ which is cali-

brated using the observed width of the main sequence from the VLT-FLAMES survey of B stars (Evans et al., 2005; Hunter et al., 2007). The convective core overshoot parameter $\alpha_{\rm ov} = 0.335$ is chosen such that a 16 $M_{\odot}$ star ends its MS lifetime when $\log g = 3.2$. This $\log g$ coincides with the drop in B star rotation rates in a $\log g$-$v \sin i$ diagram, which is interpreted as an estimate of the width of the main sequence for B stars. See Brott et al. (2011) for an in depth discussion. The Granada04 models utilize a moderate convective core overshoot $\alpha_{\rm ov} = 0.2$, though we performed several tests varying $\alpha_{\rm ov}$.

Rotationally driven mixing can bring more H and He from the envelope to the core, thus extending the MS lifetime of the star - likewise a larger overshoot parameter extends the size of the core, leading to a longer MS lifetime. The Granada04 models do not incorporate rotational mixing, while the Geneva13 and Utrecht11 models do. However - All three sets of models include rotation. All three sets of models use similar metallicity compositions of near solar. The initial bulk composition for V578 Mon is expected to be close to solar given that Mg surface abundance is within error of the solar surface abundance, despite the fact that several atmospheric abundances such as C, N and O are somewhat metal poor compared to the Sun (Pavlovski & Hensberge, 2005). This is because Mg abundance is not expected to be altered from the initial abundance in a star, where as C, N and O atmospheric abundances could vary in V578 Mon due to rotational mixing (Lyubimkov et al., 2005). However, given that the C, N and O atmospheric abundances of V578 Mon may be lower than solar,

the metallicity of V578 Mon still remains as a source of systematic error in comparing the evolution models to the observations.

The Granada04 models also compute the internal structure constants $\log k_2, \log k_3$ and $\log k_4$ allowing for a test of the internal structure of V578 Mon via apsidal motion. Here we consider only the $k_2$ constant, given that $k_3$ and $k_4$ are very small. For V578 Mon, the tidal Love numbers quantify the deformation for each star's gravity field due to the companion.

### 2.7.1 Isochrone Test for V578 Mon

In Figure 11, we place the primary and secondary star on mass-radius and $\log g - \log T_{\rm eff}$ isochrones for each set of models. For the stellar evolution models to pass the "isochrone test" the models should predict a common age for both components of V578 Mon within uncertainty. Given how different the masses of the primary and secondary star for V578 Mon are the "isochrone test" provides a stringent test of stellar evolution models. We also match all evolution models to the rotational velocities of the primary and secondary star.

We find several Geneva13, Utrecht11 and Granada04 models predict masses, radii and temperatures for the components of V578 Mon that fall within $1\sigma$ uncertainty of the measured absolute dimensions. Therefore we estimate an age range for each star as shown in Table 12. The age difference for Geneva13, Utrecht11 and Granada04 models is given as the smallest possible difference between the ages of the two stars

given age range of each star.

For the Geneva models we use isochrones with initial rotational velocities $\frac{v_i}{v_{\rm crit}} = 0.30$ and $\frac{v_i}{v_{\rm crit}} = 0.35$ which allows us to match the observed rotational velocities for each star. We interpolate the model evolution tracks for the primary and secondary star using the online interactive tool provided by the Geneva group [3] . Attempts to match the observed rotational velocities of V578 Mon with lower ($\frac{v_i}{v_{\rm crit}} < 0.30$) or higher ($\frac{v_i}{v_{\rm crit}} > 0.40$) initial velocities for either star were unsuccessful. Attempts to find a single initial rotational velocity to reproduce the current observed rotational velocities for both stars with reasonable predicted radii and masses were also unsuccessful. However, given that V578 Mon is very near synchronization with the orbital period ($F_1 = 1.08 \pm 0.04$, $F_2 = 1.10 \pm 0.03$), the rotational history of V578 Mon could be different from the best matched $\frac{v_i}{v_{\rm crit}}$ found here. If the initial velocities of the components of V578 Mon were larger at the ZAMS than the orbital velocity, the stars could spin down to synchronize with the orbital velocity. Conversely, if $\frac{v_i}{v_{\rm crit}}$ was smaller than the orbital velocities, then the components of V578 Mon could spin up (Song et al., 2013). From Table 13 we find an age difference of 1.6 Myr for mass-radius isochrones, and an age difference of only 0.1 Myr for $\log g - \log T_{\rm eff}$ isochrone. It is easier to find consistency for the latter isochrones given our uncertainty in the effective temperatures of the two stars. We find that a primary radius of $R_1 = 5.50$ R$_\odot$ and a secondary star radius of $R_2 = 5.20$ R$_\odot$ yields common ages for the Geneva13

[3] http://obswww.unige.ch/Recherche/evol/-Database-

models. However, these radii are $3\sigma$ larger and $3\sigma$ smaller than our best fit model, respectively.

For the Utrecht11 models we use isochrones that match the observed surface velocities of the components of V578 Mon, $\mathrm{v}_{1,\mathrm{rot}} = 123 \pm 5$ km s$^{-1}$ and $v_{2,\mathrm{rot}} = 99 \pm 3$ km s$^{-1}$. The Utrecht11 models are computed at very small steps of mass and initial rotational velocity, such that interpolating between model tracks is unnecessary. From Table 13 we a marginally common age (age difference 0.4 Myr) for mass-radius isochrones, and a common age of $3.5 \pm 1.5$ Myr for $\log g - \log T_{\mathrm{eff}}$ isochrone. The models were computed at solar metallicity by Dr. Brott (private comm.).

We compute the Granada04 models at the masses of primary and secondary star and chose rotational velocities to match the observed rotational velocities of V578 Mon. We attempt to match the absolute dimensions of V578 Mon to $\log g - \log T_{\mathrm{eff}}$ or alternatively mass-radius isochrones for V578 Mon. We find an age gap of 1.5 Myr for mass-radius isochrones, and a marginally common age for $\log g - \log T_{\mathrm{eff}}$ isochrones, when both stars have an overshoot of $\alpha_{\mathrm{ov}} = 0.2$. Again - finding a match on the $\log g - \log T_{\mathrm{eff}}$ isochrones is easier given the greater uncertainty in the effective temperatures.

In an attempt to match the ages of the two stars on a mass-radius isochrone, we also compute Granada04 models for $\alpha_{\mathrm{ov}} = 0.4$ and $\alpha_{\mathrm{ov}} = 0.6$. Figure 12 demonstrates the time evolution of the radii for V578 Mon for these different models. We find a near match on a single mass-radius isochrone with an age difference of only 0.2 Myr

- if we assume that the primary star has a convective overshoot $\alpha_{\rm ov} = 0.6$ and the secondary star has a convective overshoot of $\alpha_{\rm ov} = 0.2$. We also find a common age of 5.5±1.0 Myr for the $\log g - \log T_{\rm eff}$ isochrone. This does not mean that an $\alpha_{\rm ov} = 0.6$ for the primary star is correct for V578 Mon - merely that a higher convective overshoot allows for compatible ages between the two stars. High convective overshoot has been found to work in matching other EBs on a single isochrone (Claret, 2007).

In general, we find younger ages by $\approx 1$ Myr for the Utrecht11 models of V578 Mon and similar ages for the Geneva13 and Granada04 models. This can be attributed to the larger convective overshoot of $\alpha_{\rm ov} = 0.355$ included in Utrecht11 models than in Geneva13 models ($\alpha_{\rm ov} = 0.2$). While the primary star for the Granada04 models does have an even higher convective overshoot of $\alpha_{\rm ov} = 0.6$, the models do not include rotational mixing, which also extends the main sequence lifetime of the stars.

### 2.7.2 Apsidal Motion Test for V578 Mon

Measurement of apsidal motion in eccentric binary systems allow for a stringent test of the internal structure constant $k_{2,\rm theo}$ predicted from stellar evolution models (e.g. Claret & Giménez, 2010). It is not possible to separate out each individual star's contribution to the apsidal period U from newtonian apsidal motion.

The apsidal motion for V578 Mon was measured by Garcia et al. (2011). The observed apsidal motion of the V578 Mon, $\dot{\omega}_{\rm tot} = 0.07089^{+0.00021}_{-0.00013}$ deg cycle$^{-1}$, has contributions from both newtonian and general relativity components (Claret & Giménez,

2010):

$$\dot{\omega}_{\rm obs} = \dot{\omega}_{\rm newt} + \dot{\omega}_{\rm GR} \tag{6}$$

where $\dot{\omega}_{\rm GR}$ is given by

$$\dot{\omega}_{\rm GR} = 0.002286 \frac{M_1 + M_2}{a(1-e^2)} \tag{7}$$

We find that $\dot{\omega}_{\rm GR}$ =$0.002589 \pm 0.000015$ which is only 4% of the newtonian apsidal motion $\dot{\omega}_{\rm newt}$ =$0.06830 \pm 0.00017$.

Both the newtonian and general relativistic observed apsidal motions $\dot{\omega}_{\rm newt}$ and $\dot{\omega}_{\rm GR}$ have associated observed internal structure constants $k_{2,\rm obs}$. The internal structure constant is twice the tidal love number (Kramm et al., 2011), and is related to the density profiles, degree of sphericity, orbital parameters, masses, and rotation rate of both components of a binary star. Specifically, the internal structure constant is related to the solution of the Radau differential equation as in equation 3 of Claret & Giménez (2010). Importantly - constant $k_{2,\rm obs}$ is one the few ways to directly constrain the internal structure of stars.

From the precise observed apsidal motion, we compute the observed internal structure constant, $k_{2,\rm obs} = k_{2,\rm obs}(M_1, M_2, R_1, R_2, P, U, F_1, F_2, e)$, where U is the apsidal period, given by the equations (adopted from Claret & Giménez (2010)):

$$k_{2,\rm obs} = \frac{1}{c_{21} + c_{22}} \frac{P}{U} \tag{8}$$

$$c_{2i} = [(F_i)^2 (1 + \frac{M_{3-i}}{M_i}) f(e) + 15 \frac{M_{3-i}}{M_i} g(e)] (\frac{R_i}{a})^5 \tag{9}$$

$$f(e) = (1 - e^2)^{-2} \tag{10}$$

$$g(e) = \frac{(8 + 12e^2 + e^4) f(e)^{2.5}}{8} \tag{11}$$

We compute the internal structure constant due to the newtonian apsidal motion, $\log k_{2,\mathrm{newt}} = -1.975 \pm 0.017$, and due to general relativity, $\log k_{2,\mathrm{GR}} = -3.412 \pm 0.018$. The newtonian apsidal motion is much larger than the general relativistic component, and therefore the internal structure constant is also much larger.

We compute the theoretical internal structure constant, $k_{2,\mathrm{theo}}$ using the methods of Claret & Giménez (2010). The theoretical $k_2$ constant was corrected for by rotation (Claret, 1999) and dynamical tides (Willems & Claret, 2002). The theoretical internal structure constant is a combination of the internal structure constants for both star, such that

$$k_{2,\mathrm{theo}} = \frac{c_{21} k_{21} + c_{22} k_{22}}{c_{21} + c_{22}} \tag{12}$$

which can then be compared to observations.

We find the predicted newtonian apsidal motion to be $\dot{\omega}_{\mathrm{theo}} = 0.06883 \pm 0.00017$ and consequently the predicted newtonian internal structure constant to be $\log k_{2,\mathrm{theo}} = -2.005 \pm 0.025$. This is in very good agreement with the observed $\log k_{2,\mathrm{obs}} = -1.975 \pm 0.017$. From equation 9, the parameter $c_{12}$ is about 67% larger than $c_{22}$. Therefore, the weighted contribution of the primary dominates the theoretical apsidal motion. V578 Mon is a relatively young system - therefore, $\log k_{2,\mathrm{theo}}$ is almost constant during the early phases of stellar evolution. The "apsidal motion test" is therefore complementary to

the "isochrone test". Claret & Giménez (2010) compile a list of eclipsing binaries with apsidal motion, demonstrating good agreement between observed and predicted apsidal motions. V578 Mon continues this trend of agreement between theoretical and observational internal structure constants. For this relatively young system, matching the radii, temperatures and masses isochrones is key, given that we have so few young massive EBs with non-equal mass ratio.

## 2.8 Conclusion

We have determined the absolute dimensions of the massive, detached eclipsing binary V578 Mon, which is a member of young star forming region NGC 2244 in the Rosette Nebula. We confirm that the the previously published spectroscopic orbit of Hensberge et al. (2000) agree with our current spectroscopic orbit of V578 Mon. From our HERMES spectra, we find that our photometric light ratio from the light curve analysis is fully compatible with the disentangled component spectra of V578 Mon.

From 40 yr of Johnson UBV and Strömgren *uvby* photometry we determine updated radii, measure the temperature ratio and light ratio for the components of V578 Mon. We determine the radii to better than 1.5% accuracy, and carefully map out parameter space in order to reveal any possible degeneracies. We also compare our global best fit light curve model with models that include different limb darkening parameters, a different assumed temperature for the primary star, light reflection or third light finding little effect on our global model. We do not unambiguously rule out

light reflection or a third body, but we confirm that these additional complications to the light curve model will not affect our final solution.

We have compared our observed masses, radii, temperatures and rotational velocities to stellar evolution models of the Geneva, Utrecht, and Granada groups. We find no common match in predicted ages for mass-radius isochrones of the Geneva13 models. We find an age difference of only 0.1 Myr in predicted ages for the Geneva13 models for $\log g - \log T_{\rm eff}$ isochrones. For the Utrecht11 models, we find a marginally common predicted age with an age difference of only 0.4 Myr for the mass-radius isochrones. For the $\log g - \log T_{\rm eff}$ isochrones we find common ages of $3.5 \pm 1.5$ Myr for the Utrecht11 models. For the Granada04 models, we find a small age gap of only 0.2 for the mass-radius isochrone, when the primary star has a quite large convective overshoot of $\alpha_{\rm ov} = 0.6$. We do not find common ages for the mass-radius isochrone for the Granada04 models when the convective overshoot for both stars is a more moderate $\alpha_{\rm ov} = 0.2$.

This work suggests that models with larger convective overshoot predict a closer common age for the components of V578 Mon than models with a more conventional overshoot of $\alpha_{\rm ov} = 0.2$ pressure scale heights. Evolutionary models with larger convective overshoot extends the size of the convective core for massive stars, thus extending the main sequence lifetime and allowing for isochrones to predict a common age for V578 Mon. However - rotational mixing also can prolong the main sequence lifetime, making the two effects some what degenerate. The radii may in a small way

be dependent upon effective temperatures, which are based on imperfect atmosphere models. Furthermore, there are small systematic residuals of 0.005 mag in the light curve fits which may in a small way affect the radii. Finally, effects of binarity, while likely small, are not taken into account: the side of each star facing the other may be heated and the addition to the potential $\Omega$ from the companion is not taken into account into the models. The binarity of V578 Mon may cause single star models explored here to not be applicable.

Given the short apsidal period of V578 Mon of $33.48^{+0.10}_{-0.06}$ years, our photometry cover one full apsidal motion period. Combined with our precise measurement of the radii of V578 Mon we compute the internal structure constant $\log k_2$ finding that our observed $\log k_{2,\mathrm{obs}} = -1.975 \pm 0.017$ in agreement with the theoretical internal structure constant $\log k_{2,\mathrm{theo}} = -2.005 \pm 0.025$.

V578 Mon is a particularly important system for testing stellar evolution models given young age and the difference of $\approx$ 30% in the masses of the primary and secondary component star. B-type detached eclipsing binaries such as V1388 Ori and V1034 Sco have similar differences in mass of 40% and 50% respectively, meaning these systems are also of particular importance to providing constraints on stellar evolution models. However, V578 Mon is unique among such systems by virtue of its young age, thus providing the strongest constraints on the models at the earliest stages of massive stellar evolution.

Future work may include comparing the carefully vetted sample of high mass

EBs in the Torres et al. (2010) sample to evolutionary models, include more recent massive EBs such as V 380 Cyg (Tkachenko et al., 2014) and LMC 172231 and ST2-28 (Massey et al., 2012), to see if larger convective overshoot parameters allow for common predictions of age.

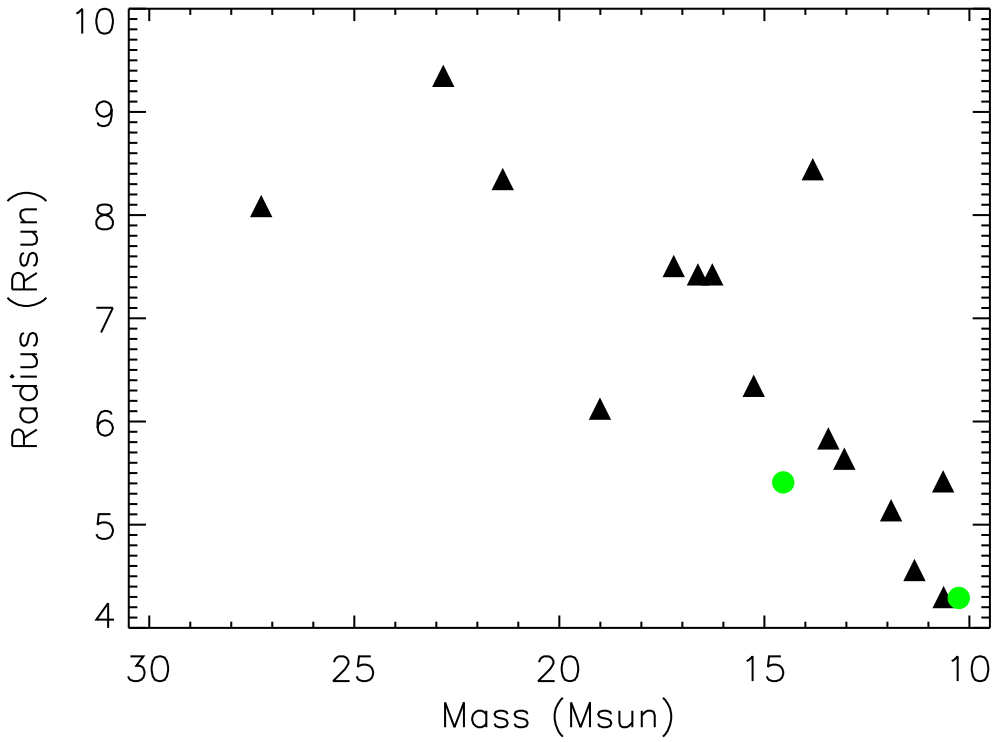


Figure 1: Massive ($> 10M_{\odot}$) detached eclipsing binaries with accurate masses and radii better than 2% are scarce. There are only 9 such systems (black triangles) including V578 Mon (green circles). This list of eclipsing binaries is adapted from Torres et al. (2010). The error bars on the mass and radii are smaller than the plotted symbols. Of these eclipsing binaries, V578 Mon is simultaneously one of the youngest and lowest mass ratios $q = \frac{M_2}{M_1}$.

Table 1. Identifications, location and combined photometric parameters for eclipsing binary V578 Mon

| | V578 Mon | Reference |
|---|---|---|
| Henry Draper number | HD 259135 | Cannon & Pickering (1923) |
| Bonner Durchmusterung | BD +04°1299 | Argelander (1903) |
| Hoag number | NGC 2244 200 | Hog et al. (1998) |
| $\alpha_{2000}$ | 06 32 00.6098 | Hog et al. (1998) |
| $\delta_{2000}$ | + 04 52 40.902 | Hog et al. (1998) |
| Spectral type | B0V + B1V | Hensberge et al. (2000) |
| $V$ | 8.542 | Ogura & Ishida (1981) |
| $V - I$ | 0.262 | Wang et al. (2008) |
| $B - V$ | + 0.165 | Ogura & Ishida (1981) |
| $U - B$ | − 0.727 | Wolff et al. (2007) |
| $V - R$ | + 0.452 | Wang et al. (2008) |

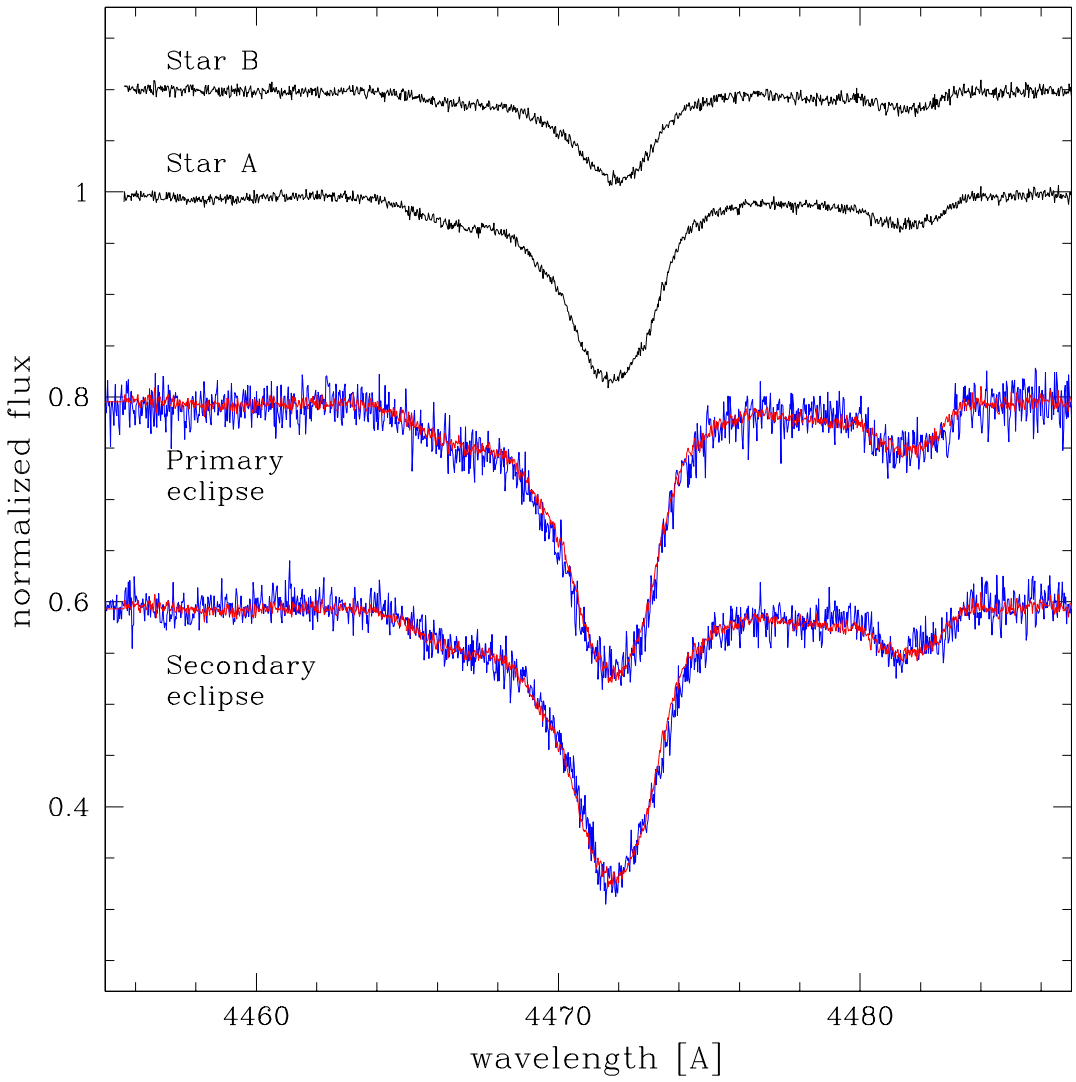


Figure 2: Fits (red) to the HERMES spectra (blue) obtained during the primary and secondary eclipse of V578 Mon. The disentangled component spectra obtained from time-series of observed spectra out-of-eclipse are shown above in black. The light ratio from the light curve analysis agrees to within uncertainty the light ratio derived from the in eclipse spectra. The light contribution of each component in the phases of the eclipses were calculated from the final light curve solution.

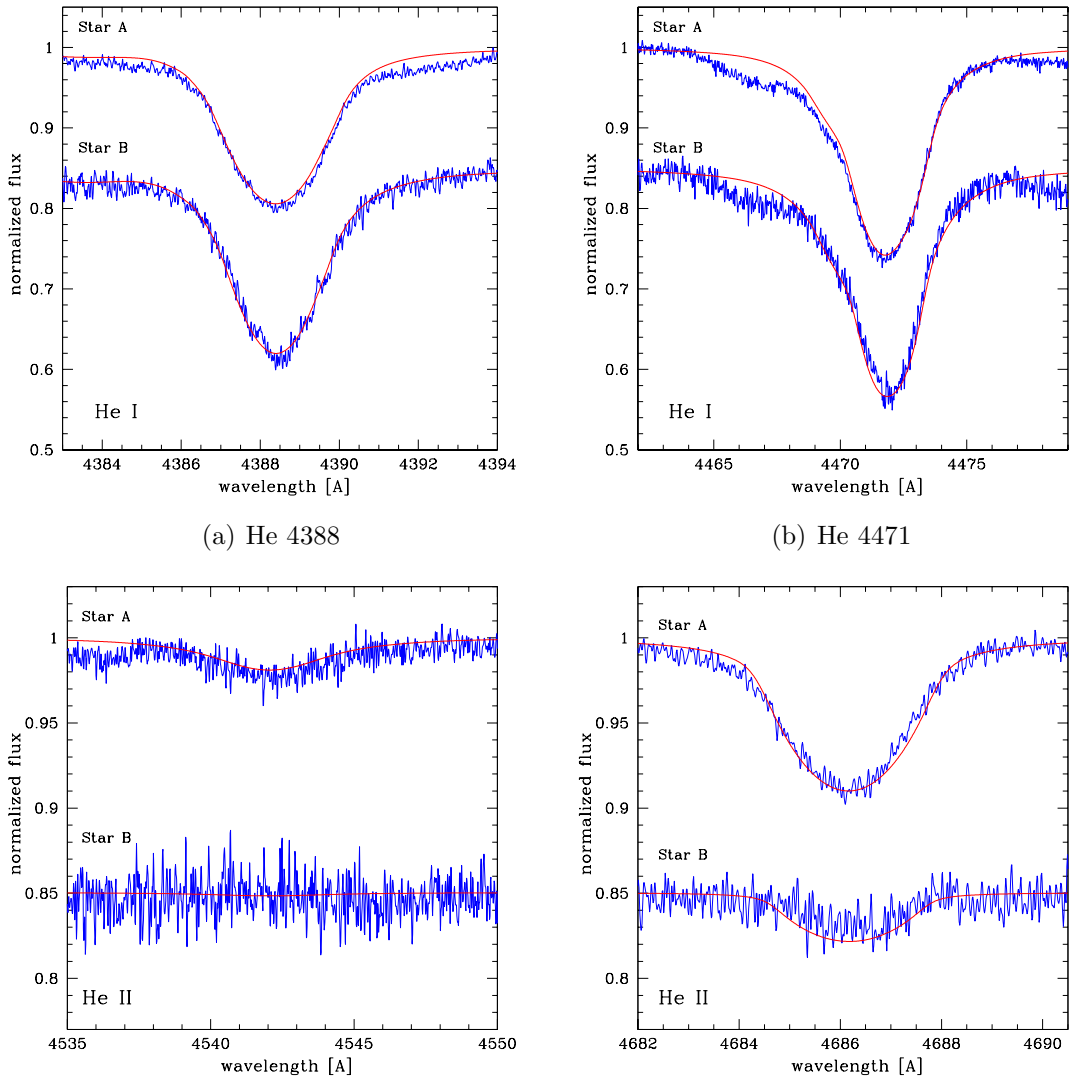


(a) He 4388

(b) He 4471

(c) He 4541

(d) He 4686

Figure 3: Optimal fitting for the four helium lines, He I 4388 Å, He I 4471 Å, He II 4541 Å, and He II 4686 Å for the out-of-eclipse HERMES spectra. In each panel helium line profiles for both components are shown (blue solid line). Optimal fitting was performed on all 4 lines simultaneously (red solid line). These are reconstructed helium profiles from disentangled spectra using the light ratio and surface gravities fixed to the final solution. A color version of this figure is available in the online journal.

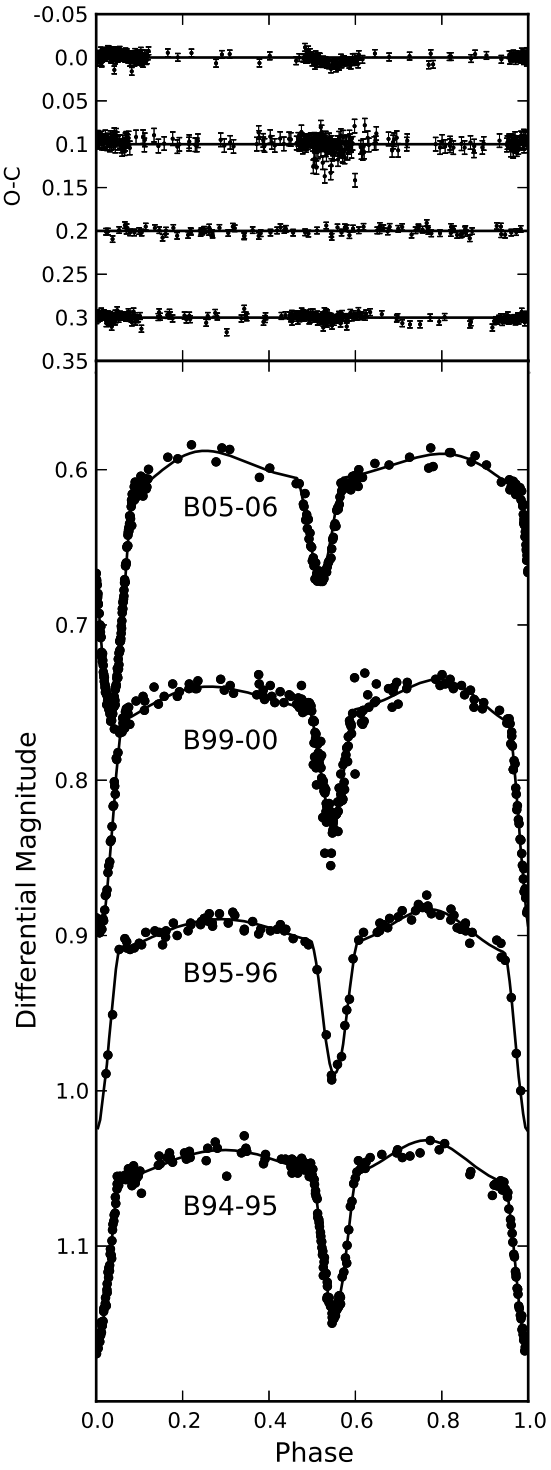


Figure 4: Representative fits to light curves from 2005–2006, 1999–2000, 1995–1996 and 1994–1995 in the Johnson $B$ passband from global fits to all light curve data, offset for clarity. The residuals to the fits $(O - C)$ are shown above.

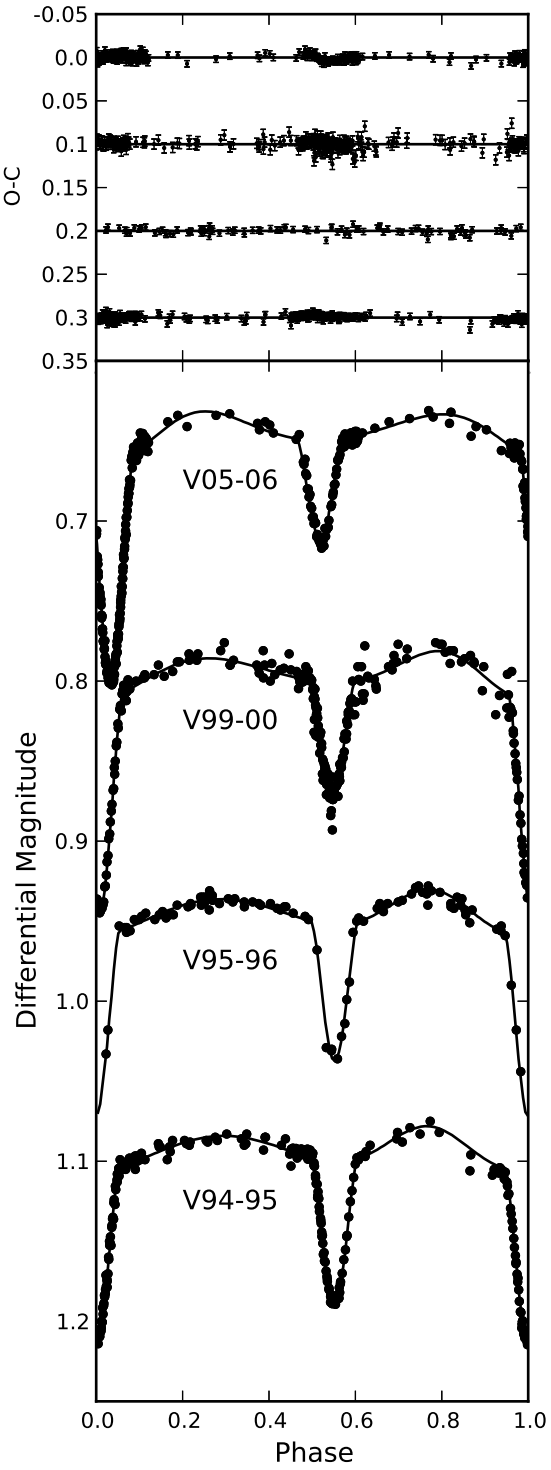


Figure 5: Same as Fig. 4, but showing Johnson $V$ band light curves and fits.

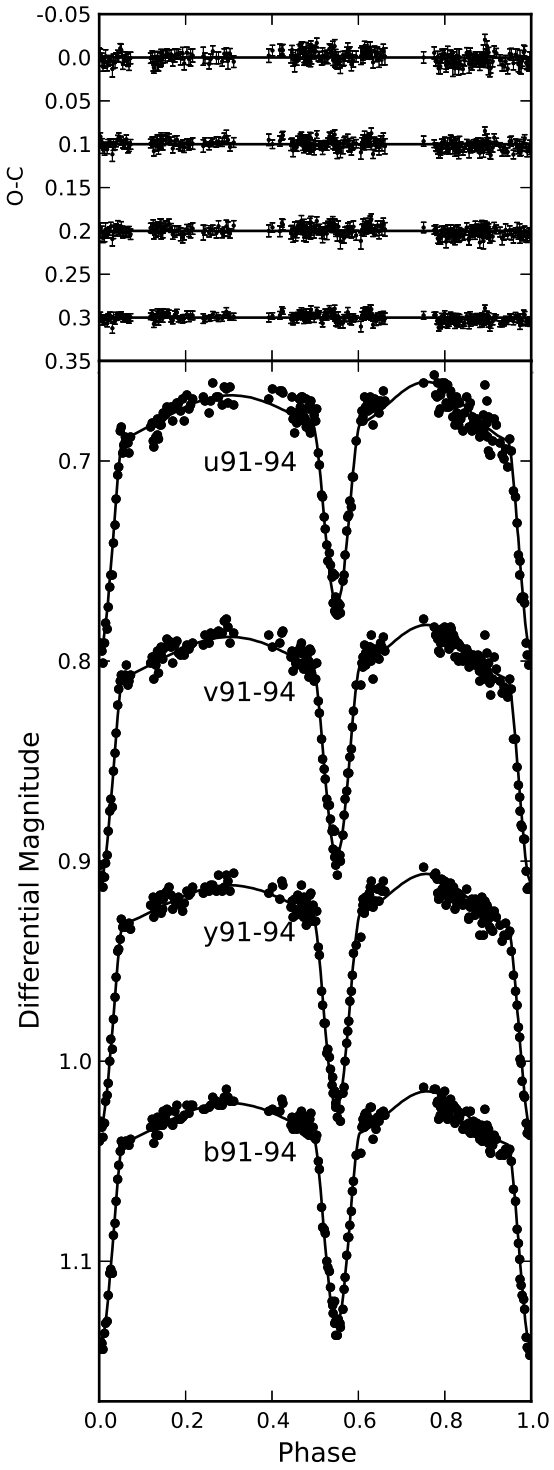


Figure 6: Same as Fig. 4, but showing Strömgren *uvby* light curves and fits.

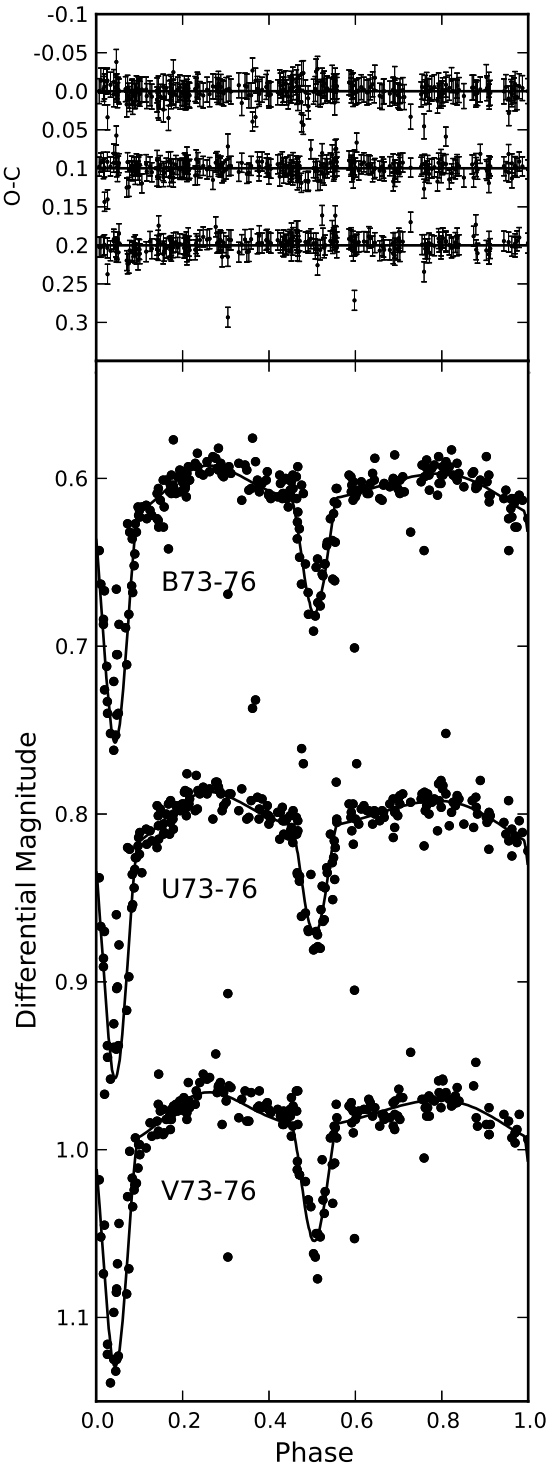


Figure 7: Same as Fig. 4, but showing 1973–1977 Johnson $UBV$ light curves and fits.

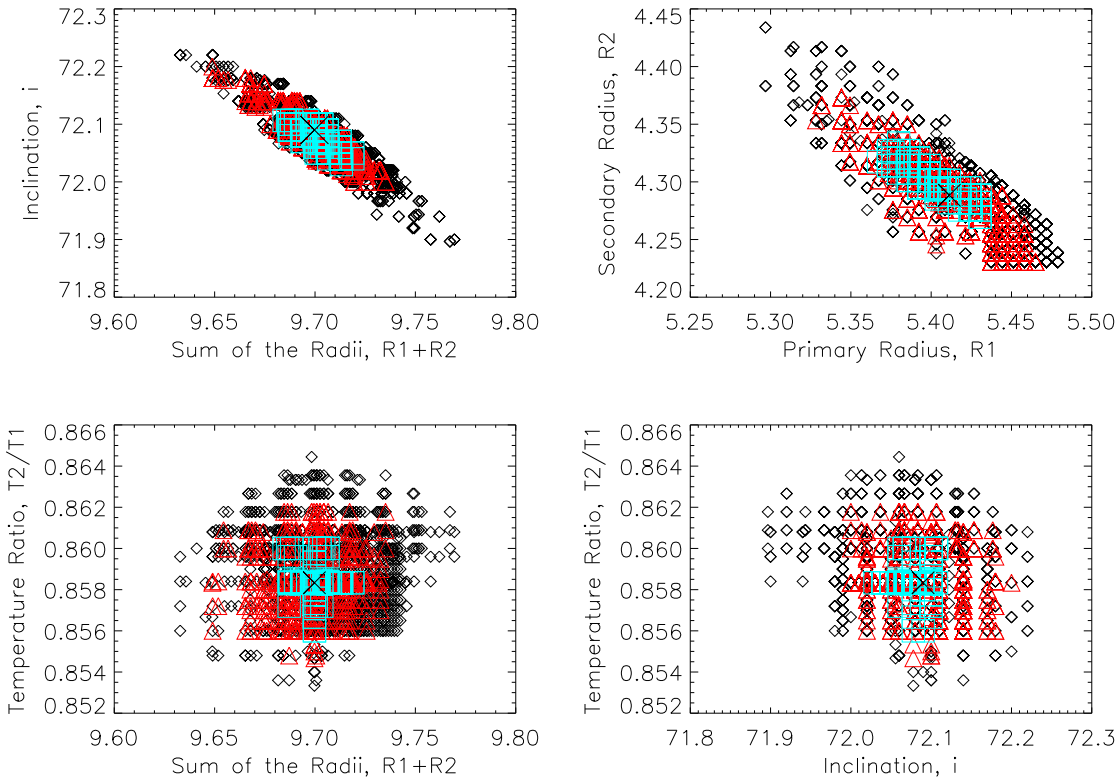


Figure 8: Degeneracies for our best fit light curve solution. The blue squares, red triangles and black diamonds correspond to difference in chi square from the global best fit solution $\Delta\chi^2 = 4.72$,9.70, and 16.3 respectively. For four parameters of interest these $\Delta\chi^2$ correspond to $1\sigma$, $2\sigma$ and $3\sigma$ respectively. There is a small degeneracy between the sum of the radii $R_1 + R_2$ and $i$. This degeneracy is typical for detached eclipsing binaries with circular or near circular orbits. Similarly, there is a small degeneracy between the primary and secondary radii $R_1$ and $R_2$. The global best fit solution is marked with an X. There is no degeneracy between the temperature ratio $\frac{T_2}{T_1}$ and inclination $i$ or sum of the radii $R_1 + R_2$. A color version of this figure is available in the online journal.

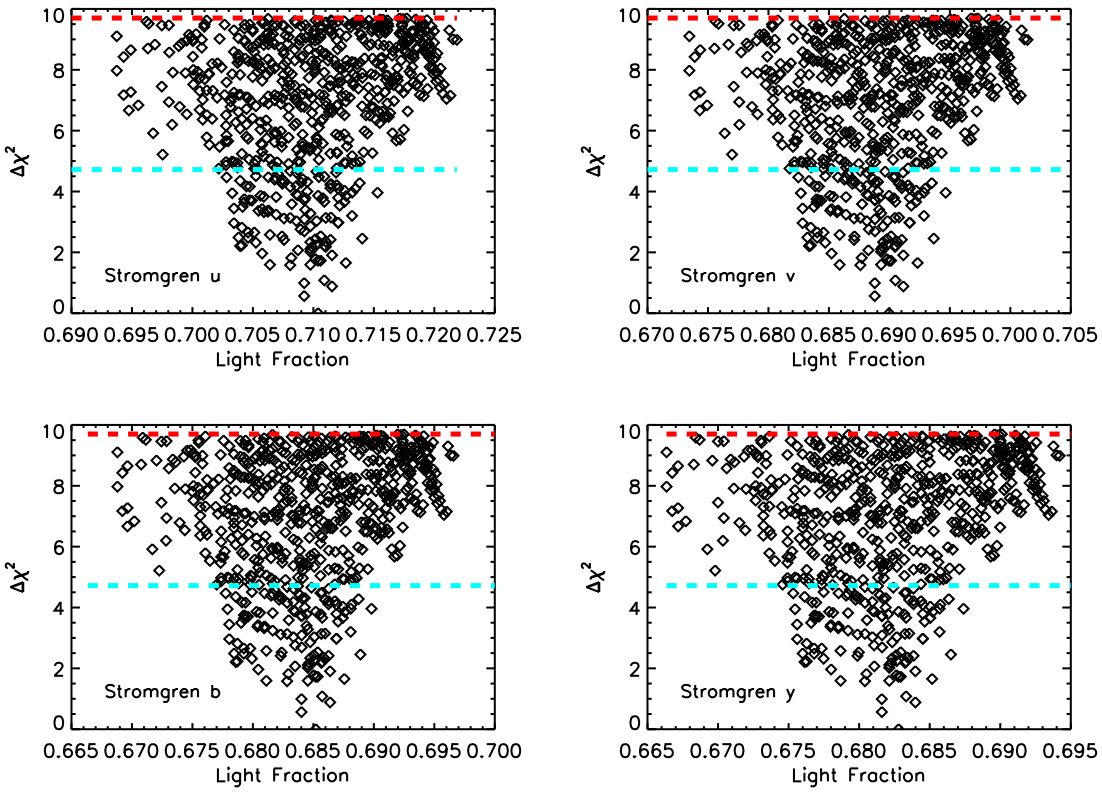


Figure 9: The light fractions $l_{f,1} = \frac{l_1(\lambda)}{l_1(\lambda)+l_2(\lambda)}$ for light curve fits within $1\sigma$ (below the blue line) and $2\sigma$ (below the red line) uncertainty for the Stromgren *uvby* photometry. Our light fractions are consistent with the light fractions computed from Hensberge et al. (2000). A color version of this figure is available in the online journal.

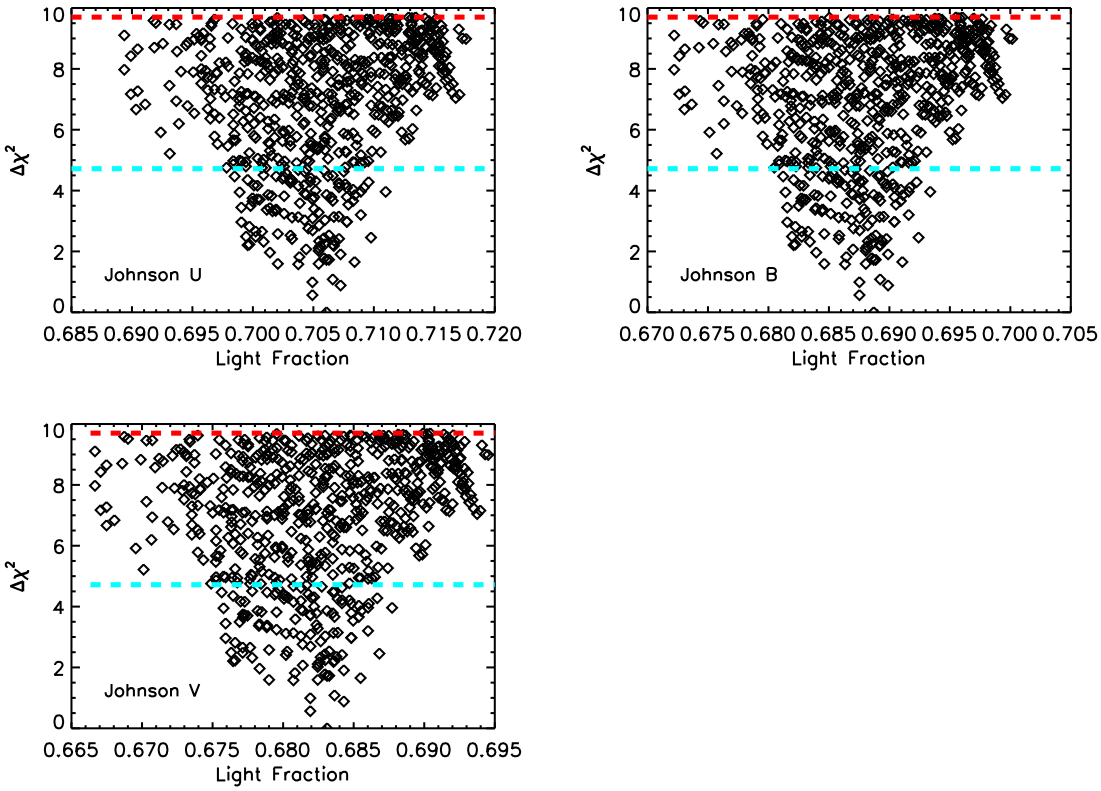


Figure 10: Same as Figure 9 except for the Johnson UBV photometry.

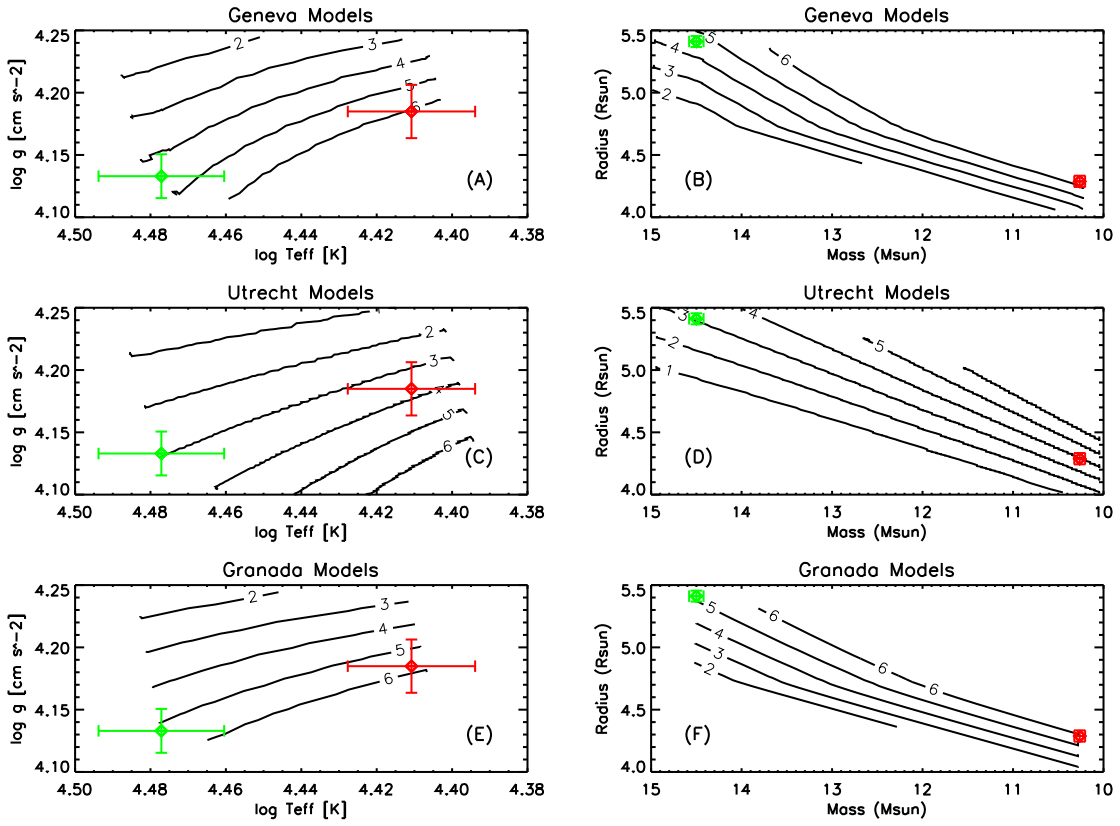


Figure 11: The best matches to observations are the Utrecht11 and Granada04 models, which both use larger than conventional overshoot of $\alpha_{\rm ov} = 0.2$ - see Table 13 for details. Isochrones are in steps of 1 Myr of the Geneva13, Utrecht11 and Granada04 models. The green point is the primary star, and the red point is the secondary star. All models have rotational velocities that match the observed velocities of V578 Mon $v_{1,\rm rot}$ =123 $\pm$ 5 km s$^{-1}$ and $v_{2,\rm rot}$ =99 $\pm$ 3 km s$^{-1}$. A color version of this figure is available in the online journal.

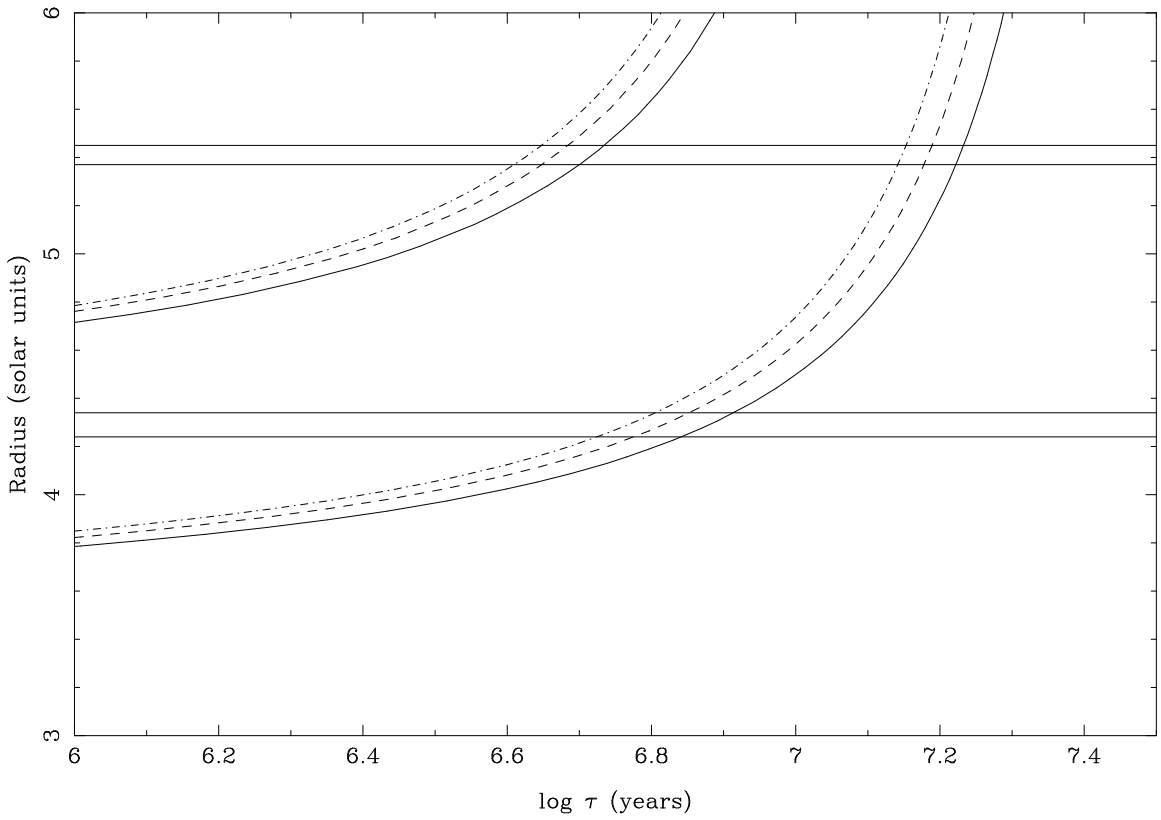


Figure 12: The time evolution of the radii for V578 Mon from Granada04 models computed for the masses of the V578 Mon primary and secondary. Dot-dashed, dashed, and solid lines are evolutionary models at convective overshoot of $\alpha_{\rm ov}$ of 0.2, 0.4 and 0.6 pressure scale heights respectively. Horizontal lines are the upper and lower limit of uncertainty on the primary star and secondary star radius respectively. The models predict a common age of 5.5 Myr - if we use a high convective overshoot of $\alpha_{\rm ov} = 0.6$ evolution model for the primary star and $\alpha_{\rm ov} = 0.2$ for the secondary star.

Table 2. V578 Mon Light Curves

| Observatory | Year | Filter | $\sigma_0$ [mag] | $\sigma$ [mag] | N |
|---|---|---|---|---|---|
| [1] KPNO | 1967-84 | Johnson $U$ | 0.004 | 0.016 | 251 |
| | | Johnson $B$ | 0.004 | 0.012 | 256 |
| | | Johnson $V$ | 0.004 | 0.013 | 217 |
| [2]SAT | 1991–94 | Strömgren $u$ | 0.0029 | 0.0067 | 248 |
| | | Strömgren $b$ | 0.0023 | 0.0046 | 248 |
| | | Strömgren $v$ | 0.0023 | 0.0054 | 248 |
| | | Strömgren $y$ | 0.0030 | 0.0053 | 248 |
| [3]APT | 1994–95 | Johnson $V$ | 0.0037 | 0.0022 | 260 |
| | | Johnson $B$ | 0.001 | 0.0040 | 254 |
| APT | 1995–96 | Johnson $V$ | 0.002 | 0.0035 | 95 |
| | | Johnson $B$ | 0.001 | 0.0037 | 96 |
| APT | 1999–2000 | Johnson $V$ | 0.002 | 0.0058 | 259 |
| | | Johnson $B$ | 0.001 | 0.0078 | 246 |
| APT | 2005–06 | Johnson $V$ | 0.002 | 0.0036 | 284 |
| | | Johnson $B$ | 0.001 | 0.0044 | 283 |

Note. — [1]16-inch telescope at Kitt Peak (KPNO)
[2]0.5 m telescope at La Silla (SAT)
[3]TSU-Vanderbilt 16-inch telescope at Fairborn University (APT)

Table 3. HERMES Observations

| Phase | BJD-2450000.000 | Exp Time [s] |
|---|---|---|
| 0.9957 | 5904.586 | 2100 |
| 0.0060 | 5904.611 | 2100 |
| 0.0168 | 5904.637 | 2100 |
| 0.0272 | 5904.662 | 2100 |
| 0.0376 | 5904.687 | 1980 |
| 0.0476 | 5904.711 | 1980 |
| 0.0613 | 5909.561 | 1500 |
| 0.0692 | 5909.580 | 1500 |
| 0.1128 | 5914.502 | 2100 |
| 0.1231 | 5914.527 | 2100 |
| 0.1530 | 5914.599 | 2100 |
| 0.1634 | 5914.624 | 2100 |
| 0.2259 | 5907.549 | 2100 |
| 0.2363 | 5907.574 | 2100 |
| 0.2803 | 5912.497 | 2100 |
| 0.2907 | 5912.522 | 2100 |
| 0.3434 | 5912.649 | 2100 |
| 0.3534 | 5912.673 | 2100 |
| 0.4432 | 5905.664 | 2100 |
| 0.4449 | 5910.485 | 2300 |
| 0.4536 | 5905.689 | 2100 |
| 0.4565 | 5910.513 | 2300 |
| 0.4673 | 5910.539 | 2100 |
| 0.4777 | 5910.564 | 2100 |
| 0.5010 | 5910.620 | 2100 |
| 0.5113 | 5910.645 | 2100 |

Table 3 (cont'd)

| Phase | BJD-2450000.000 | Exp Time [s] |
|---|---|---|
| 0.6427 | 5908.553 | 2200 |
| 0.6535 | 5908.579 | 2200 |
| 0.7187 | 5913.553 | 2100 |
| 0.7291 | 5913.578 | 2100 |
| 0.7945 | 5906.510 | 2100 |
| 0.8049 | 5906.535 | 2100 |
| 0.9278 | 5911.648 | 2200 |
| 0.9390 | 5911.675 | 2200 |

Note. — Time-series HERMES spectroscopy of V578 Mon. Each exposure is less than 0.01 of the orbital period for V578 Mon of 2.4084822 days. The time series spectra were obtained to cover the out-of-eclipse, primary eclipse and secondary eclipse phases.

Table 4. Radial Velocity Solutions

| | $q$ | $K_1$ [km s$^{-1}$] | $K_2$ [km s$^{-1}$] | $e$ |
|---|---|---|---|---|
| Hensberge et al. (2000) (LC+Spectroscopy) | 0.7078±0.0002 | 259.8 | 183.9 | 0.0867 |
| Hensberge et al. (2000) RV only | 0.705±0.004 | 259.8±0.8 | 184.4 | 0.0836±0.0008 |
| HERMES Spectra, $e$ fixed | 0.710 | 259.8 | 184.5 | 0.07755 |
| HERMES Spectra, $e$ and $\omega$ fixed | 0.709 | 259.4 | 184.0 | 0.07755 |

Table 5. Light Fraction Comparison

| Method | Wavelength $\lambda$ [nm] | Light Fraction $\frac{l_1}{l_1+l_2}$ |
|---|---|---|
| Light Curve Analysis (this work) | Johnson U, 365 | $0.706 \pm 0.008$ |
| | Johnson B, 445 | $0.689 \pm 0.007$ |
| | Johnson V, 551 | $0.683 \pm 0.007$ |
| | Stromgren u, 365 | $0.710 \pm 0.007$ |
| | Stromgren v, 411 | $0.690 \pm 0.008$ |
| | Stromgren b, 467 | $0.685 \pm 0.007$ |
| | Stromgren y, 547 | $0.683 \pm 0.007$ |
| Hensberge et al. (2000) | Stromgren v, 411 | $0.675 \pm 0.006$ |
| | Stromgren b, 467 | $0.683 \pm 0.006$ |
| | Stromgren y, 547 | $0.692 \pm 0.006$ |
| HERMES Spectroscopy | 400-500 | $0.700 \pm 0.02$ |

Table 6. Light Curve Parameter Ranges Explored

| Parameter | Max | Min | Coarse Grid Spacing | Fine Grid Spacing |
|---|---|---|---|---|
| Primary Surface Potential, $\Omega_1$ | 5.36 | 4.80 | 0.045 | 0.005 |
| Secondary Surface Potential, $\Omega_2$ | 5.26 | 4.40 | 0.045 | 0.005 |
| Inclination, $i$ [deg] | 73.15 | 70.00 | 0.2 | 0.0005 |
| Temperature Ratio, $\frac{T_2}{T_1}$ | 0.875 | 0.843 | 0.0012 | 0.03 |

Table 7. Light Curve Analysis Results and Comparison

| Light Curve Parameters | This Work & Garcia et al. (2011) | H2000 |
|---|---|---|
| Primary Surface Potential, $\Omega_1$ | $4.88 \pm 0.03$ | $5.02 \pm 0.05$ |
| Secondary Surface Potential, $\Omega_2$ | $4.89 \pm 0.04$ | $4.87 \pm 0.06$ |
| Temperature Ratio, $\frac{T_2}{T_1}$ | $0.858 \pm 0.002$ | $0.88 \pm 0.02$ |
| Inclination, $i$ [deg] | $72.09 \pm 0.06$ | $72.58 \pm 0.3$ |
| Eccentricity, $e$ | $0.07755^{+0.00018}_{-0.00026}$ | $0.0867 \pm 0.0006$ |
| Angle of Periastron, $w$ [deg] | $159.8 \pm 0.33$ | $153.3 \pm 0.6$ |
| Ephemeris, $HJD_0$ [d] | 2449360.6250 | 2449360.6250 |
| Total Apsidal Motion, $\dot{\omega}_{\rm tot}$ [deg cycle$^{-1}$] | $0.07089^{+0.00021}_{-0.00013}$ | |
| Light Curve Filters | Strömgren $uvby$, Johnson $UBV$ | Strömgren $uvby$ |
| Total Light Curve Points | 3489 | 992 |

Note. — The uncertainties on light curve parameters $\Omega_1$, $\Omega_2$, $i$ and $\frac{T_2}{T_1}$ are determined from confidence intervals in Figure 8. Light curve parameters $e$, $w$ and $\dot{\omega}_{\rm tot}$ are taken from Garcia et al. (2011). This work utilizes photometry that span one full apsidal motion period (U=$33.48^{+0.10}_{-0.06}$yr). In contrast to the Hensberge et al. (2000) analysis, this work incorporates apsidal motion in the light curve model. Finally, the temperature ratio from Hensberge et al. (2000) is measured from spectral disentangling.

Table 8. Limb Darkening Coefficients

| Filter | $x_1$ | $x_2$ | $y_1$ | $y_2$ |
|---|---|---|---|---|
| Square Root Law (adopted) | | | | |
| Strömgren $u$ | -0.096 | -0.073 | 0.631 | 0.606 |
| Strömgren $b$ | -0.132 | -0.115 | 0.672 | 0.659 |
| Strömgren $v$ | -0.129 | -0.106 | 0.607 | 0.581 |
| Strömgren $y$ | -0.073 | -0.044 | 0.612 | 0.581 |
| Johnson $U$ | -0.131 | -0.115 | 0.685 | 0.675 |
| Johnson $B$ | -0.131 | -0.110 | 0.654 | 0.638 |
| Johnson $V$ | -0.126 | -0.105 | 0.602 | 0.578 |
| Linear Law | | | | |
| Strömgren $u$ | 0.282 | 0.291 | 0.000 | 0.000 |
| Strömgren $b$ | 0.272 | 0.281 | 0.000 | 0.000 |
| Strömgren $v$ | 0.235 | 0.243 | 0.000 | 0.000 |
| Strömgren $y$ | 0.293 | 0.304 | 0.000 | 0.000 |
| Johnson $U$ | 0.280 | 0.291 | 0.000 | 0.000 |
| Johnson $B$ | 0.262 | 0.273 | 0.000 | 0.000 |
| Johnson $V$ | 0.235 | 0.242 | 0.000 | 0.000 |
| Logarithmic Law | | | | |

Table 8 (cont'd)

| Filter | $x_1$ | $x_2$ | $y_1$ | $y_2$ |
|---|---|---|---|---|
| Strömgren $u$ | 0.450 | 0.452 | 0.252 | 0.242 |
| Strömgren $b$ | 0.450 | 0.457 | 0.268 | 0.264 |
| Strömgren $v$ | 0.397 | 0.398 | 0.242 | 0.233 |
| Strömgren $y$ | 0.456 | 0.459 | 0.244 | 0.232 |
| Johnson $U$ | 0.462 | 0.471 | 0.274 | 0.270 |
| Johnson $B$ | 0.436 | 0.444 | 0.261 | 0.256 |
| Johnson $V$ | 0.395 | 0.396 | 0.241 | 0.231 |

Note. — Our best fit model uses the square root limb darkening law. Fits with the linear cosine or logarithmic limb darkening law had little effect on our final light curve solution.

Table 9. A comparison of light curve models

| Model | $\Omega_1$ | $\Omega_2$ | $i$ [deg] | $\frac{T_2}{T_1}$ | $\chi^2$ |
|---|---|---|---|---|---|
| Best Fit | $4.88 \pm 0.03$ | $4.89 \pm 0.04$ | $72.09 \pm 0.06$ | $0.858 \pm 0.002$ | 3489.00 |
| Fitting for LD coefficients | 4.92 | 4.89 | 72.18 | 0.835 | 3299.11 |
| Linear Law | 4.92 | 4.89 | 72.15 | 0.860 | 3480.01 |
| Logarithmic Law | 4.91 | 4.88 | 72.14 | 0.858 | 3503.96 |
| Fix $T_1 = 28500$ | 4.94 | 4.87 | 72.17 | 0.857 | 3460.16 |
| Fix $T_1 = 31500$ | 4.92 | 4.89 | 72.15 | 0.867 | 3488.01 |
| Light Reflection | 4.90 | 4.92 | 72.20 | 0.856 | 3522.57 |
| Third Light | 4.94 | 4.87 | 72.24 | 0.855 | 3414.93 |

Note. — The best fit model uses the square root limb darkening law, a fixed $T_1$ =30000 K, no light reflection, and no third light.

Table 10. Third Light

| Observatory | Year | Filter | $\frac{L_3}{L_{\rm tot}}$ |
|---|---|---|---|
| APT | 2005–06 | Johnson $B$ | 0.0441 |
| | | Johnson $V$ | 0.0218 |
| APT | 1999–2000 | Johnson $B$ | 0.0158 |
| | | Johnson $V$ | 0.0080 |
| APT | 1995–96 | Johnson $B$ | -0.0037 |
| | | Johnson $V$ | 0.0104 |
| APT | 1994–95 | Johnson $B$ | 0.0059 |
| | | Johnson $V$ | 0.0046 |
| SAT | 1991–94 | Strömgren $u$ | -0.0116 |
| | | Strömgren $v$ | -0.0004 |
| | | Strömgren $b$ | 0.0013 |
| | | Strömgren $y$ | -0.0045 |
| KPNO | 1967-84 | Johnson $U$ | 0.0163 |
| | | Johnson $B$ | 0.0467 |
| | | Johnson $V$ | -0.0100 |

Note. — Our best fit light curve model includes no third light. The small amount of third light varies as a function of epoch.

Table 11. V578 Mon Absolute Dimensions

| Parameter | Primary | Secondary |
|---|---|---|
| Orbital Period, P [d] | 2.4084822 | |
| Mass, $M$ $[M_\odot]$ | $14.54 \pm 0.08$ | $10.29 \pm 0.06$ |
| Radius, $R$ $[R_\odot]$ | $5.41 \pm 0.04$ | $4.29 \pm 0.05$ |
| Effective Temperature, $T_{\rm eff}$ [K] | $30000 \pm 500$ | $25750 \pm 435$ |
| Surface Gravity, $\log g$ [cm s$^{-2}$] | $4.133 \pm 0.018$ | $4.185 \pm 0.021$ |
| Surface Velocity, $v_{\rm rot}$ [km s$^{-1}$] | $123 \pm 5$ | $99 \pm 3$ |
| Luminosity, $\log \frac{L}{L_\odot}$ | $4.33 \pm 0.03$ | $3.86 \pm 0.03$ |
| Synchronicity Parameter, $F = \frac{w}{w_{orb}}$ | $1.08 \pm 0.04$ | $1.10 \pm 0.03$ |
| Apsidal Period, U [yr] | $33.48^{+0.10}_{-0.06}$ | |
| Observed Newtonian Internal Structure Constant, $\log k_{2,\rm newt}$ | $-1.975 \pm 0.017$ | |

Table 12. Stellar Evolution Models Comparison

| Physical Input | Geneva13 | Utrecht11 | Granada04 |
|---|---|---|---|
| Composition [Z,Y,X] | [0.014,0.266,0.720] | [0.0122,0.2486,0.7392] | [0.014,0.271,0.715] |
| Overshoot, $\alpha_{\rm ov}$ | 0.10 | 0.355 | 0.6 pri, 0.2 sec |
| Mixing Length, $\alpha_{\rm MLT}$ | 1.60 | 1.5 | 1.68 |
| Rotation | Yes | Yes | Yes |
| Rotational Mixing | Yes | Yes | No |
| Opacities | Iglesias & Rogers (1996) | Iglesias & Rogers (1996) | Iglesias & Rogers (1996) |
| Mass loss | Vink et al. (2001) | Vink et al. (2001) | Vink et al. (2001) |

Table 13. Ages from Stellar Evolution Models

| Model | Primary Age [Myr] | Secondary Age [Myr] | Age Diff (lower limit) [Myr] | $\alpha_{\rm ov}$ [Scale height] |
|---|---|---|---|---|
| | | Mass−Radius−$v_{\rm rot}$ Isochrones | | |
| Geneva13 | 4.3−4.6 | 6.2−7.1 | 1.6 | 0.1 |
| Utrecht11 | 3.0−3.2 | 3.6−4.4 | 0.4 | 0.355 |
| Granada04 | 5.0−5.3 | 5.5−6.3 | 0.2 | 0.6 pri, 0.2 sec |
| | | $\log g$-$\log T_{\rm eff}$-$v_{\rm rot}$ Isochrones | | |
| Geneva13 | 3.9−5.1 | 5.2−7.5 | 0.1 | 0.1 |
| Utrecht11 | 2.6−3.8 | 2.4−5.2 | Common age $3.5 \pm 1.5$ | 0.355 |
| Granada04 | 4.7−5.5 | 4.9−6.8 | Common age $5.5 \pm 1.0$ | 0.6 pri, 0.2 sec |

Note. — The ages for the primary and secondary star are computed from evolutionary tracks at the masses of either star and solar metallicity. The Granada04 models were computed for a high convective overshoot of $\alpha_{\rm ov} = 0.6$ pressure scale heights for the primary star, which allowed the models to match the observations. It easier to find a common age for the $\log g - \log T_{\rm eff}$ isochrone given the larger uncertainty on the effective temperatures of the stars.

# REFERENCES


Argelander, F. W. A. 1903, Eds Marcus and Weber's Verlag, Bonn (1903), 0

Asplund, M., Grevesse, N., Sauval, A. J., & Scott, P. 2009, ARA&A, 47, 481

Avni, Y. 1976, ApJ, 210, 642

Bell, S. A., Hilditch, R. W., & Adamson, A. J. 1986, MNRAS, 223, 513

Bouzid, M. Y., Sterken, C., & Pribulla, T. 2005, A&A, 437, 769

Butler, K., & Giddings, J. R. 1985, Newsletter of Analysis of Astronomical Spectra, No. 9

Brott, I., de Mink, S. E., Cantiello, M., et al. 2011, A&A, 530, A115

Cannon, A. J., & Pickering, E. C. 1923, Annals of Harvard College Observatory, 98, 1

Castelli, F., Gratton, R. G., & Kurucz, R. L. 1997, A&A, 318, 841

Claret, A. 1999, A&A, 350, 56

Claret, A. 2000, A&A, 363, 1081

Claret, A. 2004, A&A, 424, 919

Claret, A. 2006, A&A, 453, 769

Claret, A. 2007, A&A, 475, 1019

Claret, A., & Giménez, A. 2010, A&A, 519, A57

Diaz-Cordoves, J., & Gimenez, A. 1992, A&A, 259, 227

Evans, C. J., Smartt, S. J., Lee, J.-K., et al. 2005, A&A, 437, 467

Ekström, S., Georgy, C., Eggenberger, P., et al. 2012, A&A, 537, A146

Garcia, E. V., Stassun, K. G., Hebb, L., Gómez Maqueo Chew, Y., & Heiser, A. 2011, AJ, 142, 27

Garcia, E. V., Stassun, K. G., & Torres, G. 2013, ApJ, 769, 114

Georgy, C., Ekström, S., Granada, A., et al. 2013, A&A, 553, A24

Gómez Maqueo Chew, Y., Stassun, K. G., Prša, A., et al. 2012, ApJ, 745, 58

Hadrava, P., 1995, A&AS, 114, 393

Heiser, A. M. 1977, AJ, 82, 973

Heiser, A. M. 2010, Journal of the American Association of Variable Star Observers, 38, 93

Hensberge, H., Pavlovski, K., & Verschueren, W. 2000, A&A, 358, 553

Hunter, I., Dufton, P. L., Smartt, S. J., et al. 2007, A&A, 466, 277

Hog, E., Kuzmin, A., Bastian, U., et al. 1998, A&A, 335, L65

Holmgren, D. E., Hill, G., & Fisher, W. 1990, A&A, 236, 409

Iglesias, C. A., & Rogers, F. J. 1996, ApJ, 464, 943

Ilijic, S., Hensberge, H., Pavlovski, K., & Freyhammer, L. M. 2004, Spectroscopically and Spatially Resolving the Components of the Close Binary Stars, 318, 111

Kramm, U., Nettelmann, N., Redmer, R., & Stevenson, D. J. 2011, A&A, 528, A18

Lyubimkov, L. S., Rostopchin, S. I., Rachkovskaya, T. M., Poklad, D. B., & Lambert, D. L. 2005, MNRAS, 358, 193

Massey, P., Morrell, N. I., Neugent, K. F., et al. 2012, ApJ, 748, 96

Nieva, M.-F., & Przybilla, N. 2012, A&A, 539, A143

Nieva, M. F., & Przybilla, N. 2007, A&A, 467, 295

Ogura, K., & Ishida, K. 1981, PASJ, 33, 149

Pavlovski, K., & Hensberge, H. 2005, A&A, 439, 309

Pavlovski, K., Tamajo, E., Koubský, P., et al. 2009, MNRAS, 400, 791

Pribulla, T., Rucinski, S. M., Latham, D. W., et al. 2010, Astronomische Nachrichten, 331, 397

Popper, D. M. 1974, ApJ, 188, 559

Popper, D. M., & Hill, G. 1991, AJ, 101, 600

Popper, D. M., & Etzel, P. B. 1981, AJ, 86, 102

Prša, A., & Zwitter, T. 2005, ApJ, 628, 426

Press, W. H., Teukolsky, S. A., Vetterling, W. T. and Flannery, B. P., 1988, Numerical Recipes in C, Second Edition, Cambridge University Press, NY, pg 697.

Raskin, G., van Winckel, H., Hensberge, H., et al. 2011, A&A, 526, A69

Song, H. F., Maeder, A., Meynet, G., et al. 2013, A&A, 556, A100

Stickland, D. J., Koch, R. H., & Pfeiffer, R. J. 1992, The Observatory, 112, 277

Southworth, J., Maxted, P. F. L., & Smalley, B. 2004, MNRAS, 351, 1277

Sterne, T. E. 1939, MNRAS, 99, 451

Tamajo, E., Pavlovski, K., & Southworth, J. 2011, A&A, 526, A76

Tkachenko, A., Degroote, P., Aerts, C., et al. 2014, MNRAS, 438, 3093

Torres, G., Andersen, J., & Giménez, A. 2010, A&A Rev., 18, 67

Wang, J., Townsley, L. K., Feigelson, E. D., et al. 2008, ApJ, 675, 464

Wilson, R. E. & Devinney, E. J. 1971, ApJ, 166, 605

Wilson, R. E. 1979, ApJ, 234, 1054

Willems, B., & Claret, A. 2002, A&A, 382, 1009

Wolff, S. C., Strom, S. E., Dror, D., & Venn, K. 2007, AJ, 133, 1092

van Hamme, W. 1993, AJ, 106, 2096

Vink, J. S., de Koter, A., & Lamers, H. J. G. L. M. 2001, A&A, 369, 574

von Zeipel, H. 1924, MNRAS, 84, 665

# CHAPTER III

## Testing Brown Dwarf Stellar Formation Models with High Contrast Imaging

**This paper appears as: Garcia et al.(2015), On the Binary Frequency of the Lowest Mass Members of the Pleiades with *Hubble Space Telescope* Wide Field Camera 3, Astrophysical Journal, 804, 65**

### 3.1 Summary

We present the results of a *Hubble Space Telescope* Wide Field Camera 3 imaging survey of 11 of the lowest mass brown dwarfs in the Pleiades known ($25 - 40$ $M_{Jup}$). These objects represent the predecessors to T dwarfs in the field. Using a semi-empirical binary PSF-fitting technique, we are able to probe to $0\farcs03$ (0.75 pixel), better than 2x the WFC3/UVIS diffraction limit. We did not find any companions to our targets. From extensive testing of our PSF-fitting method on simulated binaries, we compute detection limits which rule out companions to our targets with mass ratios of $q \gtrsim 0.7$ and separations $a \gtrsim 4$ AU. Thus, our survey is the first to attain the high angular resolution needed to resolve brown dwarf binaries in the Pleiades at separations that are most common in the field population. We constrain the binary frequency over this range of separation and mass ratio of $25 - 40$ $M_{Jup}$ Pleiades brown dwarfs to be <11% for $1\sigma$ (<26% at $2\sigma$). This binary frequency is consistent

with both younger and older brown dwarfs in this mass range.

## 3.2 Introduction

Hundreds of brown dwarfs have now been identified in the solar neighborhood through wide-field surveys (e.g. DENIS, 2MASS, SDSS, UKIDSS, Pan-STARRS and WISE) and in nearby star-forming regions (e.g., Epchtein et al., 1997; Delfosse et al., 1997; Chiu et al., 2006; Allers et al., 2006; Bihain et al., 2006; Reid et al., 2008; Bihain et al., 2010; Burningham et al., 2010; Cushing et al., 2011; Liu et al., 2011; Lodieu et al., 2012; Burningham et al., 2013). The study of brown dwarf binarity is a fundamental tool for testing theory, given that the statistical properties of binaries probe formation scenarios in the very low-mass regime (e.g., Burgasser et al., 2007; Bate, 2009; Luhman, 2012; Bate, 2012). For the past decade, *HST* and ground-based adaptive optics (AO) have fueled such studies by searching for binaries among field ($0.5 - 5.0$ Gyr) brown dwarfs, (e.g., Martín et al., 1998; Burgasser et al., 2003; Bouy et al., 2003; Burgasser et al., 2006; Liu et al., 2006) and in young ($1 - 10$ Myr) star-forming regions such as Upper Sco (Kraus et al., 2005; Bouy et al., 2006b; Biller et al., 2011; Kraus & Hillenbrand, 2012), Taurus (e.g. Kraus et al., 2006; Konopacky et al., 2007; Todorov et al., 2010; Kraus & Hillenbrand, 2012; Todorov et al., 2014), and Chamaeleon I (e.g. Neuhäuser et al., 2002; Luhman, 2004; Lafrenière et al., 2008; Ahmic et al., 2007; Luhman, 2007). Multiplicity studies have also been performed in older ($\approx$400 Myr) regions such as Coma Ber, Praesepe, and the Hyades (Kraus &

Hillenbrand, 2007; Duchêne et al., 2013).

Previous work has shown that the binary frequency decreases and typical mass ratios increase going to lower mass primaries (Burgasser et al., 2007). One surprising finding is that these properties apparently differ between young and old binaries, with the binary frequency enhanced at young ages by a factor of $\approx 2\times$ (e.g., Lafrenière et al., 2008) and with wide separations ($\approx 10 - 1000$ AU) being much more common as compared to field brown dwarf binaries that are rarely wider than 10 AU (e.g. Burgasser et al., 2006; Close et al., 2007). An unambiguous physical explanation for this difference is lacking, as even relatively wide binaries in young star-forming regions (Luhman, 2004; Luhman et al., 2009) are not expected to incur dynamical interactions of sufficient intensity to reduce their frequency and truncate their separation distribution.

The Pleiades open cluster serves as an important bridge between the youngest ($1 - 10$ Myr) brown dwarfs and the field population. It has several advantages, such as its well established age of $\approx$125 Myr (Stauffer et al., 1998; Barrado y Navascués et al., 2004) and distance of 136.2$\pm$1.2 pc (Melis et al., 2014). There are many surveys that have searched for brown dwarf binaries in the Pleiades (Martín et al., 2000; Dobbie et al., 2002; Jameson et al., 2002; Nagashima et al., 2003; Moraux et al., 2003; Bouy et al., 2006a). However, there are only 4 Pleiades brown dwarfs with primary masses $\lesssim$40 $M_{Jup}$ that have been searched for companions to date (Moraux et al., 2003; Bouy et al., 2006a). At such masses, these objects will cool to T dwarfs

at ages of the field population.

In this work, we triple the number of low mass Pleiades brown dwarfs searched for companions, surveying a sample of 11 previously unobserved L dwarfs in the Pleiades using *HST*/WFC3. We computed detection limits for our sample using a binary fitting technique and Tiny Tim PSF models. We compared our binary frequency to the observed frequencies for brown dwarfs at similar masses in Taurus, Chamaeleon I, Upper Scorpius, and the field population.

## 3.3 Observations

### 3.3.1 Sample

We obtained images of 11 Pleiades brown dwarfs using the Hubble Space Telescope (*HST*) with the UVIS channel of Wide Field Camera 3 (WFC3/UVIS) in January and February of 2012 (GO 12563, PI Dupuy). Our sample consists of the faintest ($K \gtrsim 16$ mag), latest type ($\gtrsim$M9) members of the Pleiades known in early 2011. According to BT-Settl models of Allard (2014) tied to the COND evolutionary models of Baraffe et al. (1997, 1998, 2003), the estimated masses of our sample are $25-40$ $M_{Jup}$ based on their $K-$band magnitudes and the age of the Pleiades. When defining our sample, we considered objects bona-fide members of the Pleiades if they had proper motion indicating cluster membership and spectra with low surface gravity features or lithium absorption. Our sample is listed in Table 14, along with 4 targets from previous *HST*/ACS and *HST*/WFPC2 observations of Pleiades brown dwarfs by Martín et

al. (2003) and Bouy et al. (2006a) that match our membership criteria. All of our sample have proper motions consistent with the Pleiades cluster (Bihain et al., 2006; Casewell et al., 2007; Lodieu et al., 2012). BRB 17, BRB 21, PLIZ 35, BRB 23 and BRB 29 have spectral types L0-L4.5 from Bihain et al. (2010).

### 3.3.2 *HST*/WFC3 Imaging

We obtained 2 exposures each in filters F814W and F850LP for each target star. One image of brown dwarf BRB 17 was lost due to a pointing error so we had a total of 43 images. The target stars are positioned near the center of the full field of view at ≈250 pixels from the bottom of chip 1. We chose a longer exposure time of 900 s in F814W filter, where we are sensitive to tighter brown dwarf binaries because of the smaller PSF. We also obtained 340 s exposures in F850LP to confirm the presence of any candidate companions and measure their colors. The full width half maximum of the PSF is ≈1.84 pixels in F814W and ≈1.96 pixels in F850LP according to the WFC3 data handbook[1].

We inspected each image for cosmic rays hits, identified as rays or streaks with high counts but not resembling WFC3 point sources. We found 6 of the 43 images had cosmic ray hits within 5 pixels of the target star. We use the Laplacian Cosmic Ray Identification algorithm `LACOSMIC` (van Dokkum, 2001) to remove cosmic rays from a 200×200 pixel area on the detector centered on the target star. `LACOSMIC` replaces

[1] `http://www.stsci.edu/hst/wfc3/documents/handbooks/currentIHB/`

each pixel with the median of the surrounding pixels in an iterative procedure. Visual inspection after the fact confirms that we successfully cleared all obvious cosmic ray hits except for a single image of brown dwarf BRB 23 in F850LP due to a cosmic ray hit through the center of the peak of the target. We excluded this image of BRB 23 in the subsequent data analysis, therefore leaving us with 42 images total for the rest of our analysis.

We computed aperture photometry of our targets from the pipeline calibrated, geometrically-corrected, dither-combined (drz) images. We calculated our aperture photometry using the `APER` task from the IDL Astronomy User's Library[2] for an aperture radius of $0\farcs4$ and a sky annulus of $0\farcs4 - 0\farcs8$. We converted the flux in our aperture to a Vega magnitude using zeropoints of 24.57 mag for the F814W filter and 23.20 mag for the F850LP filter provided in the *HST*/WFC3 webpages[3]. To determine our photometric uncertainties, we first constructed an error image for each image, accounting for read noise and poisson noise. Using a Monte Carlo approach, we determined our photometric errors from $10^4$ iterations of the `APER` task after adding random Gaussian noise to the image in each iteration. The resulting F814W and F850LP photometry for our targets is listed in Table 15.

[2] `http://idlastro.gsfc.nasa.gov/homepage.html`
[3] `http://www.stsci.edu/hst/wfc3/phot_zp_lbn`

## 3.4 Image Analysis

### 3.4.1 Point Spread Function (PSF) Model of WFC3/UVIS

In order to search for close companions to our targets, we began by fitting a model Tiny Tim (Krist et al., 2011) point spread function to our imaging data. To create the most accurate model we specified the exact coordinates of our target and used an input spectrum of 2MASS J00361617+1821104 (Reid et al., 2000, L3.5). We set the defocus parameter in Tiny Tim to the model defocus provided on the Space Telescope Science Institute webpage[4] for each image of each target. The model defocus is computed to account for breathing, according to the telescope temperature data.

We sampled the Tiny Tim PSF at 5× the pixel scale ($0\farcs04$ pixel$^{-1}$) of WFC3/UVIS1. To simulate sub-pixel shifts of our targets we bilinearly interpolated to an arbitrary fractional pixel and then binned down to pixel scale of WFC3. We used the Nelder-Mead downhill simplex method from Press et al. (2002), which is the `AMOEBA` algorithm in IDL, to minimize the $\chi^2$, varying the $(x, y)$ position and flux normalization until finding the best fit. We computed $\chi^2$ as ((image-model)/noise)$^2$, where "noise" is the noise image provided by the WFC3 reduction pipeline. We ran the `AMOEBA` algorithm twice, starting the second run at the end point in parameter space of the first run, as recommended by Press et al. (2002). We fit a ±10 pixel cutout region centered on the target star.

[4] `http://www.stsci.edu/hst/observatory/focus`

We found average residuals after subtracting the best-fit Tiny Tim model of 5% and 6% for F814W and F850LP images, respectively. We computed residuals of our fits as the average fractional offset between the image and the model. The majority of the residual flux using the Tiny Tim model was at instrumental position angles of $30 - 50^\circ$ and $150 - 170^\circ$ in both the F814W and F850LP filters (Figure 13). If we searched for faint companions using the TinyTim PSF model and our binary fitting technique detailed below, we found that this systematic residual flux led to spurious detections of companions at these position angles.

Therefore, we instead computed a single optimal semi-empirical PSF model that minimized the residuals across all images by modifying the Tiny Tim model. We iteratively solved for a $5\times$ over-sampled additional component image to be added to the Tiny Tim model. The best guess of this additional component at each pixel was computed as the median across all normalized images of the data minus the previous iteration's PSF model. We computed a semi-empirical PSF model as the Tiny Tim model at the mean position of our targets with this additional component added in.

Using our semi-empirical PSF model, the final residuals of our fits were improved by $5\times$ to $\approx$0.9% and $\approx$2.3% for F814W and F850LP, respectively (Figure 13). Most importantly, we no longer see the concentrated residual flux at position angles of $150 - 170^\circ$. We use our semi-empirical PSF model in all subsequent analysis.

The method of fitting binaries is the same as described above, but instead of using a single model we use two co-added models. As before, the `AMOEBA` algorithm

minimizes the $\chi^2$ between the image and co-added semi-empirical PSFs. We varied six binary parameters: the primary's position on detector, the flux normalization between the primary star and the PSF model primary, the binary separation, the position angle, and flux ratio between the primary and secondary.

### 3.4.2 Quantifying False Positives

If we run our binary fitting code on a image of a single star, we recover binary parameters of false positive companions. By definition, these detections reveal the distribution in separation and flux ratio of the false positives we would find while searching for companions in our imaging data. To characterize the false positives for our WFC3 data, we fit images of our target stars using our binary fitting technique from §3.4.1. We scale all images to either the median or minimum S/N of our sample by adding in gaussian noise (Table 16). This allows us to put our sample on a common scale for our simulations. For each target star, we start with 150 random initial guesses, uniformly distributed in $(x, y)$ from $0.1 - 5$ pixels, and flux ratios from $0 - 5$ mag.

We show the resulting distribution of separations vs flux ratios of recovered false positives in Figure 14. The brightness of false positives increases with decreasing separation. At the tightest separations ($<0\farcs02$, <0.6 pixel), we find that near unity flux ratio false positives are the most common. At wider separations (>1.5 pixels, $>0\farcs06$), we find that almost all false positives are found with large flux ratios of $3 - 5$

mag. This is expected, as the binary fitting code is required to return a position and flux normalization for a secondary even if one doesn't exist. In other words, the single WFC3 PSF can be fit with a model of a high flux PSF and a very low flux PSF added in to fit any small leftover residuals.

### 3.4.3 Artificial Binary Simulations

In order to compute detection limits for our survey, we generated artificial binaries at random separations of $0.3-5$ pixels ($0\farcs018-0\farcs2$), position angles of $0-360^{\circ}$, and flux ratios of $0-5$ mag. We created these artificial binaries by shifting, scaling and co-adding randomly selected pairs of actual images together. Given that the marginally sampled WFC3 PSF (FWHM $\lesssim$2 pixels) hinders the accuracy of linear interpolation at sub-pixel shifts, we shift the secondary star relative to the primary star in integer pixel steps. We scaled the image of every primary to a common S/N by adding noise, thus degrading the image to lower S/N. We scaled the secondary to a S/N appropriate for the randomly chosen flux ratio of the artificial binary.

Given the integer pixel shifts, there are fixed separations and position angles allowed by the possible image pairings. These integer pixel shifts can result in non-integer artificial binary separations because the sub-pixel position for each image varies. Out of all possible pairings we selected a subset of 4800 artificial binaries that are distributed uniformly in log separation, flux ratio, and position angle. We ran two sets of simulations for each filter, scaling primaries alternatively to the median S/N

and the minimum S/N of our images (Table 16). Only half the images were used for the median S/N simulations, given that we only scaled images down in S/N, never up.

We then blindly fitted for the binary parameters of our artificial binaries using a double PSF model as described in §3.4.1, using 150 random initial guesses. The best-fit values for each parameter are calculated as the mean of the resulting 150 runs of our binary fitting code parameters where runs with outlier $\chi^2$ were excluded from the average.

### 3.4.4 Deriving False Positive Curves

The binary parameters recovered in our artificial binary simulations contain a mix of both detections and false positives. To assess the likelihood of a given binary fit being a detection, we compared our distribution of false positives from §3.4.2 and our fits to artificial binaries from §3.4.3 to measure our false positive curve, i.e the largest flux ratio before the recovered secondary star becomes indistinguishable from a false positive at a given separation.

We considered the artificial binaries and false positives in a given separation and flux ratio range, using 0.1 dex pixel bin widths and 0.3 mag flux ratio bin widths, respectively. In each separation bin we normalized the histogram of false positive flux ratios to the histogram of recovered artificial binary flux ratios by conservatively assuming that any artificial binaries with recovered flux ratios larger than the me-

dian false positive flux ratio $\Delta m_{crit}$ were most likely false positives themselves. We computed this normalization factor as $\frac{n}{0.5 n_{fp}}$, where $n_{fp}$ is the total number of false positives and $n$ is the number of artificial binaries with flux ratios $>\Delta m_{crit}$. After normalization, we computed the false positive fraction as a function of flux ratio as $1 - \frac{n_{fp}}{n}$. We repeat the procedure above for each separation bin. This procedure is depicted in Figure 15 for the $0.79 - 1.0$ pixel separation bin.

With the procedure detailed above, we computed false positive curves at the median and minimum S/N of our images for the F814W and F850LP filter as shown in Figure 16. Each of our false positive curves are representative of a *single*, S/N given that we scale our all our images to a common S/N for each set of simulations.

### 3.4.5 Deriving Contrast Curves

We computed contrast curves that correspond to the largest flux ratio companion that our binary PSF fitting technique can recover accurately at a given separation. A binary is considered "recovered" if the best fit parameters are within 0.2 pixels and 1 mag of the input $(x, y)$ positions and flux ratio, respectively. We binned our simulated binaries by separation and flux ratio with bin widths of 0.1 dex pixels and 0.3 mag, respectively. In each bin, we computed the completeness fraction as the number of artificial binaries that are recovered divided by the total number of artificial binaries in the bin. We define our contrast curves as the flux ratio bin at a given separation where the completeness fraction is 90% determined by the interpolation of the binned

results. We computed contrast curves at the median and minimum S/N of our targets (Table 16) for the both F814W and F850LP filters.

Figure 17 shows our resulting contrast curves. We are able to recover tight ($<0\farcs04$, $<1$ pixel) binaries with flux ratios $\lesssim$1 mag. At wider separations we recover binaries $3-5$ magnitudes fainter. We also constructed a contrast curve with a stricter recovery requirement to be within 0.3 mag of the input. This leads to a contrast curve that reaches in to binary separations of $0\farcs035$ (0.9 pixels) and is identical to our default recovery requirements outside $0\farcs055$ (1.4 pixels). A flux ratio of $\lesssim$1 mag for our targets corresponds to a mass ratio $q \gtrsim 7$ which allows us to rule out the possibility of Pleiades brown dwarf binaries similar to field brown dwarf binaries, since the latter mostly have $q \approx 1$ (see review by Burgasser et al., 2007). This means that a stricter flux ratio requirement of $<$0.3 mag for constructing our contrast curves is unnecessary. Thus, our PSF fitting technique is able to recover artificial binaries as tight as $0\farcs03$, well inside the diffraction limit ($\approx \frac{1}{3}\lambda/D$)

Given that each target in our sample has a different S/N, we interpolated over the measured median and minimum S/N curves to compute a contrast curve for each target. We conservatively fixed the contrast curve for our targets with S/N higher than the median S/N to the median S/N contrast curve. Our detection limits in F814W and F850LP mag for each target are shown in Table 17. These detection limits have lower contrast and are more conservative than the false positive curves, as expected. Finally, we convert our contrast curves from F814W and F850LP mag-

nitudes to masses using BT-Settl models Allard (2014) tied to the COND evolution models of Baraffe et al. (2003). We assumed an age of 125 Myr (Barrado y Navascués et al., 2004) and distance to the Pleiades of 136.2  pc (Melis et al., 2014). Figure 6 shows the 90% completeness contrast curve for each target as a function of mass ratio ($q$) and projected separation ($a$) in AU. We use only the F814W contrast curve for our constraint on the binary frequency due to higher S/N, larger contrast, and closer limiting separation than our F850LP contrast curve.

### 3.4.6 Completeness Maps

Similar to how we derive contrast curves in §3.4.5, we derive a median and a minimum S/N completeness map for the F814W and F850LP filters. Each completeness map represents the probability that a companion with a given separation and flux ratio would have been detected (Figure 19). The procedure for deriving completeness maps is exactly as deriving a contrast curve in §3.4.5 except that we compute the completeness fraction at every separation and flux ratio bin. We computed a completeness map for each target similar to §3.4.5, by interpolating over the median and minimum S/N completeness maps. We conservatively fixed the completeness maps for our targets with S/N higher than the median S/N to the median S/N completeness map. Our completeness maps for several targets are shown in Figure 19.

## 3.5 Results

### 3.5.1 L Dwarf Binary Frequency of the Pleiades

We found no companions in surveying 11 brown dwarf members of the Pleiades with $K \gtrsim 16.0$ mag. Our F814W contrast curves demonstrate that we could have detected companions with mass ratios of $q \gtrsim 0.5$ at separations $a \gtrsim 10$ AU and $q \gtrsim 0.8$ at $a \gtrsim 4$ AU (Figure 18). Most known very low mass binaries are sharply peaked towards mass ratios $q \approx 1$ (Burgasser et al., 2006; Liu et al., 2010). Furthermore, our detection limits probe down to separations $a \approx 4$ AU, near the peak of the observed binary distribution (Burgasser et al., 2006). Thus, our detection limits are sensitive to the majority of binaries expected from the observed field population of T dwarfs (Burgasser et al., 2003, 2006; Gelino et al., 2011; Liu et al., 2012; Radigan et al., 2013).

We estimated the binary frequency for the Pleiades by comparing our completeness maps (§3.4.6) to various random simulated populations of binaries. Each population of binaries had an adopted eccentricity, mass ratio and separation distribution, with semi-major axes of <25 AU in accordance with observations of T dwarf binaries in the field. We adopted a uniform eccentricity distribution of $0 - 0.9$ in accordance with observations (Dupuy & Liu, 2011). For our mass ratio distribution, we used the observed power law of $P(q) \propto q^{4.9}$ (Liu et al., 2010). For our separation distribution, we used the log normal distribution from Allen (2007). We assumed uniform prior distributions of longitude of ascending node, mean anomaly, and argument of

periapsis, and an $a \sin i$ distribution for inclination. We projected each binary on sky from the population with $10^5$ randomly chosen orbits. We compared each of these $10^5$ orbits to each completeness map of each target. The probability for detecting a binary was given by our completeness fraction at the separation and mass ratio of the binary from the completeness maps (Figure 19). We averaged over all probabilities and computed a single average probability ("detectability") to recover a companion for each target star (Table 19). Similar to Aberasturi et al. (2014), we then summed over these average probabilities, and found that if all our targets had companions we should have detected 7.6 binaries for the log normal distribution of semi-major axes. We also used a linear (flat) semi-major axis distribution to be consistent with Aberasturi et al. (2014), finding virtually no difference in the total number of binaries we should have detected (8.1). The lack of detections implies a binary frequency upper limit of <11% for $1\sigma$ (<26% at $2\sigma$) using the recommended Jeffrey's distribution for small $n$ (Brown et al. , 2001). Aberasturi et al. (2014) computed a binary frequency for $\gtrsim$T5 primaries in the solar neighborhood of <16%-<25% using the Clopper-Pearson interval at 95% confidence using the same log normal and uniform separation distributions. This is comparable to our own binary frequency upper limit of <26% at $2\sigma$ ($\approx$ 95% confidence).

### 3.5.2 Binary Frequency vs Age for Wide (>10 AU) Companions

According to the evolution models of Baraffe et al. (2003), our sample of Pleiades L dwarfs are expected to evolve to $T_{\rm eff} = 700 - 1300\,{\rm K}$ (i.e., T0-T8 spectral types) at ages of $0.5 - 5.0$ Gyr. At younger ages of $1 - 10\,{\rm Myr}$, our sample would have had temperatures of $2300 - 2750\,{\rm K}$ (i.e. M7 − M9). Thus, we compared our binary frequency constraint to AO and *HST* observations of $\gtrsim$M7 objects in Taurus (Todorov et al., 2014; Kraus & Hillenbrand, 2012; Kraus et al., 2006; Konopacky et al., 2007; Todorov et al., 2010), Chamaeleon I (Luhman, 2004; Lafrenière et al., 2008; Ahmic et al., 2007; Luhman, 2007; Neuhäuser et al., 2002), Upper Sco (Biller et al., 2011; Kraus & Hillenbrand, 2012) and the field (Burgasser et al., 2006). Taurus, Chamaeleon I and Upper Sco are regions with objects all at the same distance, thus aiding the comparison.

It is possible that the different cluster stellar densities in which brown dwarfs form could affect the binary frequency, hindering a direct comparison between field and young brown binary frequencies as done here. However, King et al. (2012) find that the binary frequency for stars with masses of $0.1 - 0.3\,{\rm M}_{\odot}$ did not vary measurably over nearly 20× in density for five young regions (Taurus, Chamaeleon I, Ophiucus, IC 348, and the Orion Nebula Cluster). Figure 20 and Table 18 summarizes these comparisons of the binary frequency at different ages. In contrast to our estimate of the binary frequency in §3.5.1, here we used only the methods of Burgasser et al. (2003) for computing the binary frequency of these different clusters and the field in

order to keep the statistical analysis the same.

For constraining our binary frequency of Pleiades at wider separations $a \gtrsim 10$ AU, 4 brown dwarfs observed by the *HST*/WFPC2 and *HST*/ACS surveys of Martín et al. (2003) and Bouy et al. (2006a) were combined with our own observations for a larger sample size of 15 objects. These 4 brown dwarfs match our $K \gtrsim 16.0$ mag cutoff and conservative Pleiades cluster membership criteria, i.e. that the target must have proper motion indicating cluster membership and a spectral type $\gtrsim$M9 (see §3.3.1). Brown dwarfs PLIZ 28 and PLIZ 2141 were observed with *HST*/ACS by Bouy et al. (2006a) with detection limits that ruled out companions for mass ratios $q \gtrsim 0.45$ at separations $a \gtrsim 7-12$ AU. Brown dwarfs Roque 30 and Roque 33 were observed with *HST*/WFPC2 by Martín et al. (2003) and similarly they ruled out companions for mass ratios $q \gtrsim 0.5$ and separations $a \gtrsim 10$ AU. The *HST*/ACS and *HST*/WFPC2 observations have comparable detection limits to our own detection limits of $q \gtrsim 0.6$ at separations $a \gtrsim 10$ AU. Thus, with a combined sample size of 15 low mass Pleiades brown dwarfs and no binaries detected, we computed an upper limit on the binary frequency of <7.0% ($1\sigma$) for mass ratios $q \gtrsim 0.6$ and separations $a \gtrsim 10$ AU.

The sample of young brown dwarfs observed by *HST*/WFPC2 and AO surveys (see Table 18) compiled in Todorov et al. (2014) and references therein includes all targets with spectral types $\gtrsim$M4. The detection limits for these surveys are generally sensitive to companions with separations $a \gtrsim 10$ AU. In an attempt to constrain the masses of the primaries to $\lesssim$40 $M_{Jup}$, we included only primaries in the Todorov

et al. (2014) sample with spectral types $\gtrsim$M7 (see Table 18). Note that for young (<10 Myr) brown dwarfs mass estimates at young ages are still uncertain and could have large uncertainties due the lack of a well measured $T_{\rm eff}$ scale for these stars and uncertain atmospheric and stellar evolution models. This spectral type cut off corresponds to a mass estimate of $\lesssim$40 $M_{\rm Jup}$ at ages $\approx$ 1 Myr and $\approx 2-3$ Myr for the Taurus and Chamaeleon I regions, respectively, according to the Baraffe et al. (2003) models. Over this range there are 3 out of 37 binaries in Taurus and 1 out of 22 binaries in Chamaeleon I, which corresponds to binary frequencies of $0.0-6.0\%$ and $0.0-10.0\%$ ($1\sigma$) respectively. We find our binary frequency upper limit of <7.0% is in agreement with binary frequencies for both Taurus and Chamaeleon I. One caveat is we included candidate companions in Taurus 2MASS J04414489+2301513 and 2MASS J04221332+1934392 from Todorov et al. (2014) in the binary frequency computed here. If those objects are not binaries, the binary frequency of Taurus would be even lower ($0.0-6.0\%$), still in agreement with our own binary frequency limit.

Kraus & Hillenbrand (2012) and Biller et al. (2011) observed 10 and 18 members of Upper Sco with spectral types $\gtrsim$M7 respectively and were sensitive to companions with separations $\gtrsim$10 AU. Given an age of 11 Myr for Upper Sco (Pecaut et al., 2012) and the spectral type–$T_{\rm eff}$ relation of Pecaut & Mamajek (2013), $\gtrsim$M7 spectral types correspond to $\lesssim$2650 K and thereby masses of $\lesssim$40 $M_{\rm Jup}$. This is comparable to our own mass range of $25-40$ $M_{\rm Jup}$. Both previous surveys have detection limits $q \gtrsim 0.8$

at separations $a \gtrsim 10$ AU with no binaries detected. Using this combined sample, we estimated a binary frequency of $0.0 - 4.0\%$ for Upper Sco, which is consistent to our own binary frequency upper limit of $<7.0\%$ for the Pleiades.

Burgasser et al. (2006) resolved 5 T dwarf binaries with separations of $a = 1.8-5.0$ AU out of 22 stars observed with *HST*/NICMOS. They computed a Malmquist bias-corrected binary frequency of $8 - 19\%$ for mass ratios $q \gtrsim 0.6$ and separations $a \gtrsim 2$ AU. However, to directly compare to our detection limits, we recomputed their Malmquist bias-corrected binary fraction and considered only the 2 T dwarf binaries which have projected separations of $\gtrsim$10 AU, which gives a binary frequency of $<3.0\%$ for 0 binaries detected out of 17 objects observed.

Bate (2012) performed hydrodynamic simulations of star formation that produced 27 objects with masses $<70$ $M_{Jup}$, with none ending up as binaries. Bate (2012) quoted a binary frequency of $0.0 \pm 5\%$ for the mass range of $30 - 70$ $M_{Jup}$ and a binary frequency of $<7\%$ for the mass range $10 - 30$ $M_{Jup}$. These predictions are in good agreement with our observed binary frequency constraint of $<7.0\%$ for separations $\gtrsim$10 AU.

## 3.6 Summary

The measurement of the brown dwarf binary frequency at different ages is fundamental tool for testing theory, given that the statistical properties of binaries probe formation scenarios in the very low-mass regime. In this work, we tripled the number

low-mass Pleiades brown dwarfs searched for companions, surveying a sample of 11 previously unobserved L dwarfs in the Pleiades, predecessors to T dwarfs in the field, using *HST*/WFC3. We have constrained the binary frequency in Pleiades for the lowest known mass ($25 - 40$ $M_{Jup}$) and latest known type ($\gtrsim$M9) brown dwarfs to $<$11% at $1\sigma$ ($<$26% at $2\sigma$) confidence for companions as close as $\approx 4$ AU, finding no binaries. Our survey is the first to probe down to separations of 4 AU at such young ages.

Furthermore, we find our binary frequency constraints are in good agreement with observed binary frequencies of young star forming regions Taurus ($0.0 - 6.0\%$), Chamaeleon I ($0.0 - 10.0\%$), and Upper Sco ($0.0 - 4.0\%$) for objects with similar primary masses of $<40$ $M_{Jup}$, at $1\sigma$ with projected separations $>10$ AU. Overall, our observations of the Pleiades support the evidence that T dwarf binaries are likely uncommon, and consistent with having the same frequency at both young ($1 - 10$ Myr), intermediate ($\approx$120 Myr) and old ($\gtrsim$1 Gyr) ages.

Table 14. Pleiades Sample

| Name[a] | R. A. J2000.0 | Decl. J2000.0 | Mass[b] $M_{Jup}$ | K mag | SpT | SpT Ref | P.M. Ref |
|---|---|---|---|---|---|---|---|
| BRB 17 | 03 54 07.98 | +23 54 27.9 | 43 | $16.03 \pm 0.03$ | L0 | 1 | 2 |
| NPNPL 2 | 03 46 34.26 | +23 50 03.7 | 41 | $16.09 \pm 0.03$ | | | 3 |
| PLIZ 31 | 03 51 47.65 | +24 39 59.2 | 40 | $16.09 \pm 0.03$ | | | 3,4 |
| BRB 21 | 03 54 10.27 | +23 41 40.2 | 31 | $16.39 \pm 0.04$ | L3 | 1 | 2 |
| PLIZ 35 | 03 52 39.16 | +24 46 29.5 | 31 | $16.51 \pm 0.04$ | L2 | 1 | 2 |
| BRB 23 | 03 50 39.54 | +25 02 54.7 | 30 | $16.56 \pm 0.04$ | L3.5 | 1 | 2 |
| PLIZ 161 | 03 51 29.47 | +24 00 37.3 | 28 | $16.70 \pm 0.05$ | | | 3 |
| UGCS J0348+2550[e] | 03 48 15.63 | +25 50 08.9 | 28 | $16.73 \pm 0.05$ | L3±1 | 8 | 3,7 |
| BRB 28 | 03 52 54.90 | +24 37 18.2 | 26 | $16.92 \pm 0.06$ | | | 2 |
| PLIZ 1262 | 03 44 27.27 | +25 44 42.0 | 26 | $16.95 \pm 0.07$ | | | 2,4 |
| BRB 29 | 03 54 01.43 | +23 49 57.7 | 25 | $17.00 \pm 0.07$ | L4.5 | 1 | 2 |
| Roque 33[c] | 03 48 49.03 | +24 20 25.4 | 41 | $16.06 \pm 0.03$ | M9.5 | 6 | 5 |
| Roque 30[c] | 03 50 16.09 | +24 08 34.7 | 40 | $16.08 \pm 0.03$ | | | 3 |
| PLIZ 28[d] | 03 54 14.03 | +23 17 51.4 | 35 | $16.14 \pm 0.03$ | L0.0 | 1 | 2 |
| PLIZ 2141[d] | 03 44 31.29 | +25 35 14.4 | 28 | $16.69 \pm 0.04$ | | | 2 |

Note. — [a] To search these targets by name in Simbad, add the string "Cl* Melotte 22"
[b] Masses are estimated from Baraffe et al. (2003)
[c] Observed with *HST*/WFPC2 Martín et al. (2003)
[d] Observed with *HST*/ACS Bouy et al. (2006a)
[e] UGCS J034815.64 + 255008.9

**References.** (1) Bihain et al. (2010); (2) Bihain et al. (2006); (3) Lodieu et al. (2012); (4) Casewell et al. (2007); (5) Stauffer et al. (2007); (6) Martín et al. (2000) (7) Zapatero Osorio et al. (2014a); (8) Zapatero Osorio et al. (2014b)

Table 15. *HST*/WFC3 Photometry

| Our Targets | F814W (mag) | F850LP (mag) |
|---|---|---|
| BRB 17 | $20.419 \pm 0.007$ | $19.415 \pm 0.011$ |
| NPNPL 2 | $20.685 \pm 0.006$ | $19.448 \pm 0.011$ |
| PLIZ 31 | $20.701 \pm 0.006$ | $19.524 \pm 0.013$ |
| BRB 21 | $21.344 \pm 0.010$ | $20.204 \pm 0.023$ |
| PLIZ 35 | $21.315 \pm 0.010$ | $20.096 \pm 0.021$ |
| BRB 23 | $21.604 \pm 0.012$ | $20.431 \pm 0.029$ |
| PLIZ 161 | $21.804 \pm 0.014$ | $20.678 \pm 0.034$ |
| UGCS J0348+2550 | $21.866 \pm 0.015$ | $20.706 \pm 0.035$ |
| BRB 28 | $22.177 \pm 0.019$ | $20.860 \pm 0.040$ |
| PLIZ 1262 | $22.211 \pm 0.020$ | $21.086 \pm 0.049$ |
| BRB 29 | $22.231 \pm 0.021$ | $21.042 \pm 0.048$ |

Table 16. Binary Simulations

| Simulation | Filter | S/N | Number of Artificial Binaries |
|---|---|---|---|
| Median S/N | F814W | 93.5 | 4800 |
| Min S/N | F814W | 61.1 | 4800 |
| Median S/N | F850LP | 49.1 | 4800 |
| Min S/N | F850LP | 33.0 | 4800 |

Table 17. Detection Limits

| Target | 0.″025 | 0.″032 | 0.″040 | 0.″050 | 0.″063 | 0.″080 | 0.″100 | 0.″126 | 0.″159 | 0.″180 |
|---|---|---|---|---|---|---|---|---|---|---|
| **F814W (mag)** | | | | | | | | | | |
| BRB17 | 20.66 | 21.26 | 21.88 | 22.20 | 22.48 | 22.75 | 22.77 | 23.05 | 23.69 | 23.06 |
| NPNPL2 | 20.93 | 21.52 | 22.15 | 22.46 | 22.75 | 23.02 | 23.04 | 23.31 | 23.95 | 23.33 |
| PLIZ31 | 20.94 | 21.54 | 22.17 | 22.48 | 22.76 | 23.03 | 23.05 | 23.33 | 23.97 | 23.35 |
| BRB21 | 21.59 | 22.18 | 22.81 | 23.12 | 23.41 | 23.67 | 23.70 | 23.97 | 24.61 | 23.99 |
| PLIZ35 | 21.56 | 22.15 | 22.78 | 23.09 | 23.38 | 23.65 | 23.67 | 23.94 | 24.58 | 23.96 |
| BRB23 | 21.85 | 22.44 | 23.07 | 23.38 | 23.67 | 23.93 | 23.96 | 24.23 | 24.87 | 24.25 |
| PLIZ161 | | 22.64 | 23.27 | 23.26 | 23.54 | 24.13 | 23.86 | 24.43 | 24.72 | 24.45 |
| UGCSJ0348+2550 | | 22.70 | 23.33 | 23.32 | 23.61 | 23.93 | 23.92 | 24.49 | 24.78 | 24.51 |
| BRB28 | | 22.70 | 23.30 | 23.63 | 23.92 | 24.25 | 24.23 | 24.53 | 24.76 | 24.55 |
| PLIZ1262 | | 22.73 | 23.34 | 23.66 | 23.66 | 24.28 | 24.27 | 24.57 | 24.80 | 24.58 |
| BRB29 | | 22.75 | 23.36 | 23.68 | 23.68 | 24.30 | 24.29 | 24.59 | 24.82 | 25.44 |
| **F850LP (mag)** | | | | | | | | | | |
| BRB17 | | | 20.26 | 20.55 | 20.57 | 20.90 | 21.49 | 21.14 | 21.77 | 21.76 |
| NPNPL2 | | | 20.29 | 20.59 | 20.60 | 20.93 | 21.52 | 21.17 | 21.81 | 21.80 |
| PLIZ31 | | | 20.37 | 20.66 | 20.68 | 21.01 | 21.60 | 21.25 | 21.88 | 21.87 |
| BRB21 | | | 21.05 | 21.34 | 21.36 | 21.69 | 22.28 | 21.93 | 22.56 | 22.55 |
| PLIZ35 | | | 20.94 | 21.23 | 21.25 | 21.58 | 22.17 | 21.82 | 22.46 | 22.44 |
| BRB23 | | | 21.28 | 21.57 | 21.59 | 21.91 | 22.51 | 22.16 | 22.79 | 22.78 |
| PLIZ161 | | | 20.73 | 20.92 | 21.83 | 22.16 | 22.12 | 22.40 | 22.44 | 22.16 |
| UGCS J0348+2550 | | | 20.76 | 20.95 | 21.86 | 22.19 | 22.15 | 22.43 | 22.46 | 22.19 |
| BRB28 | | | | 20.91 | 21.71 | 22.02 | 22.31 | 22.30 | 22.30 | 22.34 |
| PLIZ1262 | | | | 21.14 | 21.94 | 22.24 | 22.53 | 22.53 | 22.53 | 22.57 |
| BRB29 | | | | 21.10 | 21.90 | 21.88 | 22.49 | 22.48 | 22.48 | 22.53 |

Table 18. Binary Frequency vs. Age for Wide (>10) AU Companions

| Region | Age | Age Ref | Sample Ref | $N_{\rm obj}$ | $N_{\rm bin}$ | Bin Freq % | $q$ |
|---|---|---|---|---|---|---|---|
| Taurus | 1 Myr | 15 | 1,2,3,4,5 | 37 | 3 | $0.0-6.0$ | $\gtrsim 0.7$ |
| Chameleon I | 2-3 Myr | 16 | 4,5,6,7,8,9,10 | 22 | 1 | $0.0-10.0$ | $\gtrsim 0.7$ |
| Upper Sco | 11 Myr | 17 | 2,11 | 28 | 0 | $0.0-4.0$ | $\gtrsim 0.8$ |
| This work + lit | 125 Myr | 18 | 12,13 | 15 | 0 | <7.0 | $\gtrsim 0.6$ |
| Field | 0.5-5.0 Gyr | 19 | 14 | 17 | 0 | <3.0 | $\gtrsim 0.6$ |

Note. — Faint companions to brown dwarfs with separations and mass ratios greater than given in table are ruled out by the given detection limits for primaries with masses $<40{\rm M_{Jup}}$ and separations >10 AU.

**References.** (1) Todorov et al. (2014); (2) Kraus & Hillenbrand (2012); (3) Kraus et al. (2006)(4) Konopacky et al. (2007) (5) Todorov et al. (2010); (6) Luhman (2004); (7) Lafrenière et al. (2008); (8) Ahmic et al. (2007); (9) Luhman (2007); (10) Neuhäuser et al. (2002); (11) Biller et al. (2011); (12) Martín et al. (2003); (13) Bouy et al. (2006a); (14) Burgasser et al. (2006); (15) Luhman (2007); (16) Luhman et al. (2010); (17) Pecaut et al. (2012); (18) Barrado y Navascués et al. (2004); (19) Assumed age for field T dwarfs by Burgasser et al. (2006) from Reid & Hawley (2000).

Table 19. Companion Detectability

| Name | Detectability log normal $a$ |
|---|---|
| BRB17 | 70.8% |
| BRB21 | 68.7% |
| BRB23 | 69.9% |
| BRB28 | 67.2% |
| BRB29 | 66.7% |
| NPNPL2 | 71.4% |
| PLIZ1262 | 66.9% |
| PLIZ161 | 68.8% |
| PLIZ31 | 71.3% |
| PLIZ35 | 68.6% |
| UGCS J0348+2550 | 68.8% |
| Total Expected Binaries | 7.6 |
| Binary Frequency[a] | <11% |

Note. — [a] Binary frequency with $1\sigma$ using the Jeffrey interval recommended for low $n$ by Brown et al. (2001).

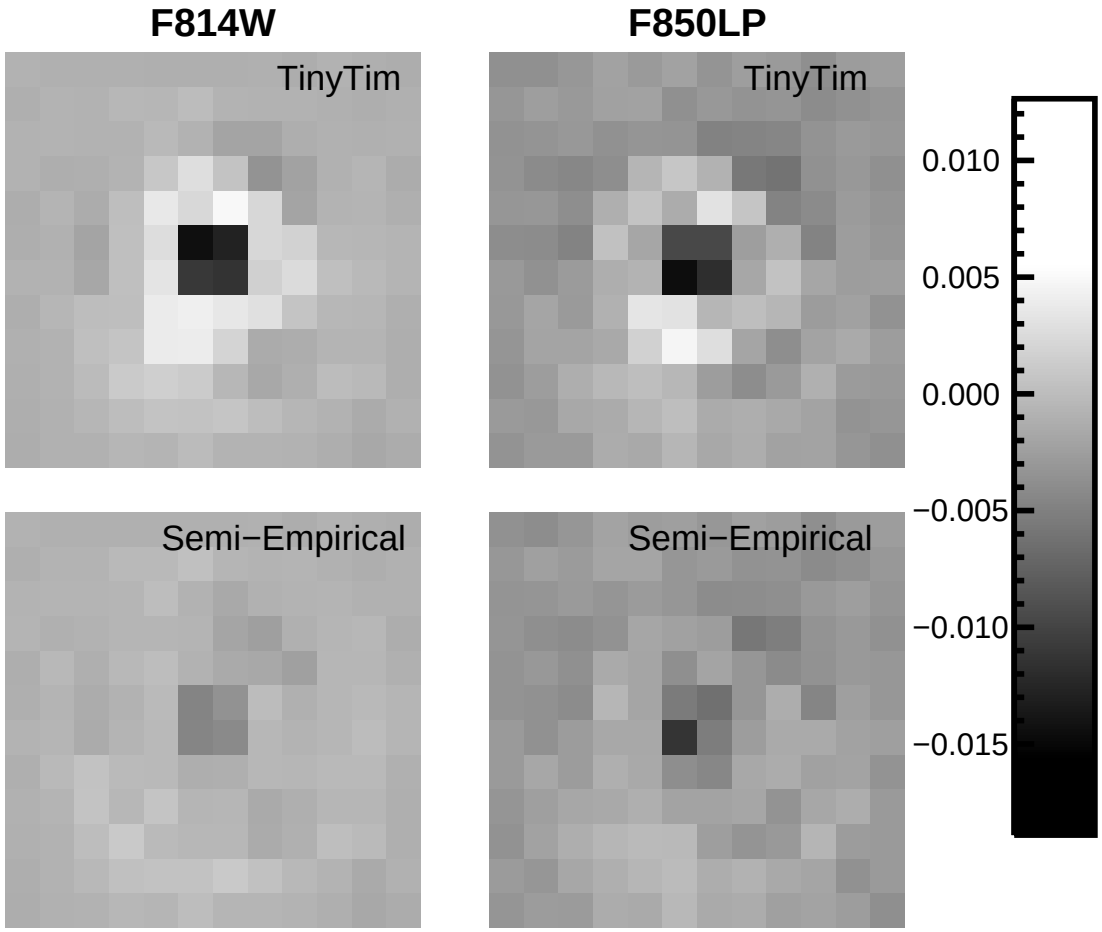


Figure 13: The average residuals of all WFC3 images after fitting the original Tiny Tim model (top) and fitting our semi-empirical PSF model (bottom). For viewing purposes, we display the average residuals as the normalized "(image-model)" in each filter. When using our original Tiny Tim model, the average residuals results in concentrated residual flux at instrumental position angles of $30-50^\circ$ and $150-170^\circ$ for both the F814W and F850LP filters. This would bias our binary fitting technique to preferentially recover companions with these position angles. Therefore we computed a semi-empirical model PSF using the original Tiny Tim model as a starting point as detailed in §3.4.1. The resulting average residuals are improved by a factor of 4-5$\times$ from $\approx 5\%$ and $\approx 6\%$ to $\approx 0.9\%$ and $\approx 2.3\%$ in F814W and F850LP respectively. The residuals are also smoother, no longer containing concentrations at position angles of $30-50^\circ$ and $150-170^\circ$.

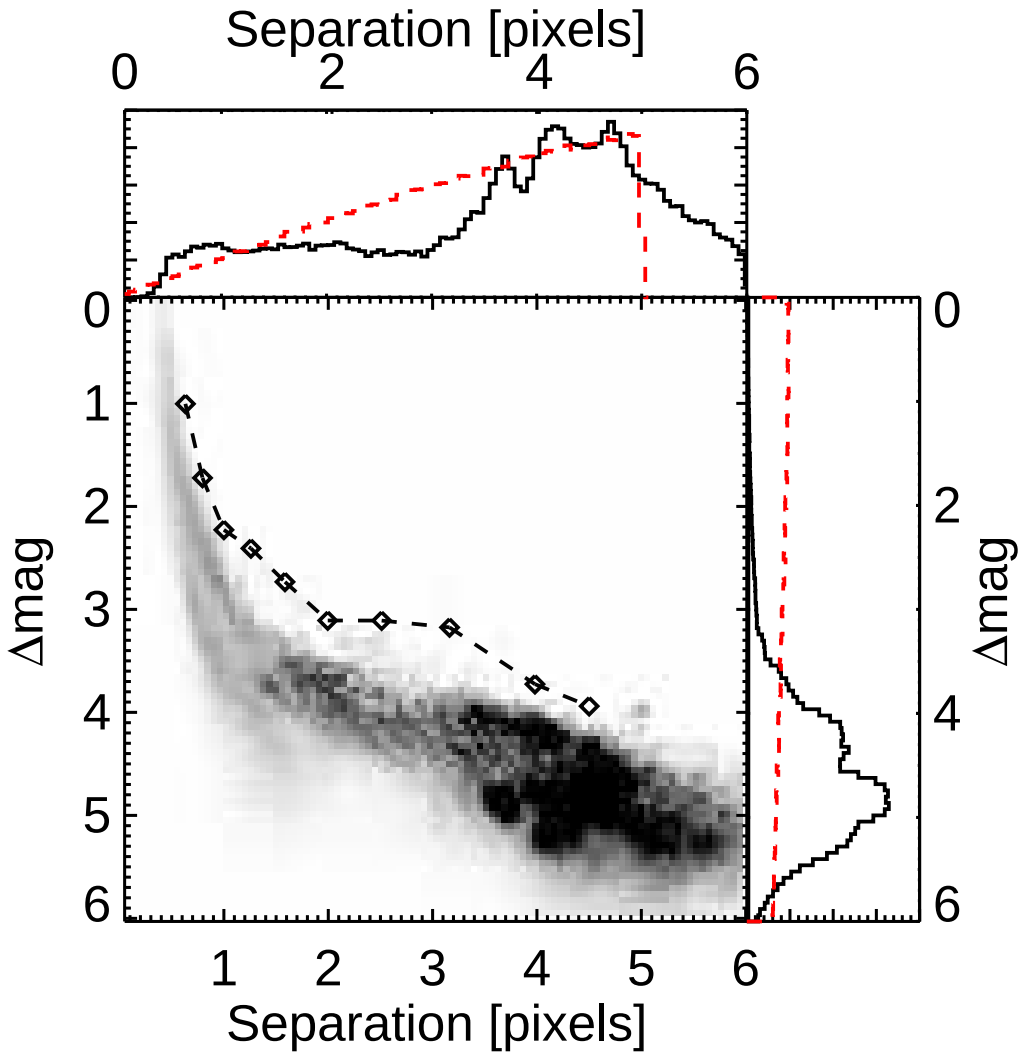


Figure 14: Number density of binary parameters returned when fitting images of single stars with a binary PSF model, i.e., false positive detections, for the median S/N F814W case. Overall, the most common false positives have wide with separations of >3 pixels, and faint flux ratios of >4 mag companions, but at separations of <1 pixels (<0.″04), the majority of false positives range with flux ratios of $0-3$ mag. The dotted red histograms are the initial guesses for the false positives uniformly distributed in log separation and flux ratio. The 1% false positive curve (§3.4.4) is over plotted (diamonds).

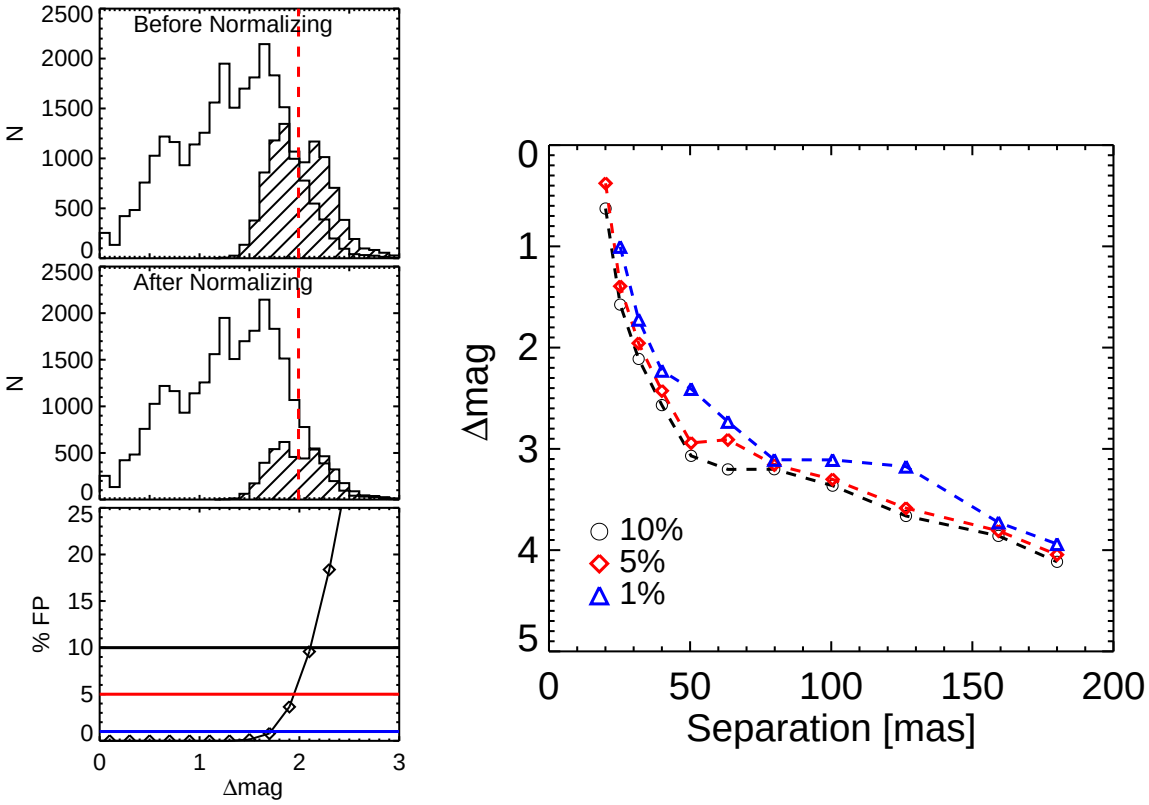


Figure 15: Illustration of our calculation of the false positive curve using the case of artificial binaries at separations $0.79 - 1.0$ pixels ($\approx 0\farcs03 - 0\farcs04$) as an example. **TOP LEFT:** The white histogram is the distribution of the recovered flux ratios $\Delta$m for artificial binaries at separations of $0.79 - 1.0$ pixels. The histogram with slashes are false positives recovered by using our binary fitting technique on single star images. The vertical red dashed line is the median false positive flux ratio. **MIDDLE LEFT:** We normalize the histogram of false positive flux ratios (slashes) to the white histogram of recovered artificial binary flux ratios by conservatively assuming that any artificial binaries with recovered flux ratios larger than the median false positive flux ratio (vertical dashed red line) are most likely false positives themselves. **BOTTOM LEFT:** 1% (black solid line), 5% (red) and 10% (blue) false positive fractions as a function of flux ratio. **RIGHT:** The false positive curve is constructed by repeating the process for all separation bins. The stars denote the $\Delta$m corresponding to 1%, 5% and 10% false positive fraction at separations of $0.79-1.0$ pixels shown at the bottom left.

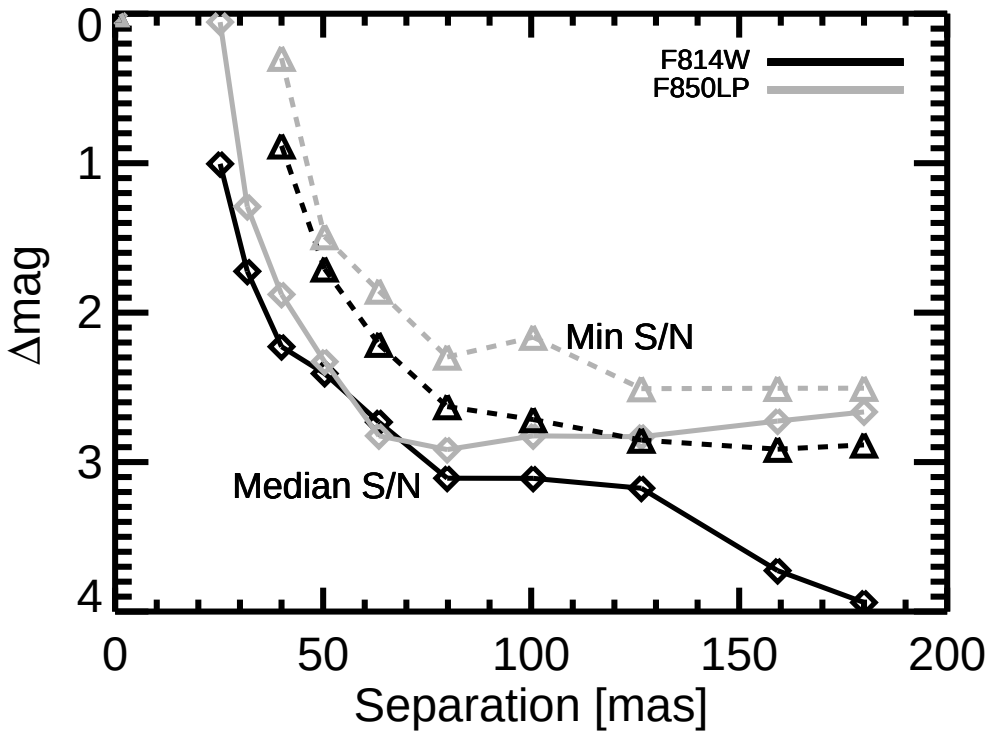


Figure 16: False positive curves computed at the minimum (triangles) and median (squares) signal-to-noise of our WFC3 images of Pleiades brown dwarfs (§3.4.4) for the F814W (black) and F850LP (grey) filters. As expected the minimum S/N false positive curves have brighter false positives than the median S/N curves in a given filter.

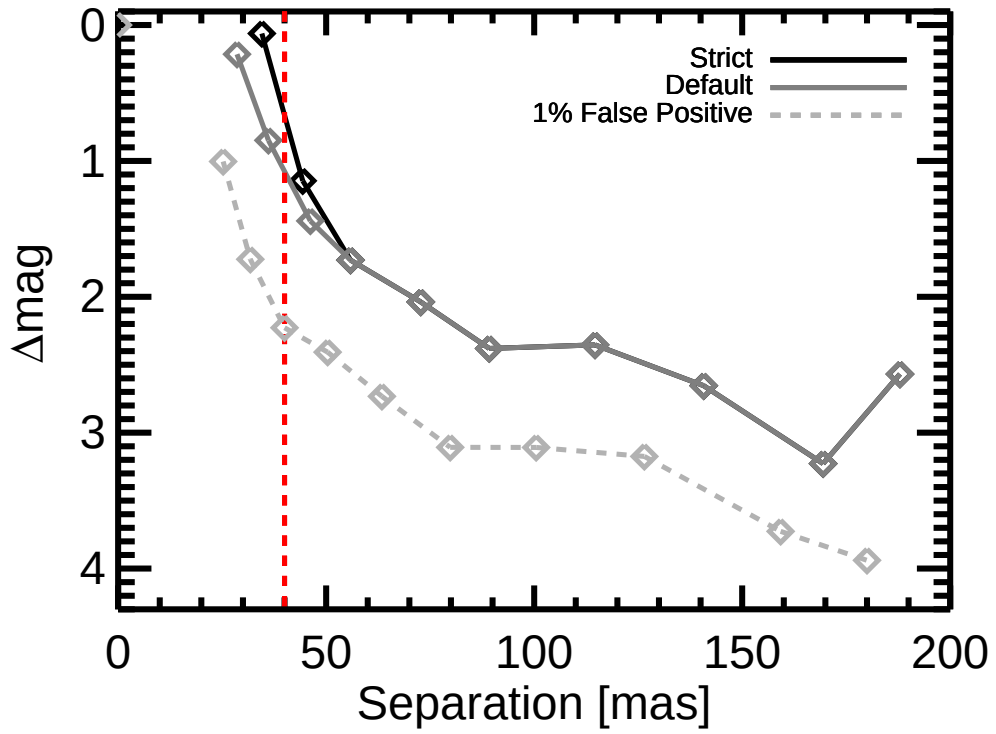


Figure 17: Contrast curves for the median F814W S/N case constructed using our default and a stricter companion recovery criteria (see §3.4.5). In our default criteria, we required companions be recovered to within 1 mag of the input binary parameters (dark grey solid line). We can recover companions with flux ratios <1 mag and separations >0.″04. We also tested a stricter criteria, and required recovered companions to be within within 0.3 mag of the input flux ratio (black solid line). The contrast curves are identical for separations >0.″055. With the stricter recovery criteria, companions with separations <0.″04 and flux ratios < 0.5 mag were detectable. Both contrast curves required that recovered artificial binaries be within 0.2 pixels of input $(x, y)$ position. We adopt our default criteria given that most brown dwarf binaries are found to have near unity flux ratios. The 1% false positive curve is shown for comparison (light grey dotted line). The contrast curve drops at 200 mas due to difficulty in fitting artificial binaries at the edge of our cut-out region of ±10 pixels.

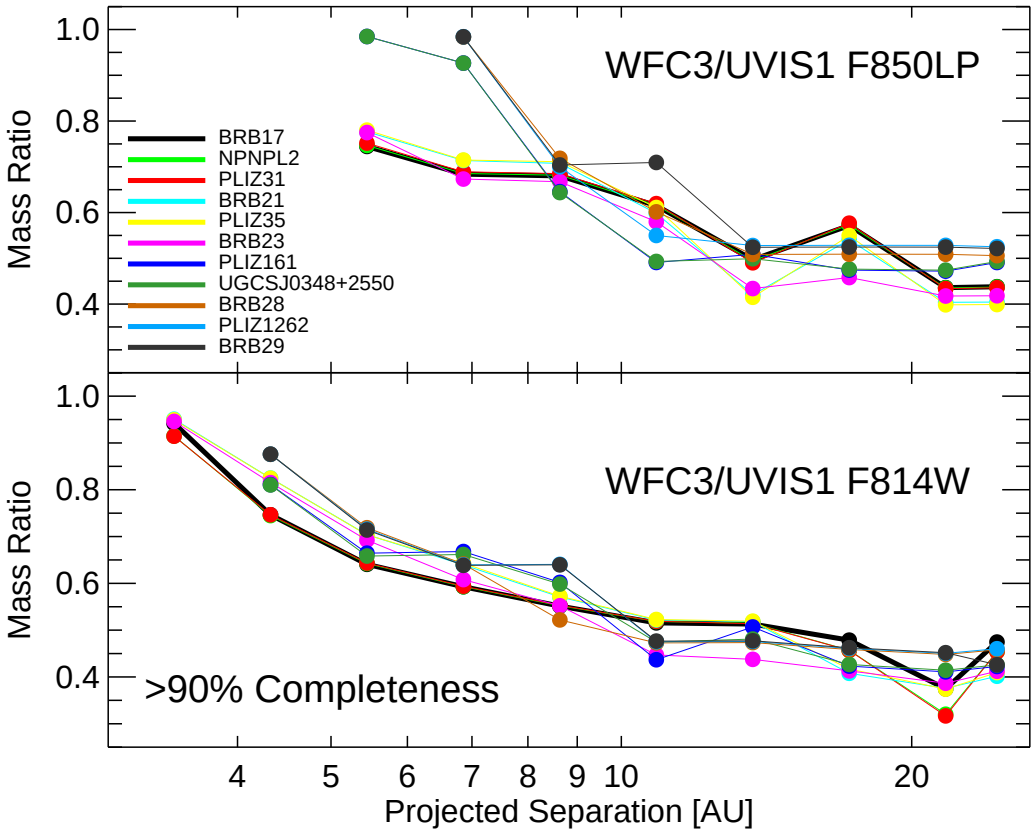


Figure 18: 90% completeness contrast curves for our F814W and F850LP observations of 11 young L dwarfs ($\lesssim$40 $M_{Jup}$) in the Pleiades. Our contrast curves rule out the majority of expected brown dwarf binaries, given that most binaries in the field have mass ratios $\gtrsim$0.6 and separations <25 AU (Burgasser et al., 2007). We convert our detection limit flux ratios in WFC3 bandpasses to mass ratios using the distance to the Pleiades (136.2 pc, Melis et al., 2014) and evolution models from Baraffe et al. (2003) tied to BT-Settl models (Allard, 2014).

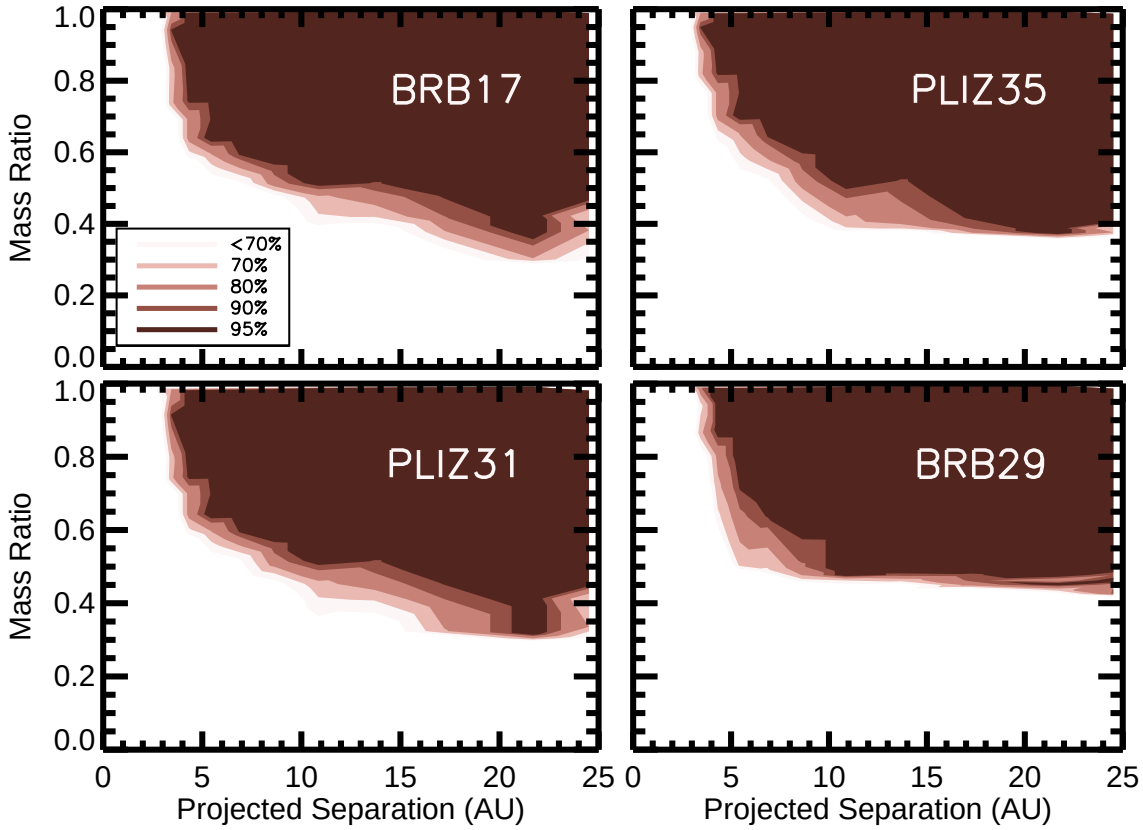


Figure 19: Example completeness maps for several our 11 young L dwarfs ($\lesssim$40 $M_{Jup}$) in the Pleiades. At each point, the completeness map represents the percentage of binaries that would have been recovered given our observations. We convert our detection limit flux ratios in WFC3 bandpasses to mass ratios using the distance to the Pleiades (136.2 pc, Melis et al., 2014), and evolution models from Baraffe et al. (2003) tied to BT-Settl models (Allard, 2014).

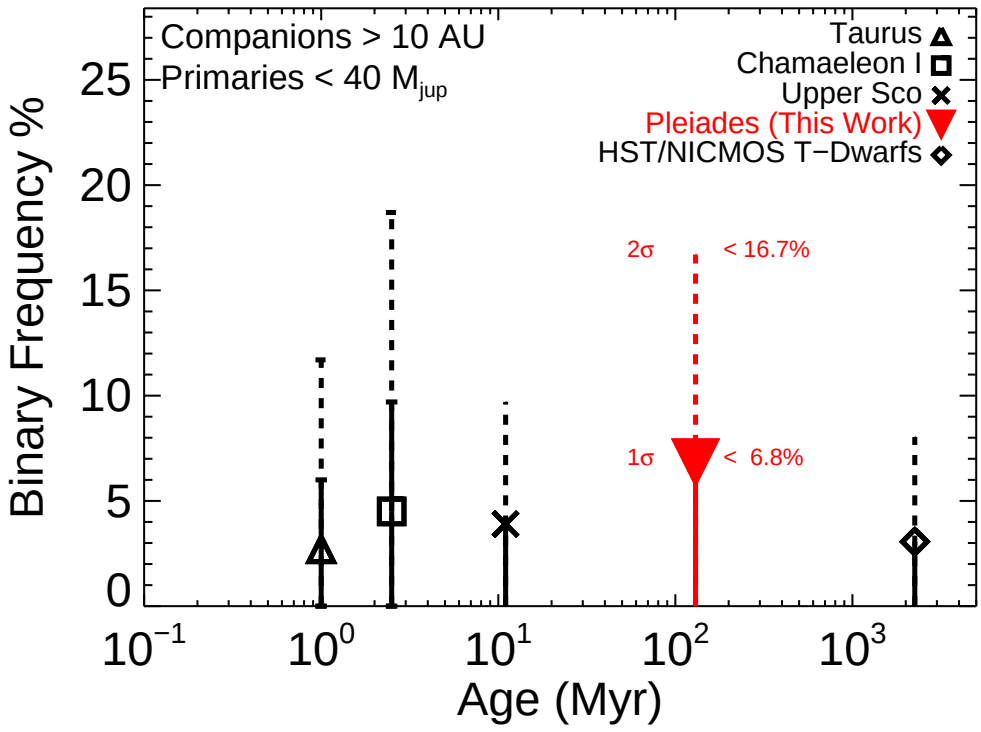


Figure 20: The wide (>10 AU) brown dwarf binary frequency as function of the age for young star forming regions, the intermediate age Pleiades, and the field (see §3.5.2). All populations are shown for a common mass range ($25 - 40$ $M_{Jup}$). Low mass brown dwarf binaries may very well be infrequent across a wide range of ages.

# REFERENCES


Aberasturi, M., Burgasser, A. J., Mora, A., et al. 2014, AJ, 148, 129

Ahmic, M., Jayawardhana, R., Brandeker, A., et al. 2007, ApJ, 671, 2074

Allen, P. R. 2007, ApJ, 668,492

Allers, K. N., Kessler-Silacci, J. E., Cieza, L. A., & Jaffe, D. T. 2006, ApJ, 644, 364

Allard, F. 2014, IAU Symposium, 299, 271

Barrado & Navascués, D., Stauffer, J. R., & Jayawardhana, R. 2004, ApJ, 614, 386

Baraffe, I., Chabrier, G., Allard, F., & Hauschildt, P. H. 1997, A&A, 327, 1054

Baraffe, I., Chabrier, G., Allard, F., & Hauschildt, P. H. 1998, A&A, 337, 403

Baraffe, I., Chabrier, G., Barman, T. S., Allard, F., & Hauschildt, P. H. 2003, A&A, 402, 701

Bate, M. R. 2009, MNRAS, 392, 590

Bate, M. R. 2012, MNRAS, 419, 3115

Bihain, G., Rebolo, R., Béjar, V. J. S., et al. 2006, A&A, 458, 805

Bihain, G., Rebolo, R., Zapatero Osorio, M. R., Béjar, V. J. S., & Caballero, J. A. 2010, A&A, 519, A93

Biller, B., Allers, K., Liu, M., Close, L. M., & Dupuy, T. 2011, ApJ, 730, 39

Bouy, H., Brandner, W., Martín, E. L., et al. 2003, AJ, 126, 1526

Bouy, H., Moraux, E., Bouvier, J., et al. 2006, ApJ, 637, 1056

Bouy, H., Martín, E. L., Brandner, W., et al. 2006, A&A, 451, 177

Brown, LD, Cat, TT and DasGupta, A (2001). Interval Estimation for a Binomial proportion. Statistical Science 16:101-133

Burgasser, A. J., Kirkpatrick, J. D., Reid, I. N., et al. 2003, ApJ, 586, 512

Burgasser, A. J., Kirkpatrick, J. D., Cruz, K. L., et al. 2006, ApJS, 166, 585

Burgasser, A. J., Reid, I. N., Siegler, N., et al. 2007, Protostars and Planets V, 427

Burningham, B., Pinfield, D. J., Lucas, P. W., et al. 2010, MNRAS, 406, 1885

Burningham, B., Cardoso, C. V., Smith, L., et al. 2013, MNRAS, 433, 457

Casewell, S. L., Dobbie, P. D., Hodgkin, S. T., et al. 2007, MNRAS, 378, 1131

Chiu, K., Fan, X., Leggett, S. K., et al. 2006, AJ, 131, 2722

Cushing, M. C., Kirkpatrick, J. D., Gelino, C. R., et al. 2011, ApJ, 743, 50

Close, L. M., Zuckerman, B., Song, I., et al. 2007, ApJ, 660, 1492

Delfosse, X., Tinney, C. G., Forveille, T., et al. 1997, A&A, 327, L25

Dobbie, P. D., Kenyon, F., Jameson, R. F., et al. 2002, MNRAS, 335, 687

Duchêne, G., Bouvier, J., Moraux, E., et al. 2013, A&A, 555, A137

Dupuy, T. J., & Liu, M. C. 2011, ApJ, 733, 122

Epchtein, N., de Batz, B., Capoani, L., et al. 1997, The Messenger, 87, 27

Gelino, C. R., Kirkpatrick, J. D., Cushing, M. C., et al. 2011, AJ, 142, 57

Jameson, R. F., Dobbie, P. D., Hodgkin, S. T., & Pinfield, D. J. 2002, MNRAS, 335, 853

King, R. R., Parker, R. J., Patience, J., & Goodwin, S. P. 2012, MNRAS, 421, 2025

Konopacky, Q. M., Ghez, A. M., Rice, E. L., & Duchêne, G. 2007, ApJ, 663, 394

Kraus, A. L., White, R. J., & Hillenbrand, L. A. 2005, ApJ, 633, 452

Kraus, A. L., White, R. J., & Hillenbrand, L. A. 2006, ApJ, 649, 306

Kraus, A. L., & Hillenbrand, L. A. 2007, AJ, 134, 2340

Kraus, A. L., & Hillenbrand, L. A. 2012, ApJ, 757, 141

Krist, J. E., Hook, R. N., & Stoehr, F. 2011, Proc. SPIE, 8127

Lafrenière, D., Jayawardhana, R., Brandeker, A., Ahmic, M., & van Kerkwijk, M. H. 2008, ApJ, 683, 844

Luhman, K. L. 2004, ApJ, 602, 816

Luhman, K. L. 2007, ApJS, 173, 104

Luhman, K. L., Mamajek, E. E., Allen, P. R., Muench, A. A., & Finkbeiner, D. P. 2009, ApJ, 691, 1265

Luhman, K. L., Allen, P. R., Espaillat, C., Hartmann, L., & Calvet, N. 2010, ApJS, 186, 111

Luhman, K. L. 2012, ARA&A, 50, 65

Lodieu, N., Deacon, N. R., & Hambly, N. C. 2012, MNRAS, 422, 1495

Liu, M. C., Leggett, S. K., Golimowski, D. A., et al. 2006, ApJ, 647, 1393

Liu, M. C., Dupuy, T. J., & Leggett, S. K. 2010, ApJ, 722, 311

Liu, M. C., Deacon, N. R., Magnier, E. A., et al. 2011, ApJ, 740, LL32

Liu, M. C., Dupuy, T. J., Bowler, B. P., Leggett, S. K., & Best, W. M. J. 2012, ApJ, 758, 57

Melis, C., Reid, M. J., Mioduszewski, A. J., Stauffer, J. R., & Bower, G. C. 2014, arXiv:1408.6544

Martín, E. L., Basri, G., Zapatero-Osorio, M. R., Rebolo, R., & López, R. J. G. 1998, ApJ, 507, L41

Martín, E. L., Brandner, W., Bouvier, J., et al. 2000, ApJ, 543, 299

Martín, E. L., Barrado y Navascués, D., Baraffe, I., Bouy, H., & Dahm, S. 2003, ApJ, 594, 525

Moraux, E., Bouvier, J., Stauffer, J. R., & Cuillandre, J.-C. 2003, A&A, 400, 891

Nagashima, C., Dobbie, P. D., Nagayama, T., et al. 2003, MNRAS, 343, 1263

Neuhäuser, R., Brandner, W., Alves, J., Joergens, V., & Comerón, F. 2002, A&A, 384, 999

Pecaut, M. J., Mamajek, E. E., & Bubar, E. J. 2012, ApJ, 746, 154

Pecaut, M. J., & Mamajek, E. E. 2013, ApJS, 208, 9

Press, W. H., Teukolsky, S. A., Vetterling, W. T. and Flannery, B. P., 1988, Numerical Recipes in C, Second Edition, Cambridge University Press, NY

Reid, I. N., Kirkpatrick, J. D., Gizis, J. E., et al. 2000, AJ, 119, 369

Reid, I. N., Cruz, K. L., Kirkpatrick, J. D., et al. 2008, AJ, 136, 1290

Reid, I. N., & Hawley, S. L. 2000, New light on dark stars. Red dwarfs, low-mass stars, brown dwarfs., by Reid, I. N.; Hawley, S. L.. Springer, London (UK), 2000, ISBN 1-85233-100-3, Published in association with Praxis Publishing, Chichester (UK).

Radigan, J., Jayawardhana, R., Lafrenière, D., et al. 2013, ApJ, 778, 36

Stauffer, J. R., Schultz, G., & Kirkpatrick, J. D. 1998, ApJ, 499, L199

Stauffer, J. R., Hartmann, L. W., Fazio, G. G., et al. 2007, ApJS, 172, 663

Todorov, K., Luhman, K. L., & McLeod, K. K. 2010, ApJ, 714, L84

Todorov, K. O., Luhman, K. L., Konopacky, Q. M., et al. 2014, ApJ, 788, 40

van Dokkum, P. G. 2001, PASP, 113, 1420

Zapatero Osorio, M. R., Gálvez Ortiz, M. C., Bihain, G., et al. 2014, A&A, 568, AA77

Zapatero Osorio, M. R., Béjar, V. J. S., Martín, E. L., et al. 2014, arXiv:1410.2383

# CHAPTER IV

## Testing 2D and 3D Stellar Atmosphere Models with Optical Interferometry

**This chapter appears as: Garcia et al. (2016), VISION: A Six-Telescope Fiber-Fed Visible Light Beam Combiner for the Navy Precision Optical Interferometer, Publications of the Astronomical Society of the Pacific**

### 4.1 Summary

Visible-light long baseline interferometry holds the promise of advancing a number of important applications in fundamental astronomy, including the direct measurement of the angular diameters and oblateness of stars, and the direct measurement of the orbits of binary and multiple star systems. To advance, the field of visible-light interferometry requires development of instruments capable of combining light from 15 baselines (6 telescopes) simultaneously. The Visible Imaging System for Interferometric Observations at NPOI (VISION) is a new visible light beam combiner for the Navy Precision Optical Interferometer (NPOI) that uses single-mode fibers to coherently combine light from up to six telescopes simultaneously with an image-plane combination scheme. It features a photometric camera for calibrations and spatial filtering from single-mode fibers with two Andor Ixon electron multiplying CCDs. This paper presents the VISION system, results of laboratory tests, and results of com-

missioning on-sky observations. A new set of corrections have been determined for the power spectrum and bispectrum by taking into account non-Gaussian statistics and read noise present in electron-multipying CCDs to enable measurement of visibilities and closure phases in the VISION post-processing pipeline. The post-processing pipeline has been verified via new on-sky observations of the O-type supergiant binary $\zeta$ Orionis A, obtaining a flux ratio of $2.18 \pm 0.13$ with a position angle of $223.9 \pm 1.0°$ and separation $40.6 \pm 1.8$ mas over 570-750 nm, in good agreement with expectations from the previously published orbit.

## 4.2 Introduction

A beam combiner coherently combines the starlight from the multiple telescopes of the interferometer to form interference patterns (fringes). These fringes are the Fourier components of the image of the object being observed and thus allow for the measurement of the angular diameters of stars, the orbits of binary and multi-star systems with milliarcsecond separations, and the direct observation of stellar surface features. The advantage of optical interferometry is high angular resolution typically in the milliarcsecond or sub-milliarcsecond range.

Over the past two decades, visible-light beam combiners have been commissioned for three interferometers: the Navy Precision Optical Interferometer (NPOI, Armstrong et al., 1998), the Center for High Angular Resolution Astronomy (CHARA) Array (ten Brummelaar et al., 2005), and the Sydney University Stellar Interferom-

eter (SUSI, Davis et al., 1999a,b). Currently, visible-light beam combiners being commissioned or recently made operational are the Precision Astronomical Visible Observations (PAVO) for the CHARA Array and SUSI (Ireland et al., 2008; Maestro et al., 2012, 2013), the Micro-arcsecond University of Sydney Companion Astrometry instrument (MUSCA) for SUSI (Kok et al., 2012), and the Visible spEctroGraph and polArimeter (VEGA, Mourard et al., 2008, 2009, 2011, 2012) for CHARA. In addition, at NPOI there is the "Classic" pupil-plane combiner (Mozurkewich, 1994), which is having its fringe engine upgraded (Sun et al., 2014; Landavazo et al., 2014), and is named the New Classic fringe engine. All of these beam combiners have provided insights into rapidly rotating stars (Ohishi et al., 2004; Peterson et al., 2006; Jamialahmadi et al., 2015), direct measurements of stellar radii (Armstrong et al., 2001; Wittkowski et al., 2006; North et al., 2007, 2009; Bazot et al., 2011; Armstrong et al., 2012; Baines et al., 2013, 2014; Challouf et al., 2014; Jorgensen et al., 2014), validation of transiting exoplanets (Huber et al., 2012b,a), and binary and multiple star systems (Hummel et al., 1998, 2001, 2003; Patience et al., 2008; Schmitt et al., 2009; Zavala et al., 2010; Tango et al., 2009; Hummel et al., 2013; Wang et al., 2015).

However, with the exception of the upgraded "Classic" fringe engine for the NPOI, none of these are yet capable of simultaneous measurement of fringes on all available baselines. Dense coverage of the UV plane is critical for making the first direct stellar surface images at visible wavelengths, and this is best accomplished by simultaneously observing a star with as many baselines as possible. This is one of main advantages

of the Visible Imaging System for Interferometric Observations at NPOI (VISION), which has recently been commissioned and is described in this paper.

VISION's design was derived from the six-telescope Michigan InfraRed Combiner (MIRC, Monnier et al., 2004, 2006, 2007). VISION is a six-telescope, all-in-one beam combiner using single-mode fibers and visible light electron-multiplying charge coupled devices (EMCCDs). Prior to VISION and MIRC, the IONIC (Integrated Optics Near-infrared Interferometric Camera) instrument for the Infrared Optical Telescope Array (IOTA) (Rousselet-Perraut et al., 1999, 2000; Berger et al., 2003; Traub et al., 2004) to filter and guide light also used single mode fibers to measure closure phases (Ragland et al., 2004).

VISION was built by Tennessee State University in collaboration with Lowell Observatory, the United States Naval Observatory, and the Naval Research Laboratory (Ghasempour et al., 2012). It monitors individual telescope throughputs and fiber coupling efficiencies in real time for visibility calibration. VISION operates from $580 - 850$ nm, whereas MIRC operates in the near infrared (IR) at $1490 - 1750$ nm ($H$-band). It is capable of simultaneously measuring 15 visibilities, 20 triple amplitudes, and 20 closure phases, allowing for dense UV plane coverage and image reconstruction.

VISION's six-telescope simultaneous beam combination allows for multi-pixel images across the surface of a target star via image reconstruction. VISION is intended to deliver complementary visible-light observations to MIRC's near-IR observations

of rapidly rotating stars, binary stars, and red super giants (Monnier et al., 2007; Zhao et al., 2008; Che et al., 2011; Monnier et al., 2012; White et al., 2013; Baron et al., 2014; Kloppenborg et al., 2015; Roettenbacher et al., 2015a,b). Early science targets for VISION include imaging the surfaces of rapidly rotating stars and red supergiants for testing of 2D and 3D stellar models. It will be used to test 2D models of rapidly rotating stars (Espinosa Lara & Rieutord, 2011, 2013) and 3D radiative-hydrodynamic models of red supergiants (Freytag et al., 2002; Freytag Höfner, 2008; Chiavassa et al., 2009, 2010, 2011, 2012); to date, only a few rapidly rotating stars and several red supergiants have been observed via interferometry (see reviews by van Belle, 2012; Domiciano de Souza et al., 2003; Peterson et al., 2006; Monnier et al., 2007; Zhao et al., 2008; Che et al., 2011; Monnier et al., 2012; Domiciano de Souza et al., 2012; Haubois et al., 2009; Baron et al., 2014).

Furthermore, VISION has high spatial resolution imaging coupled with a large field of view from moderate spectral resolution. This allows VISION to study hierarchical triple star systems, where one of the two components of a relatively wide pair of stars is itself a much more narrowly separated binary. VISION can measure the relative astrometry between the different components of the triple or quadruple system. There are only a handful of fully characterized orbits of multi-star systems (Hummel et al., 2003; Muterspaugh et al., 2005, 2006a,b,c, 2008, 2010).

This paper presents the design of the VISION instrument, laboratory tests evaluating the system performance, and validation of the data-processing pipeline from

new on-sky resolved measurements of the O-type supergiant binary $\zeta$ Orionis A. In §4.3, the VISION optical design and light path is detailed. In §4.4 the data acquisition sequence is described. In §4.5 the throughput, cameras, system visibility, and fringe crosstalk are evaluated. In §4.6 the adaptation of the MIRC data-processing pipeline for VISION is described and the theoretical bispectrum and power spectrum bias subtraction equations for an EMCCD in the photon counting regime are evaluated. The post-processing pipeline is validated in §4.7 using on-sky commissioning observations of $\zeta$ Orionis A and new resolved astrometric measurements of the flux ratio, separation, and position angle of this benchmark binary star system are reported. Finally, in §4.8 a summary and a brief description of planned future work are discussed.

## 4.3 The VISION Instrument

### 4.3.1 Optical design

The VISION optical design is shown in Figure 21, and the beam combiner itself in Figure 22. Similar to MIRC, VISION uses single-mode optical fibers that spatially filter incoming starlight, enabling precise visibility and closure phase measurements (Shaklan et al., 1992). Unlike MIRC, the VISION fibers are polarization-maintaining. The six outputs of VISION's single mode fibers are arranged in a non-redundant pattern using a V-groove array. The polarization of the starlight parallel to the optical bench is reflected by a polarizing beam splitter, focused into multimode fibers,

which are reconfigured into linear arrangement with equal spacing, and imaged onto a EMCCD to monitor the fluxes of each beam in real-time (the "photometric camera" hereafter). The polarization of the light perpendicular to the optical bench is imaged onto an identical EMCCD to form 15 unique sets of fringes (the "fringing camera" hereafter). The EMCCDs feature sub-electron, but non-negligible, effective read noise. Light is spectrally dispersed using identical optical ($570 - 850$ nm) slit spectrographs attached to photometric and fringing cameras. Each spectrograph has a low resolution ($R \approx 200$) and medium resolution ($R \approx 1000$) option. Below is a sequential description of each optical system, in order from the siderostats where light is collected to the EMCCD detectors:

- **Light Gathering:** NPOI uses a 12.5 cm circular beam of starlight gathered by 50 cm siderostats. The light is guided to the central beam combining facility in vacuum pipes that include 125:35 beam reducers. After beam reduction, the light is passed to delay line carts with mirrors that receive feedback from the VISION fringe tracker to match optical path lengths. The result is six coherently phased, collimated circular beams of light with 35-mm diameters.

- **Routing Light to the VISION Optical Bench:** The routing of the six 35-mm collimated beams from NPOI delay lines to the optical bench is shown in Figure 23. The 35-mm beams are reflected by six UV fused silica broadband plate $^{70}/_{20}$ beam splitters placed at a 45° angle to each beam (top panel, Figure 23). Some light is lost in transmission and scattering through our custom

made broadband beam splitters which results in the $\approx 70$ reflectivity and $\approx 20$ transmissivity across $570 - 850$ nm. The $^{70}/_{20}$ beam splitter reflects 70% of the light to VISION and transmits ≈20% of the light to NPOI's tip/tilt quad cells. The six beams are then reflected to the optical bench via 3-inch flat Newport Zerodur Broadband Metallic Mirrors with silver coating[1]. The 3-inch flat mirrors are placed 45° to the beam (bottom panel, Figure 23). At the front of the VISION optical bench are shutters that can be controlled either manually or by computer. These can block light for individual beams (panel 1, Figure 22). The six beams are then reflected off 2-inch flat mirrors to the VISION off-axis parabolas.

- **Coupling Light to Single-Mode Fibers:** Each 35-mm beam is coupled to a single-mode polarization-maintaining fiber using 2-inch Nu-tek 480-900 nm silver coated off-axis parabolas (OAPs). The 165 mm focal lengths of the OAPs (f/4.7 optics) were calculated by Ghasempour et al. (2012) for typical $r_0 = 9$ cm site seeing using the method of Shaklan & Roddier (1988) (panel 2, Figure 22). The OAPs collapse the beams from 35-mm to 4-8 $\mu$m over 165 mm. Newport closed-loop picomotors and drivers are used to move the fibers vertically and horizontally relative to the VISION optical bench to maximize the coupling efficiency of the starlight into each fiber. This alignment is both manually and computer controllable. Except for the X-axis of the beam 5

[1]http://www.newport.com/Broadband-Metallic-Mirrors/141088/1033/info.aspx#tab_Specifications

driver and all of the beam 6 drivers, the picomotor drivers operate in closed-loop mode, which corrects for fiber positioning hysteresis. The fibers can be positioned to better than 2 $\mu$m, and the X and Y axis of the fibers can be aligned using an automated fiber alignment algorithm written in C++ and Python. The Newport picomotors and drivers occasionally fail with error status on startup; the picomotor drivers often require restarting a few times until they operate normally. This is an issue that will eventually be addressed but does not significantly affect performance.

- **Single-Mode Polarization-Maintaining Fibers:** In order to increase fringe contrast, VISION uses single-mode fibers that filter the atmospheric turbulence, removing residual wavefront errors for each beam. VISION uses Nufern PM630-HP single-mode polarization maintaining fibers that are operational over 570-900 nm. The fibers are multimode at wavelengths $\lesssim$ 570 nm. The single-mode fibers spatially filter wavefront errors by transmitting only the fundamental transverse mode of incoming light ($LP_{01}$). This filtering enhances fringe contrast by partially removing spatial but not temporal atmospheric turbulence. The polarization of starlight through the fibers is maintained via strong birefringence due to stress rods along the slow axis of the fiber. The mode field diameter of the fibers is 4.5 $\mu$m at 630 nm, with a core size of 3.5 $\mu$m and numerical aperture of 0.12. The beam exiting each single mode fiber can be described by a Gaussian model.

- **Non-redundant Spacing with V-groove Array:** VISION produces a unique fringe frequency for each telescope pair by arranging the outputs of the fibers in a non-redundant linear pattern on a silicon OZ-optics V-groove array (Table 20). The V-groove array has a base spacing of 250 $\mu$m. Non redundant fiber positions of 0-2-8-13-17-20 were chosen. After passing the light through a lens with long focal length, interference fringes are imaged. The fringe frequency, or number of pixels per fringe is:

$$\frac{\text{Pixels}}{\text{Fringe}} = \frac{f\lambda}{p(d_A - d_B)} \tag{13}$$

where $\lambda$ is the wavelength of the fringe, $d_A$ and $d_B$ are the location of fiber $A$ and $B$ on the V-groove array, $f$ is the focal length ($f = 750$ mm), and $p = 24$ $\mu$m is the size of the pixels of the camera on which the fringes are formed. Given that each fiber pair $AB$ has a unique physical separation $d_A - d_B$ on the V-groove array, the corresponding telescope pair have a unique fringe frequency on the VISION cameras and therefore each of VISION's 15 telescope pairs has a unique signature in a power spectrum of the image (Figure 24). The VISION geometry minimizes the overlap between the peaks in power spectra for each telescope pair (the "fringe cross talk"). The fast axis of all fibers on output of the V-groove array are aligned vertically. A lenslet array glued to the polarizing beam splitter re-collimates the beams to 250 $\mu$m diameter after they exit the fibers.

- **Output to Photometric and Fringing Cameras:** VISION splits the light between a camera to record interferograms (the "fringing" camera), and a camera to record individual beam fluxes (the "photometric" camera), using a polarizing beam splitter. The polarization of the six beams parallel to the optical bench is reflected through the beam splitter at 90° and is coupled to six multimode fibers positioned on a second V-groove array (blue arrow, panel 3, Figure 22). It is then guided to the spectrograph attached the photometric camera (blue arrow, Figure 22, panel 4). Each beam output has a unique spatial location on the photometric camera due to a V-groove array that positions the multi-mode output for each fiber onto the photometric camera. The photometric camera monitors the real-time wavelength-dependent flux of each beam.

  The polarization of the light perpendicular to the optical bench is transmitted directly through the polarizing beam splitter (red arrow, panel 3, Figure 22), and is focused by a 750 mm focal length Thorlabs antireflection coated achromatic cemented doublet to a $\sim$ 3.5 mm diameter spot size. Next, to condense the image in the non-fringing direction, VISION uses a 50 mm focal length cylindrical lens to collapse the light in the horizontal direction (red arrow, panel 4, Figure 22) to 24 $\mu$m, the size of a single pixel on the EMCCDs. This results in an image 24 $\mu$m by 3.5 mm, with fringing in the long direction that is passed to a spectrograph attached to the fringing camera, which in turn results in 128 unique spectral channels of fringes with a height of 3.5 mm in the fringing direc-

tion. The combination of the microlens array, polarizing beam splitter, and 750 mm achromatic cemented doublet achieve the desired overlap of the six Gaussian beam profiles from the six single-mode fibers along the fringing direction on the VISION camera, which produces the fringes (see the fringe forming lens to cylindrical lens ray tracing in Figure 21). The fringes are produced at the entrance to the slit of the spectrograph.

- **Spectrographs:** VISION spectrally disperses the incoming light using two identical Princeton Instruments SP-2156 Acton spectrographs, attached to the fringing and photometric cameras. The spectrographs are 1:1, i.e. there is no magnification of the Gaussian beam profiles at the entrance to the slit. VISION has two observing modes, one low resolution ($R = 200$) and one medium resolution ($R = 1000$). Switching between the $R = 200$ and $R = 1000$ grating for each spectrometer is remotely controllable and can be accomplished in a few seconds. The wavelength solution for the spectrographs was initialy derived using a Ne-Ar lamp source. This wavelength solution was verified with the pixel locations of the H$\alpha$ feature from on-sky observations of Vega, and an in-lab HeNe laser source on the fringing and photometric cameras. The resulting wavelength solution for the $R = 200$ mode is:

$$\lambda(\mathrm{i}) = (\lambda_{\mathrm{cent}} - 232.294) + 2.91(\mathrm{i}+1) - 1.30 \text{ nm, fringing camera}$$

$$\lambda(\mathrm{i}) = (\lambda_{\mathrm{cent}} - 214.986) + 2.91(\mathrm{i}+1) + 4.66 \text{ nm, photometric camera}$$

where $i = 0-127$ is the pixel number, $\lambda_{\text{cent}}$ is the user-chosen central wavelength of the spectrograph in nanometers, and $\lambda(i)$ is the wavelength in nanometers corresponding to pixel $i$. In this paper, only the commissioning of the low resolution observing mode is described, as the medium resolution mode has not yet been fully tested on sky.

- **Andor Ixon EMCCDs:** VISION features two identical 128×128 pixel Andor Ixon DU 860 EMCCDs, with 24 $\mu$m square pixels and quantum efficiencies of 70-85% over 550-850 nm at $-50^\circ$ C and dark current of 0.002 electrons/pixel/second. For recording stellar interferograms, the EMCCDs are operated at $-50^\circ$ C, with 6 ms exposure times, electron multiplying gains of 300, and fast readout rates of 10 MHz with vertical clock speeds of 0.1 $\mu$s to minimize clock induced charge (CIC) noise. The typical CIC event rate for the Andor Ixon EMCCDs was found to be $0.08 - 0.11$ events/pixel/frame. Longer exposure times of 10-12 ms were tested on sky resulting in interferograms with significantly reduced fringe contrast due to atmospheric turbulence. Custom C++ and Python code controls data acquisition, the fringe searching, the fringe tracking, the spectrographs, the shutters, and the single-mode fiber positioners using a computer running Ubuntu Linux OS 12.04.

### 4.3.2 Raw Interferograms & Calibration Data

VISION requires large amounts of support measurements to calibrate the raw interferograms of a given star. A complete VISION data set for extracting photometrically calibrated visibilities and closure phases is shown in Figure 25 for beams 1 and 4. For both the fringing and photometric cameras, the spatial direction is vertical in the figure, and the wavelength direction is horizontal.

A sample averaged interferogram is shown in the top center panel of Figure 25 from the combined light of beams 1 and 4 using a laboratory white-light source. To produce the interferogram, the light path length difference between beams 1 and 4 was minimized using the delay line carts. The averaged interferogram was constructed from several hundred co-added, dark subtracted, 20 ms frames with a gain of 300 in medium ($R \sim 1000$) resolution mode. The low resolution observing mode is not typically used for measurements illuminated by internal light sources because the laboratory light source path passes through the $^{70}/_{20}$ beam splitters in transmission, leading to significant dispersion. The different types of data necessary to extract calibrated squared visibilities and closure phases from any given set of interferograms are:

- **Darks** are frames with no starlight on the detector. For each data set, $\approx 5 \times 10^3 - 10^4$ six-ms dark frames are recorded (requiring 30–60 seconds of real time). Darks are recorded by blocking incoming starlight by closing all shutters at the front of the VISION optical bench. Darks are recorded semi-hourly

throughout the night for typical observing to carefully characterize the clock induced charge and bias count levels. The sky background is not included in the darks, as it is not a significant source of photons given that VISION observes bright ($R_{\mathrm{mag}} < 4$) stars. Darks are used to estimate the EMCCD read noise, gain, and CIC rate, which are necessary parameters for extracting calibrated squared visibilities, bias-corrected closure phases, and triple amplitudes from raw interferograms. Sample average dark frames are shown in the left panels of Figure 25 for the fringing and photometric cameras.

- **Foregrounds** are frames with incoherent light from all beams on the detector. Incoherent light is obtained when the delay line carts are moved many coherence lengths away from the fringing position. A sample foreground for beams 1 and 4 is shown in the bottom-center panel of Figure 25. Foregrounds are used to characterize the Gaussian profiles from the single-mode fibers on the fringing camera. This is needed to compute the power spectrum and bispectrum biases, which are in turn needed for calibrating squared visibilities and triple amplitudes.

- **Real-Time Flux Estimation.** The flux for each beam is recorded simultaneously with the interferograms. A sample image from the photometric camera with beams 1 and 4 is shown in the bottom right and top right panels of Figure 25. The real-time flux is used to estimate the system visibility due to beam intensity mismatch. The photometric imbalance between two beams with in-

tensities $I_A$, $I_B$ will reduce the visibility by $\frac{2\sqrt{I_A I_B}}{I_A+I_B}$(Coudé du Foresto et al., 1997). The fringing camera beam fluxes $I_{f,A}$ and $I_{f,B}$ are estimated from the photometric camera beam fluxes, as described next.

- **Single Telescope Data.** A sample set of single telescope data for beams 1 and 4 is shown in the center panels of Figure 25. The precise ratio of fluxes between the fringing and photometric cameras using the polarizing beam splitter can deviate from an exact $^{50}/_{50}$ split. This is the result of slightly varying polarization of light from the several telescopes, which is due to the siderostats' motions when tracking stars. Thus, the fringing-to-photometric light flux ratio can vary from star to star and night to night at different wavelengths. In order to calibrate this effect, the time and wavelength dependent flux ratio $\alpha(\lambda)$ between the fringing and photometric cameras are measured for each beam and for each star observed. This flux ratio is then used to correlate the real-time flux for each beam on the photometric camera to the fringing camera. The flux for each beam on the fringing camera is given as:

$$I_{f,i}(\lambda, t) = \alpha_i(\lambda, t) I_{p,i}(\lambda, t). \tag{14}$$

$I_{f,i}(\lambda, t)$ is the flux at wavelength $\lambda$ and time $t$ on the fringing camera for beam $i$, and $\alpha_i(\lambda, t)$ is the measured wavelength- and time-dependent flux ratio between

the fringing and photometric cameras using single beam data for beam $i$:

$$\alpha_i(\lambda) = \frac{I_{f,i}(\lambda)}{I_{p,i}(\lambda)} \tag{15}$$

where the fringing-to-photometric camera flux ratio $\alpha_i(\lambda)$ is measured using single beam data (center panels, Figure 25). Equations 14 and 15 are used to estimate the flux on the fringing camera for each beam, $i$, separately. The estimated fluxes for each beam on the fringing camera are used to correct observed squared visibilities and triple amplitudes for beam intensity mismatch.

### 4.3.3 Daily Alignments

A series of daily alignments are performed for each of the six beams to maximize the starlight throughput for on-sky observations, using a 632.8 nm HeNe laser source. The procedure is as follows:

1. Align the "switchyard" mirror (top panel, second mirror in the light path of Figure 23) to the $^{70}/_{20}$ beam splitters in order to route each beam towards the VISION "switchyard" table.

2. Mount the $^{70}/_{20}$ beam splitters and accompanying beam-shear compensating windows. The beam splitters route light from the feed system to the VISION optical bench.

3. Place an auto-collimation mirror directly in front of each of the $^{70}/_{20}$ beam

splitters, thus retro-reflecting the HeNe laser back on itself and to the VISION optical bench. This is necessary because the HeNe laser light path is opposite that of the feed system.

4. Align the $^{70}/_{20}$ beam splitters (top panel, Figure 23) to place the laser spot as close as possible to the fiber tip of each single-mode fiber.

5. Align each fiber with an automated algorithm that directs the fiber to move horizontally and vertically to the optical bench until the laser light coupled to the fiber is at maximum. This alignment algorithm typically is repeated twice, once as a rough pass with total grid search size of 32×32 $\mu$m, and once with a smaller grid search size of 8×8 $\mu$m. Occasionally, the fiber focus for each beam is determined using the fiber alignment algorithm.

6. Remove the auto-collimation mirrors, and after acquiring a star, re-align the fibers to maximize the coupling of starlight to each fiber.

## 4.4 Data Acquisition

### 4.4.1 Fringe Searching

The fringe search algorithm acquires fringes by automatically stepping the delay line carts back and forth until the fringes are found. For the first star observed each night, this procedure typically takes several minutes. After that, offsets of 1–3 mm in the cart positions generally remain fixed throughout the night, and the fringe search-

ing on subsequent stars can take less than a few seconds. VISION takes advantage of the roughly equal spacing of the NPOI array to use the shortest baselines to phase the long baselines via baseline bootstrapping (Armstrong et al., 1998; Jorgensen et al., 2006). The fringe search algorithm uses up to 5 baselines for fringe searching and fringe tracking. For single stars that are resolved with NPOI baselines, the shortest baselines are typically used to fringe search, since the visibility is highest on the first peak of the visibility function. For binary stars, the baselines used for fringe tracking are strategically chosen based on the observed fringe SNR on each baseline, and this can be done in real time.

For example, for 3-way beam combination on a star using beams 2, 4, and 5, beam pairs 2-4 and 4-5 can be selected for fringe tracking while the longer baseline with beam pair 2-5 is also phased without additional delay line feedback. Each of the fringe searching and fringe tracking parameters are adjustable.

Next the fringe search algorithm is detailed for beams 2, 4, and 5 with the nominal settings:

1. First, the algorithm begins searching for fringes between beams 2 and 4 with an increasing search pattern around the nominal delay point, stepping delay line cart 4 by $\sim +20$ $\mu$m. If the fringe SNR is greater than the semi-lock SNR at least $\sim 3$ consecutive times, then the fringe is considered "found". The fringe SNR is estimated in the control system code after the sum of $\sim 20$ power spectra

co-adds:

$$\text{SNR} = \frac{\text{Peak of power spectrum}}{\text{Average power spectrum noise}}. \quad (16)$$

If the fringe is not found by the time the delay line cart has reached $\sim 500$ $\mu$m, the cart stepping reverses direction with steps of $\sim -20$ $\mu$m until the cart has reached $\sim -500$ $\mu$m.

2. If no fringe is found, the search range is repeated and increased by $\sim 2\times$, from $\sim -1000$ $\mu$m to $+\sim 1000$ $\mu$m about the nominal delay point. This search range is increased continually until the fringe is found, which is typically within $1-3$ mm of the nominal delay point for the first star observed that night.

3. Once the fringe is found, if the fringe SNR is greater than the track SNR, tracking begins on beam pair 2-4, with delay line feedback sent to cart 4 to correct for atmospheric piston errors. If the fringe SNR is lower than a separate "fringe-lost" SNR at least $\sim 3$ times, then the fringe searching for cart 4 resumes, with a small, fixed delay range of $\pm \sim 5$ $\mu$m.

4. The fringe search algorithm then repeats the above process to search for fringes between beams 4 and 5. Searching for fringes using delay line cart 5 is relative to any delay line feedback sent to cart 4. The fringe search algorithm automatically keeps the cart of the first beam given as the stationary cart. In this example, the algorithm was given tracking beam pairs 2-4 and 4-5 and thus cart 2 was kept stationary. If the algorithm is tracking beam pairs 4-2 and 2-5, it would

keep cart 4 stationary.

### 4.4.2 Fringe Tracking

Due to atmospheric turbulence, the path length that light travels from each star to the telescopes often changes on 10-500 ms timescales. To correct for this effect the fringes are tracked in real time using a fringe tracking algorithm. The fringe tracking code is written in C++ and installed on the VISION control system computer, which sends feedback directly to the delay line carts.

VISION forms spatially dispersed fringes on the fringing camera in real time, and thus avoids the need for modulation of the delay line mirrors to create temporal fringes. This design was chosen to avoid possible non-linear modulations in the shapes of the delay line modulations observed in NPOI classic, which can lead to cross talk between the fringe amplitudes and phases, when multiple baselines are observed with the same detector pixel.

A fringe-fitting approach is used to estimate group delay in the fringe tracking algorithm. The delay to move each of the five operational delay line carts is evaluated on $\approx$ 100 ms timescales to minimize the path length differences between the carts, ideally to within a few hundred nm or better. The fringe tracking approach uses a Fourier transform along the wavelength direction, and a direct fit to the data along the fringing (spatial) direction for each 6 ms frame of data. The theoretical fringe model for an image plane combiner adopted from Equation 10.1 on page 569 of Born

& Wolf (1999) is:

$$I(y) = I_1 + I_2 + 2\sqrt{I_1 I_2}|\gamma| \cos\left(fy + \arg(\gamma)\right) \tag{17}$$

where, $I_1$ and $I_2$ are the fluxes for beams 1 and 2 respectively. The coherence between the two beams $\gamma$ has both an amplitude $|\gamma|$ and a phase $\arg(\gamma)$, and the fringes are modulated by frequency $f$. Note that the phase can be instead represented by replacing the cosine function with independent cosine and sine functions each with independent amplitudes using the identity

$$\cos(\theta_1 - \theta_2) = \cos(\theta_1)\cos(\theta_2) + \sin(\theta_1)\sin(\theta_2);$$

the phase would be found as the inverse tangent of the ratio of sine to cosine amplitudes. This allows the nonlinear phase parameter to be replaced by linear coefficients, simplifying model fitting procedures.

If only a single telescope pair were being used, and if there were no further modulation of the fringe amplitude, the intensity pattern could be fit using a Fourier Transform, and implemented efficiently in real time using, for example, the Fast Fourier Transform algorithm (with attention to zero-pad the array for better sampling of the fringe frequencies $f$, since the fringe wavelengths will not necessary be integer fractions of the number of pixels).

In practice this theoretical fringe model is modulated by both a coherence envelope

(as a function of distance from zero differential optical path length) and detector illumination pattern, and multiple fringe signals are present simultaneously. The first can be modeled according to the instrument and source bandpasses (though only with nonlinear parameters), and the second according to incoherent illumination pattern measurements. For fringe tracking, a model combining the effects of the illumination pattern and fringing is used as follows (however, the coherence envelope is presently ignored in real-time analysis due to nonlinear parameter complexities).

Fringes are dispersed horizontally ($x$), with the fringing (delay) direction vertical ($y$). For a given spectral channel $x$, the interferogram is modeled as

$$I(x,y) = e^{-(y-P_1)^2/P_2^2}\left(P_3 + \sum_{k=1}\left[P_{4,k}\cos\left(P_{6,x,k}\left(y-64-P_{7,x,k}\right)\right) + P_{5,k}\sin\left(P_{6,x,k}\left(y-64-P_{7,x,k}\right)\right)\right]\right) \quad (18)$$

where $k$ is the index of each beam pair, $P_1$ and $P_2$ describe the approximately Gaussian illumination pattern on the detector, $P_3$ is the overall intensity, $P_{4,k}$ and $P_{5,k}$ are the cosine and sine amplitudes for each pair (with the phase $\phi$ given by $\tan\phi = P_{5,k}/P_{4,k}$ and the total fringe amplitude $\sqrt{P_{4,k}^2 + P_{5,k}^2}$), and $P_{6,x,k}$ is the (wavelength dependent) fringe frequency. More generally, the form can be written as

$$I(y) = \sum_{m=0}^{m=2N} A_m g_m$$

where

$$g_m(x,y) = \begin{cases} 1 & m = 0 \\ e^{-(y-P_1)^2/P_2^2} \cos\left(P_{6,x,k}\left(y - 64 - P_{7,x,k}\right)\right) & m = 2n-1,\, m \,\text{odd} \\ e^{-(y-P_1)^2/P_2^2} \sin\left(P_{6,x,k}\left(y - 64 - P_{7,x,k}\right)\right) & m = 2n,\, m \,\text{even} \end{cases}$$

and these functions can be precomputed based on laboratory evaluations of the Gaussian profile parameters $P_1$ and $P_2$, fringe frequencies $P_{6,x,k}$, and internal differential dispersion $P_{7,x,k}$ (presently set to zero). The remaining coefficients $A_m$ are all linear, allowing for a single matrix inversion to solve the best $\chi^2$ fit. This is efficient to implement in real-time, whereas an iterative nonlinear fitting procedure would be prohibitively slow. It is also trivial to parallelize the fit computations, as each spectral channel's fit is evaluated independently.

The typical fringe tracking parameters are given in Table 23 and are optimized with on-sky observations in median seeing conditions. An exposure time of 6 ms is commonly used for the EMCCD. The typical fringe search step sizes are $\sim 12.5$ $\mu$m. During fringe tracking, two 6 ms frames are added together for a total on-sky coherent integration time of 12 ms (2 coherent co-adds). While a 12 ms effective exposure time on sky does reduce the fringe SNR (see Equation 16 in §4.4.1) due to the atmospheric fluctuations, the added flux more than makes up for the lost fringe SNR. Fringe fitting is done as described above using Equation 18 to determine $P_4$ and $P_5$. The group delay for each telescope pair is estimated by treating $P_4$ and $P_5$ as the real

and imaginary components of a 1D Fourier Transform (FT) for that frequency, and another 1D FT along the wavelength direction using the FFTW[2] program in C++ (M. Frigo and S. G. Johnson , 2005) is performed. The resulting power spectrum is coadded over thirty 12 ms co-added frames, for an effective in-coherent exposure time of 360 ms (30 incoherent co-adds) to generate a total power spectrum. The location of the peak of the total power spectrum corresponds to the delay that is sent to the delay line carts.

### 4.4.3 Observing Sequence

A complete observing sequence for a target or calibrator star is detailed in Table 21. After acquiring the star, the fibers are aligned to maximize the light coupled using an automatic fiber alignment algorithm. This step is typically required several times a night depending upon whether the observed fluxes are lower than expected. Next the different types of VISION data necessary to calibrate the observed interferograms in post-processing are recorded: darks, interferograms while fringe tracking, foregrounds, and single beam data, as detailed in §4.3.2.

Target star and calibrator star observation sequences are interleaved. Calibrator stars are selected that are typically 1–4 mas (depending upon whether longer (30–80 m) or shorter (8–12 m) baselines are used) to correct for the system visibility drift and bispectrum bias in the data. For typical $\approx$ 2 hour observations of a given star,

[2]http://www.fftw.org/

a calibrator-target-calibrator pattern is alternated on $\approx 20$ minute timescales, given that single beam and foreground data are required. A typical VISION observation of a star produces 20–50 GB of raw data, and consists of $\approx 10^6$ individual frames with 6 ms exposures; an observing run typically produces 200–400 GB of raw data per night.

### 4.4.4 Faint Magnitude Limit

Fringe detection has been demonstrated with current hardware at apparent magnitude $R_{\rm mag} = 4.5$, in excellent seeing. Funds from the Office of Naval Research DURIP competition have recently been received to replace the existing Andor DU-860 EMCCDs used for fringe detection and intensity mismatch monitoring with new Nüvü EMCCDs. The new EMCCDs feature $\times 10$ less CIC noise (0.005 events pixels$^{-1}$ per frame) as compared to our measured CIC of $0.08 - 0.11$ events pixels$^{-1}$ per frame. This reduced noise is expected to greatly improve our faint magnitude limit.

## 4.5 Characterizing the VISION instrument

### 4.5.1 System Throughput

An observed throughput of 0.67% was measured using the average total flux of of $\gamma$ Orionis on the night of March 16, 2015, in median seeing. The total observed

photons per second $F_{\rm obs}$ for $\gamma$ Orionis was estimated as:

$$F_{\rm obs}(\text{phot s}^{-1}) = \sum_{i=0}^{i=127} \frac{\pi}{4} D^2 < F_0 > 10^{-0.4(R_{\rm mag}+kz)} \frac{\lambda_i}{hc} \Delta\lambda < T > \qquad (19)$$

where $i$ is the pixel index on the VISION fringing and photometric cameras, $D = 12.5$ cm is the effective collecting area diameter, $k = 0.11$ is the extinction in $R$-band in magnitudes, $z = 1.43$ is the airmass during the observations, $< F_0 >= 2.25 \times 10^{-9}$ ergs cm$^{-2}$ s$^{-1}$ Å$^{-1}$ is the zero magnitude $R$ band flux, $R_{\rm mag} = 1.73 \pm 0.1$ (Ducati, 2002) is the magnitude $\gamma$ Orionis from SIMBAD[3] (Wenger et al., 2000), $\lambda_i$ is wavelength of light at pixel $i$ on the cameras, $h$ is Planck's constant, $c$ is the speed of light, $\Delta\lambda \approx 1860$ Å is the wavelength range over the entire filter, and finally $< T >$ is the average throughput for the observations. $F_{\rm obs}$ for $\gamma$ Orionis was measured on both the fringing and photometric cameras on March 16, 2015 in median seeing. We computed the observed throughput, for both the fringing and photometric cameras by solving Equation 19 above for $< T >$.

Accounting for all optical surfaces from the telescopes to the beam combiner, a total theoretical throughput of ≈8.6% was computed by multiplying the reflectivity and transmission of all optical surfaces from the telescope to the VISION cameras including filter response and quantum efficiency as detailed in Table 22. The total observed throughput was ≈0.67%, which is nearly 13 times lower than the theoretical throughput. This significant difference could be due to the adopted throughput of

[3]http://simbad.u-strasbg.fr/simbad/

the NPOI feed system and the delay line carts of ≈75% and ≈73% respectively, as measured 9 years ago by Zhang et al. (2006). The loss of light in the feed system could be much larger due to 9 additional years of optical coating degradation. Similarly, the delay line cart mirrors have drifted out of focus, meaning the adopted theoretical fiber coupling efficiency of 55% is likely overestimated. An additional cause of lost light is that the fringing camera does not sample the full Gaussian profile from each fiber on the detector as shown in Figure 27, which leads to ≈ 30% loss in light. Finally, the misalignment of the focusing optics for light from the multi-mode fiber output to the photometric camera also could lead to an additional loss of light for beams 3 and 5, which are on the edges of the photometric camera chip.

### 4.5.2 Beam Overlap

Fringes can only exist where the Gaussian beam profiles of each single-mode fiber overlap on the fringing camera. The Gaussian beam profile was measured for each beam individually on the fringing camera using a laboratory white light source, 20 ms exposure times, a gain of 300, and the low resolution $R = 200$ observing mode. Ten minutes of frames were recorded on the fringing camera for each beam to build high-SNR Gaussian beam profiles. Figure 27 illustrates the overlap for all 5 beams averaged over $570 - 850$ nm. With the exception of beam 3, the percent flux overlap for each beam with each other beam is $> 90\%$. The percent flux for beam 3 that overlaps with beams 1, 2, 4, and 5 is $72\% - 79\%$. The lower overlap for beam 3 is likely

due to a slight misplacement of the fiber for beam 3 in the V-groove array. The lower overlap fraction in beam 3 can lead to slightly lower fringe contrast between beam 3 and the other beams. These systematic differences in visibility can be removed by observing a calibrator star.

### 4.5.3 Laboratory Fringe Model

Given that VISION uses single-mode fibers, high visibilities of $> 80\%$ are expected for all beam pairs under ideal laboratory conditions, similar to commissioning tests of other beam combiners such as MIRC and AMBER (Petrov et al., 2007) that use optical fibers. This maximum possible visibility measured for a given beam pair under ideal conditions is the "system visibility". In order to verify that the system visibility is $> 80\%$, a fringe model was chosen to match sets of high signal-to-noise laboratory fringes that do not suffer from visibility loss due to beam intensity mismatch and atmospheric turbulence or CIC noise.

Equation 18 was parameterized making the basic fringe model directly comparable to VISION interferograms, at a single wavelength channel:

$$I(x,y) = e^{-(y-P_1)^2/P_2^2}\left(P_3 + \sum_{k=1}\frac{\sin(P_8 y + P_9)}{P_8 y + P_9}\left[P_{4,k}\cos\left(P_{6,x,k}\left(y - 63.5 - P_{5,k}\right)\right)\right]\right) \tag{20}$$

where parameters $P_{4,k}$ and $P_{5,k}$ are redefined as overall fringe amplitude and phase, and new parameters $P_8, P_9$ are introduced modulation by the coherence envelope due

to the finite spectral resolution of the detector, which can be modeled by integrating over several wavelengths.

The integration is done by evaluating the fringe model at 0.01 pixel steps, or $1.28 \times 10^4$ evenly spaced points from pixels 0 to 127, and integrating the resulting model fringe to 128 pixels. By integrating, the pixelation of each interferogram by the finite spectral resolution is modeled. The fringe model (Equation 20) assumes a rectangular bandpass, due to the use of a sinc function. The model is an approximation given that the VISION bandpass is likely closer to a Gaussian and not square (as dictated by a sinc function) for each resolution element, but was sufficient for the present study.

The system visibilities for all 10 available beam pairs (beams 1–5) were measured under laboratory conditions using the fringe model above. The fringe parameters for each beam pair were evaluated by fitting the fringe model in Equation 20 to interferograms from a laboratory HeNe 632.8 nm laser source. The visibility was estimated as the ratio between total flux on the detector and the amplitude of the coherence:

$$V = \frac{P_4}{P_3} = 2\frac{\sqrt{I_1 I_2}}{I_1 + I_2}|\gamma|. \tag{21}$$

The procedure to obtain the interferograms for each beam pair was as follows. First, a 632.8 nm HeNe laser source was coupled to the single-mode fiber of each beam. The delay line carts were positioned to minimize light path difference between the two beams to within the coherence length ($\lesssim 1300$ $\mu$m), maximizing the visibility for a given pair of beams. Several minutes of 2-ms exposure time raw interferograms

were recorded for each beam pair and the gain set to zero. Electron multiplying gain was not used in order to avoid additional multiplication noise. A time averaged dark was subtracted from each of the raw interferograms to remove the bias counts on the EMCCD. A median selected dark was not used because there was negligible CIC on the detector when running the EMCCD with zero gain.

The system visibility was $V_{\text{laser}} \approx 85 - 97\%$, as expected when using single-mode fibers. Fitting was performed using IDL's MPFIT[4] which employs a modified Levenberg-Marquardt $\chi^2$ minimization to fit the fringe model (Equation 20) to the interferograms. Sample interferograms for each beam and model fits are shown in Figure 28. The residuals between the fringe model and the interferograms are 1–5% as shown in Figure 29, as expected given the imperfect fringe model (e.g. sinc envelope instead of Gaussian). Nevertheless, the laboratory system visibilities for VISION were $> 80\%$ for all beam pairs, as expected.

### 4.5.4 Fringe Crosstalk

Fringe analysis based on Fourier Transforms shows slight overlap among the peaks in the power spectra from each beam pair (see Figure 24). This is because the fringes do not fit along the 128 pixels of the fringe direction an exact integer number of times. While the fringe frequencies were selected to be unique and produce orthogonal intensity pattern functions, sinusoids are only orthogonal on domains in which both

[4]http://www.physics.wisc.edu/∼craigm/idl/down/mpfit.pro

sinusoids have an exact integer number of waves. (Even if a perfect integer number of waves fit across the detector for one wavelength, this would not be the case for other wavelengths.) As a result, the fringe sinusoids are not strictly orthogonal functions on the domain of 128 pixels, though they may be unique and orthogonal overall. This results in perceived cross-talk between channels even in the case of a perfect setup (instrumental alignment inaccuracies will add to the effect). This is independent of the method used to evaluate the fringe models and instead related to the non-orthogonality of the basis functions on the 128 pixel restricted domain.

As expected, the observed crosstalk between peaks in the power spectra were found to occur between pairs of beams that are closest in fringe frequency such as beam pairs 1-4 and 2-5. The crosstalk percentage was calculated as the total power in the power spectrum for each beam pair at the location of the peak of each other beam pair. The magnitude of the fringe crosstalk using the Fourier Transform method was found to be $\approx 1 - 8\%$ of the power in the power spectra for the laboratory fringes. Fringe fitting with better fringe models (including illumination profile, coherence reduction far from zero optical path delay, dispersion, etc.), as described in §4.4.2 and below, can improve but not entirely eliminate these effects.

In an attempt to further understand the crosstalk, a multi-fringe model based on Equation 20, was used to fit fringes from multiple beam pairs on the detector. Laser fringes from beam pairs 1-4 and 2-5 were added together and fit for parameters of both beam pairs simultaneously.

In Figure 31 the $\chi^2$ space is mapped by varying the amplitude of the fringes, parameter $P_{4,k}$ for both beam pairs 1-4 and 2-5 in Equation 20 above. For two parameters of interest, $\Delta\chi^2 = 2.30$, 6.17, and 11.8 for $1\sigma$, $2\sigma$, and $3\sigma$ confidence intervals respectively (Press et al., 2002). Even for ideal, high SNR fringes, a correlation in the visibilities is seen of both beam pairs at the $\approx 2\%$ level for the $3\sigma$ confidence interval. This could also be interpreted as a form of crosstalk. This test suggests that the $\chi^2$ minimization between a multi-fringe model and multi-fringe data likely leads to correlations between the visibility parameters and is thus a manifestation of crosstalk, similar to the overlapping peaks in the power spectra.

## 4.6 The VISION Data-Processing Pipeline

### 4.6.1 Dark Subtraction Algorithm

Dark frames are used to subtract the bias counts for all raw calibration data and interferograms. The bias counts are important to characterize given that average signal counts can be as low as $\approx 0.1$ photons/pixel/frame for $R_{\rm mag} \approx 3.5$ stars. Bias level subtracted interferograms and calibration data are used in the data processing pipeline. Following Harpsøe et al. (2012) the bias count levels on the photometric and fringe camera chips were characterized by the sum of time-dependent (frame to frame) and spatially dependent bias counts:

$$b(x, y, t) = b(x, y) + b(t) \tag{22}$$

where $b(x, y, t)$ are the bias counts at pixel $(x, y)$, and time $t$. Andor's "baseline clamp" software stabilizes $b(t)$ for each frame by subtracting off a running average of a 128 pixel overscan region of the chip and then adding back in 100 Analog-to-Digital Units (ADU). The output probabilities of ADU for the EMCCDs are characterized using an analytic model that is a convolution of the probability that a pixel will have a CIC event or just a bias count (Equation 8, Harpsøe et al., 2012).

This analytic EMCCD model was modified to include the probability that two CIC events occur in the same pixel, given that the probability of a CIC electron is $\approx 8-11\%$ for the EMCCDs, and thus the probability of two concurrent CIC electrons was $\approx 0.6 - 1.2\%$, which is significant for characterizing the high end tail of pixels with $> 200$ ADU:

$$P(Z = n) = \int_0^n \left[ (1-p-p^2) \left( \delta(x) + \left( \frac{p}{G} e^{-x/G} + \frac{p^2}{G^2} x e^{-x/G} \right) H(x) \right) \right] \times N(n-x, \sigma_{\mathrm{RN}}) dx \tag{23}$$

where $P(Z = n)$ is the normalized probability that a given pixel will have output $n$ ADU. Furthermore, $p$ is the probability of CIC, $G$ is the gain, $\sigma_{\mathrm{RN}}$ is the read noise in ADU, $H(x)$ is the heaviside step function, and $N(n - x, \sigma_{\mathrm{RN}})$ is the normal distribution that describes the bias counts $b(x, y)$ at each pixel:

$$N(n - x, \sigma_{\mathrm{RN}}) = \frac{1}{\sqrt{2\pi\sigma_{\mathrm{RN}}^2}} e^{-(n-x)^2/(2\sigma_{\mathrm{RN}}^2)} \tag{24}$$

where $N(n - x, \sigma_{\mathrm{RN}})$ describes the bias counts (which has Gaussian read noise) when

no CIC event occurs. If a CIC event occurs, the output counts $n$ from the EMCCD go as $\frac{e^{-x/G}}{G}$ (Basden & Haniff, 2004).

This EMCCD model was tested by fitting a histogram of $10^5$ raw dark frames from the fringing camera on a pixel by pixel basis to derive a bias count level $b(x, y)$, read noise $\sigma_{\mathrm{RN}}(x, y)$, gain $G(x, y)$, and CIC probability $p(x, y)$. The darks were recorded with 6 ms exposures, and a gain setting of 300 on the camera. The modified Levenberg least squares minimization algorithm MPFIT (Markwardt, 2009) was used to fit the EMCCD model to the darks. A sample fit to pixel $(x, y) = (50, 50)$ is shown in Figure 32. The EMCCD model fit the data well with small residuals. The typical read noise was $\sigma_{\mathrm{RN,obs}} \approx 3.5$ ADU[5], gain of $\approx 16 - 18$, and clock induced charge probability of $\approx 11 - 13\%$ averaged over the entire chip for the fringing camera. The observed gain of $\approx 16 - 19$ is $258 - 305$ when multiplied by the $e^-$/ADU conversion of 16.3 and 16.1 for the fringing and photometric camera, respectively. This gain is comparable to the camera gain setting of 300 for these darks. The read noise, gain, and CIC were similar for the photometric camera. Andor's listed CIC rate of 0.05 events/pixel/frame for the cameras is likely underestimated since it does not include CIC events buried within the read noise. A higher CIC rate of $0.08 - 0.11$ events/pixel/frame was measured and accounted for CIC within the read noise using the EMCCD model above.

[5]Following the literature convention, counts instead of electrons are used given that the gain on an EMCCD is stochastic and varies as a function of time and location on the detector. Therefore there is no exact conversion between electrons and ADU for an EMCCD.

With a derived CIC $p(x, y)$ and gain $G(x, y)$ from fitting dark frames using Equation 23, the dark subtraction algorithm of Harpsøe et al. (2012) was used to subtract the bias count level. First, the mean bias level for each raw frame was computed using pixel 127 to further stabilize the frame to frame bias count variability:

$$b_o(t) = \text{avg}\Big[c(127, y, t) - b(127, y)\Big] \tag{25}$$

where $c(127, y, t)$ are pixel values for the raw frame at pixel $x = 127$. Finally, the bias counts from each raw frame are subtracted as:

$$c_b(x, y, t) = c(x, y, t) - [b(x, y) + b_o(t)] - G(x, y)p(x, y) \tag{26}$$

where $c_b(x, y, t)$ is the bias count subtracted frame.

### 4.6.2 Pre-Processing Raw Interferograms

Prior to extracting squared visibilities, closure phases, and triple amplitudes from raw interferograms, the following steps are performed:

1. estimate the gain, read noise, and clock induced charge for darks,
2. perform dark subtraction,
3. remove poor quality interferograms, and
4. bin the data spectrally to increase SNR.

First, a series of dark frames taken during the observing sequence (see §4.4.3) is used to estimate the gain, clock induced charge rate, and read noise for the raw interferograms as detailed in §4.6.1 above. Next, dark subtraction is performed using Equation 26 from §4.6.1 above. Raw interferograms for which the fringe tracking SNR is so low that no fringes were identified are removed. This loss of coherence can occur often due to the turbulence of the atmosphere at visible wavelengths. With this step 1–5% of the raw interferograms that have the lowest fringe SNR (see §4.4.2) are removed. Next, spectral channels with very little light are removed. For stars with spectral types O–F, typically only spectral channels with wavelengths $580 - 750$ nm are used, given that the single-mode fibers enter multimode at $< 580$ nm and spectral channels with wavelengths $> 750$ nm had too little SNR. Next, these spectral channels are binned in the wavelength by a factors of 8, 9, or 10. For a typical 9 spectral channels, this results in an overall read noise of $\sigma_{\mathrm{RN,binned}} = \sqrt{9}\sigma_{\mathrm{RN,obs}} \approx 10.5$ ADU, and $\approx 19$ nm per spectral channel. Finally, the raw interferograms are divided by the mean gain as derived above, typically $15 - 18$ ADU/$\mathrm{e}^-$.

### 4.6.3 Adapting the MIRC Data-Processing Pipeline for VISION

Since MIRC and VISION are nearly identical in design, the MIRC data-processing pipeline (Monnier et al., 2004, 2007) was modified to estimate calibrated squared visibilities, closure phases, and triple amplitudes from interferograms pre-processed as detailed in §4.6.2 above. Briefly, the MIRC pipeline measures uncalibrated squared

visibilities and triple amplitudes from raw interferograms after a series of Fourier transformations and foreground subtractions. The MIRC pipeline then calibrates the squared visibilities and triple amplitudes using fluxes measured simultaneously with fringes. The last step of the MIRC pipeline is to use calibrators with known sizes to compensate for system visibility drift.

A significant change to the MIRC pipeline for processing VISION interferograms is the use of single 6 ms frames to estimate the uncalibrated squared visibilities. By contrast, MIRC pipeline coherently co-adds several frames of data before estimating uncalibrated squared visibilities. In adapting the MIRC pipeline, the complex bispectrum bias must also be corrected on a frame by frame basis, since VISION data are photon noise limited whereas MIRC data are read-noise limited; the MIRC pipeline only partially implements this correction, since MIRC operates in a regime where photon noise bias in the bispectrum is rarely important.

The uncorrected bispectrum is given as

$$B_{0,ijk} = C_{ij} C_{jk} C_{ki} \tag{27}$$

where $B_{0,ijk}$ is the bispectrum for beams $i, j, k$, and $C_{ij}$ is the complex discrete Fourier transform for beam pair $i, j$. The triple product bias was adopted from EMCCD simulations of Basden & Haniff (2004), with an additional read noise term from

Gordon & Buscher (2012) that was modified for the EMCCDs:

$$B_{1,ijk} = B_{0,ijk} - 2\Big(|C_{ij}|^2 + |C_{jk}|^2 + |C_{ki}|^2\Big) + 6N + 6N_{\rm pix}\sigma^2_{\rm RN,binned}. \qquad (28)$$

where $|C_{ij}|^2$ is the power spectra, $N$ is the total number of counts in the frame, $N_{\rm pix} = 128$ is the total number of pixels in the spectral channel, $B_{1,ijk}$ is the bias-corrected bispectrum, and $\sigma_{\rm RN,binned}$ is the summed read noise in quadrature over the wavelength-binned pixels in Equation 28.

Equation 28 was derived by attempting to recover the correct closure phases extracted from simulated fringes of a binary star with an input orbit, a simulated EMCCD gain register, and added read-noise and Poisson noise. The EMCCD simulations of Basden & Haniff (2004) were replicated, and their Equation 4 was extended by adapting the Gordon & Buscher (2012) treatment of read noise, yielding an extra term of $6N_{\rm pix}\sigma^2_{\rm RN,binned}$. Gordon & Buscher (2012) provide equations to correct the bispectrum in the presence of read noise, but their equations only apply for Poission statistics, and the output of the EMCCDs is non-Poissonian due to the stochastiscity of the electron multiplying gain. As detailed in Basden & Haniff (2004), the coefficients of 2 and 6 multiplied by the power spectra $|C_{ij}|^2$ and total counts $N$ in Equation 28 also differ from the traditional Wirnitzer (1985) coefficients of 1 and 2 given that the output from an EMCCD is not Poissonian. The VISION implementation uses the bispectrum bias subtraction in Equation 28 on a frame-by-frame basis as recommended by both Basden & Haniff (2004) and Gordon & Buscher (2012) for

extracting unbiased closure phases and triple amplitudes from VISION raw interferograms.

The corrected bispectrum $B_{1,ijk}$ should be zero within error for foreground data, given that these data have no fringes. Therefore, Equation 28 was further tested by comparing the uncorrected bispectrum $B_{0,ijk}$ of a sample set of foregrounds to the theoretical bispectrum bias:

$$B_{0,ijk} \text{ of Foreground} = -2\Big(|C_{ij}|^2 + |C_{jk}|^2 + |C_{ki}|^2\Big) + 6N + 6N_{\text{pix}}\sigma^2_{\text{RN,binned}}. \quad (29)$$

$B_{0,ijk}$ was computed for foreground data from observations of $\gamma$ Orionis, and it closely matched the right side of Equation 29 above, as shown in Figure 34. This further validated that the derived bispectrum bias correction (Equation 28) for the EMCCDs was correct.

The theoretical prediction for the power spectrum bias was also derived as a modified version of the Gordon & Buscher (2012) power spectrum bias adapted for EMCCDs, in the presence of read noise:

$$|C_{1,ij}|^2 = |C_{0,ij}|^2 - 2N + N_{\text{pix}}\sigma^2_{\text{RN,binned}} \quad (30)$$

where $|C_{1,ij}|^2$ is the corrected power spectrum and $|C_{0,ij}|^2$ is the uncorrected power spectrum. Similar to the previous approach, foreground data contains no fringes and therefore no peaks in the power spectrum. Thus, the corrected power spectrum

$|C_{1,ij}|^2$ should be zero. The power spectrum bias correction matches the uncorrected power spectrum $|C_{0,ij}|^2$ to within 1% as shown in Figure 35.

## 4.7 The Orbit and Flux Ratio of $\zeta$ Orionis A

To both provide a first on-sky science result and to verify the VISION data-processing pipeline from §4.6.2 and §4.6.3, VISION was used to obtain new resolved observations of the massive binary star $\zeta$ Orionis A. The orbit and flux ratio of $\zeta$ Orionis A have previously been measured by Hummel et al. (2013), therefore the new observations serve as an established test of the VISION system and provide an additional epoch of constraint on the orbit of this benchmark astrometric binary.

$\zeta$ Orionis A was observed on March 16th, 2015, with stations AC, AE and N3, with baselines between $10.77 - 25.92$ m using the observation sequence in Table 21. Fringe searching and tracking were performed as described in §4.4.1 and §4.4.2. The calibrator star $\gamma$ Orionis ($\theta_{\rm UD} = 0.701 \pm 0.005$; Challouf et al., 2014) was observed immediately after, using the same observing sequence to compensate for any visibility drift. The wavelength solutions for the cameras from §4.3.1 was used.

Sample squared visibilities versus time for $\gamma$ Orionis are shown in Figure 33. The squared visibility drift for VISION as measured using $\gamma$ Orionis is $0.01 - 0.02$ over 30 minutes. Dark subtraction was performed on all the raw frames of $\zeta$ Orionis and the calibrator $\gamma$ Orionis as described in §4.6.1. The data were pre-processed as described in §4.6.2 and calibrated squared visibilities and bias-corrected closure phases were

extracted as described in §4.6.3.

From the orbit of Hummel et al. (2013), $\zeta$ Orionis A is predicted to have a separation of $40.1 \pm 1.0$ mas and a position angle of $223.2 \pm 2.3°$ at the epoch of the observations, with a flux ratio of $2.2 \pm 0.1$ mag. The $1\sigma$ errors on the predicted separation and position angle were calculated from distributions of separation and position angle from $10^7$ uniformly randomly selected orbits from the reported $1\sigma$ errors of the orbital elements from Hummel et al. (2013) and then projected on sky.

The new observations of $\zeta$ Orionis A with VISION yield a best-fit separation of $40.6 \pm 1.8$ mas, a position angle of $223.9 \pm 1.0°$, and flux ratio of $2.18 \pm 0.13$ mag at $580-750$ nm and are listed in Table 24. A sample of the extracted squared visibilities and closure phases along with the best fit model are shown in Figure 36. The median error on the closure phase is 1.9° and on $V^2$ is 4.5%. The error increases towards redder wavelengths due to decreased SNR, which is in part due to a decrease in quantum efficiency of 83% to 73% from 600 to 750 nm. The formal $1\sigma$ errors were plotted on the fitted orbit and flux ratio using $1\sigma$ confidence intervals with $\Delta\chi^2 = \chi^2 - \chi^2_{\rm min} = 3.53$, which corresponds to $1\sigma$ for 3 parameters of interested (Press et al., 2002). The $1\sigma$, $2\sigma$, and $3\sigma$ confidence intervals for the fitted orbit to $\zeta$ Orionis are shown in Figure 37. Finally, as shown in Figure 38, there is excellent agreement between the observed separation and position angle for $\zeta$ Orionis A as observed by VISION versus that predicted by the previously published orbit (Hummel et al., 2013).

## 4.8 Conclusions & Future Work

This paper introduces the VISION beam combiner for NPOI: a six-telescope image plane combiner featuring optical fibers, electron multiplying CCDs, and real-time photometric monitoring of each beam for visibility calibration. The VISION cameras, the fringe crosstalk, and the system visibility have been characterized, and a version of the MIRC data-processing pipeline has been adapted and verified for VISION with an observation of the benchmark astrometric binary star $\zeta$ Orionis A.

Future work on the instrument includes installation of new Nüvü cameras with 10 times less clock-induced charge noise. Recently, the 750 mm fringe-forming lens was replaced with a 500 mm lens to fully sample the Gaussian profile on the fringing camera, with early indications showing a gain of 30% flux, as well as a significant reduction in fringe crosstalk. Finally, the control system code will be updated from a text user interface to a graphical user interface.

With the capabilities demonstrated here, we anticipate now being able to use VISION to make the first 5- or 6-telescope reconstructed images at visible wavelengths of the main sequence stars Altair and Vega, as well observations of triple star systems and the TiO lines on the surfaces of spotted red supergiant stars.

Table 20
Laser Fringe Results

| Beam Pair | Pixels Per Fringe | Fitted Visibility |
|---|---|---|
| 1-3 | 39.38 | $0.968 \pm 0.006$ |
| 2-4 | 16.52 | $0.969 \pm 0.010$ |
| 1-4 | 13.89 | $0.939 \pm 0.009$ |
| 2-5 | 11.91 | $0.949 \pm 0.019$ |
| 3-4 | 10.45 | $0.954 \pm 0.010$ |
| 1-2 | 7.64 | $0.922 \pm 0.005$ |
| 4-5 | 7.01 | $0.884 \pm 0.018$ |
| 2-3 | 6.48 | $0.928 \pm 0.008$ |
| 1-5 | 4.65 | $0.858 \pm 0.015$ |
| 3-5 | 4.20 | $0.867 \pm 0.014$ |

Table 20: Pixels per fringe and raw visibility derived from the model fits to the 632.8 nm HeNe laser fringes in Figure 28.

Table 21
Observing Sequence

| | |
|---|---|
| Align Fibers | 120 s |
| Take Darks | 30 s |
| Fringe Search | 30 s |
| Record Fringes | 720 s |
| Record Foreground | 60 s |
| Record Single Beams 1−6 | 45 s per beam |
| Total | 1230 s |

Table 21: The observing sequence for each target or calibrator star. Raw interferograms are recorded while fringe tracking. The fibers only need to be aligned a couple of times per night. The rest of the data obtained are used to calibrate these raw interferograms: "Dark" frames are used to subtract off the bias counts of the EMCCDs. "Foreground" frames are observations of the star with incoherent flux (no fringes). These data are used to characterize the bias in power spectrum and triple amplitudes. "Single Beam" frames are the flux measurements of each beam individually, which is used to measure how the polarizing beam splitter splits light between the photometric and fringing cameras at each wavelength.

Table 22
Throughput

| Reflection | |
|---|---|
| Feed System | 75% |
| Delay Line Carts | 73% |
| $^{70}/_{20}$ Beam Splitter, (20% to Tip/Tilt) | 70% |
| 3 Inch Flat Mirror (Protected silver coating) | 96% |
| 2 Inch Flat Mirror (Silver coating) | 98% |
| Off Axis Parabola (Silver coating) | 98% |
| Fiber Coupling Efficiency ($r_0 = 9$ cm) | 55% |
| Fiber Fresnel Air-to-Glass | 92% |
| Lenslet Array at output of Fibers | 98% |
| **Light to Fringing Camera** | |
| Polarizing Beam Splitter $S$ mode | 50% |
| Fringe Focusing Lens (AR coating) | 97% |
| Cylindrical Lens (AR coating) | 98% |
| $R = 200$ Fringing Spectrograph Filter | 62% |
| Quantum Efficiency of Andor Ixon DU 860 (8% loss from air to chip) | 83% |
| **Throughput Fringing Camera (theoretical)** | ≈4.2% |
| **Throughput Fringing Camera (observed)** | ≈0.45% |
| **Light to Photometric Camera** | |
| Lenslet Array at input of Multi-mode Fibers | 98% |
| Polarizing Beam Splitter $P$ mode | 50% |
| $R = 200$ Photometric Spectrograph Filter | 62% |
| Quantum Efficiency of Andor Ixon DU 860 (8% loss from air to chip) | 83% |
| **Throughput Photometric Camera (theoretical)** | ≈4.4% |
| **Throughput Photometric Camera (observed)** | ≈0.22% |

Table 22: List of throughput for the VISION fringing and photometric cameras. Most VISION mirrors are silver-coated. The biggest single contributor to the loss of light is coupling to the single-model fibers. The theoretical fiber coupling efficiency of 55% is likely greatly over estimated due to feed alignment and delay line cart optics misalignments detailed in §4.5.1.

Table 23
Fringe Searching and Tracking Parameters

| | |
|---|---|
| EMCCD Exposure Time | 6 ms |
| Effective Coherent Exposure Time | 12 ms |
| Number of Coherent Co-adds | 2 |
| Effective In-coherent Exposure Time | 360 ms |
| Number of Incoherent Co-adds | 30 |
| Search Step Size | 12.5 $\mu$m |

Table 23: Fringe searching and tracking parameters detailed in §4.4.1 and §4.4.2. These optimal parameters were determined using on-sky observations in median-seeing conditions.

Table 24
Observations of $\zeta$ Orionis

| | | |
|---|---|---|
| HJD | 24557098.122 | |
| UT Date | 2015−03−17 | |
| Telescopes Used | AC−AE−N3 | |
| Baseline Length Range | $10.77 - 25.92$ m | |
| Wavelength Range | 570-750 nm | |
| # Closure Phases | 35 | |
| # $V^2$ | 90 | |
| Median Closure Phase Error | 1.9° | |
| Median $V^2$ Error | 4.5% | |
| | This Work | Hummel et al. (2013) |
| Separation (mas) | $40.6 \pm 1.8$ | $40.1 \pm 1.0$[1] |
| Position Angle (deg) | $223.9 \pm 1.0°$ | $223.2 \pm 2.3°$ [1] |
| $\Delta$Mag(570-750 nm) | $2.18 \pm 0.13$ | $2.2 \pm 0.1$[1] |

Table 24: Observations of $\zeta$ Orionis.
[1] Calculated at HJD= 24557098.122, using orbit of Hummel et al. (2013).

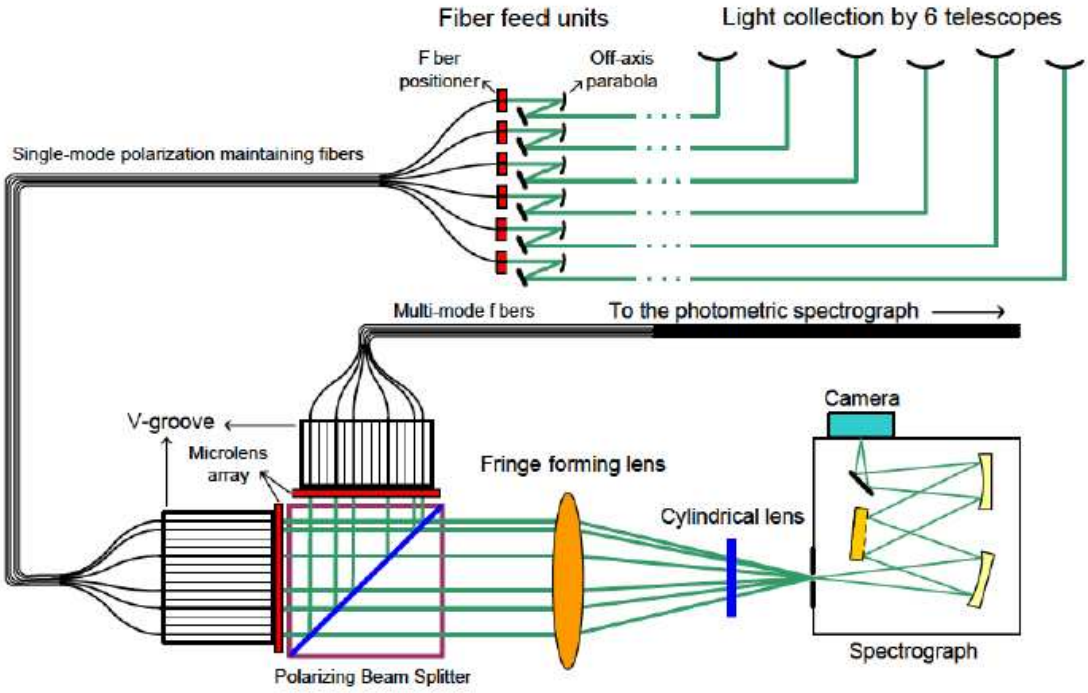


Figure 1. Schematic layout of VISION.

Figure 21: A diagram of light path for the VISION beam combiner. Light from up to six telescopes is coupled to single-mode polarization-maintaining fibers via off-axis parabolas and picomotor fiber positioners. Beam 6 has not yet been commissioned due to observatory maintenance. The single-mode fibers are placed on a V-groove array to ensure unique fringe frequencies for each beam pair. Finally, the light from each beam is split by a polarizing beam splitter: 50% is transmitted and focused onto the fringing camera, which records the interferograms, and 50% is reflected by the polarizing beam splitter and focused onto the photometric camera, which monitors real-time fluxes of each beam for visibility and triple amplitude calibration.

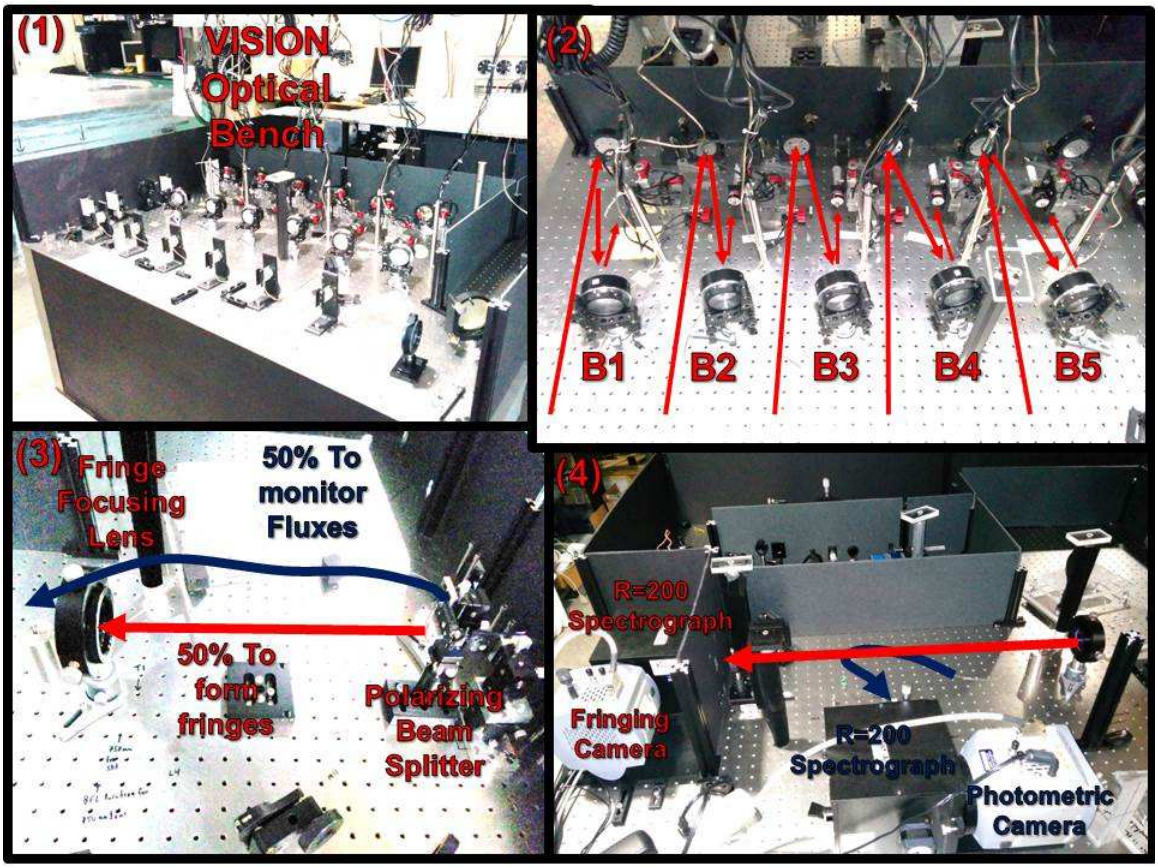


Figure 22: The light path through the VISION beam combiner. (1) The entire VISION optical bench. (2) Each 35 mm diameter beam is collapsed to a $4-8$ $\mu$m spot size, focused onto each single-mode fiber tip held in place by a fiber positioner. (3) The light from each single-mode fiber is positioned on a V-groove array, where 50% is sent to the photometric camera via multi-mode fibers and 50% is sent to the fringing camera after passing through a fringe focusing lens and cylindrical lens. The photometric and fringing cameras and the identical $R = 200$ spectrographs attached to these cameras are shown in (4).

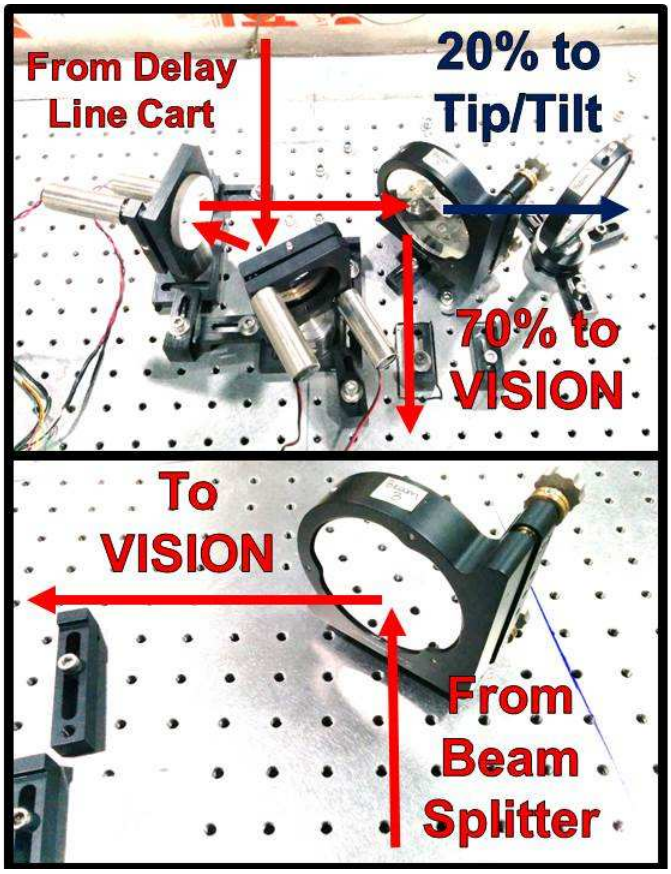


Figure 23: The light path towards the VISION beam combiner. (TOP) A minority (20%) of the light passes through the beam splitter in transmission to the tip/tilt mirrors for 1st order correction of the atmospheric turbulence. The majority (70%) of the light is reflected towards VISION. (BOTTOM) The light is re-routed towards the VISION beam combiner.

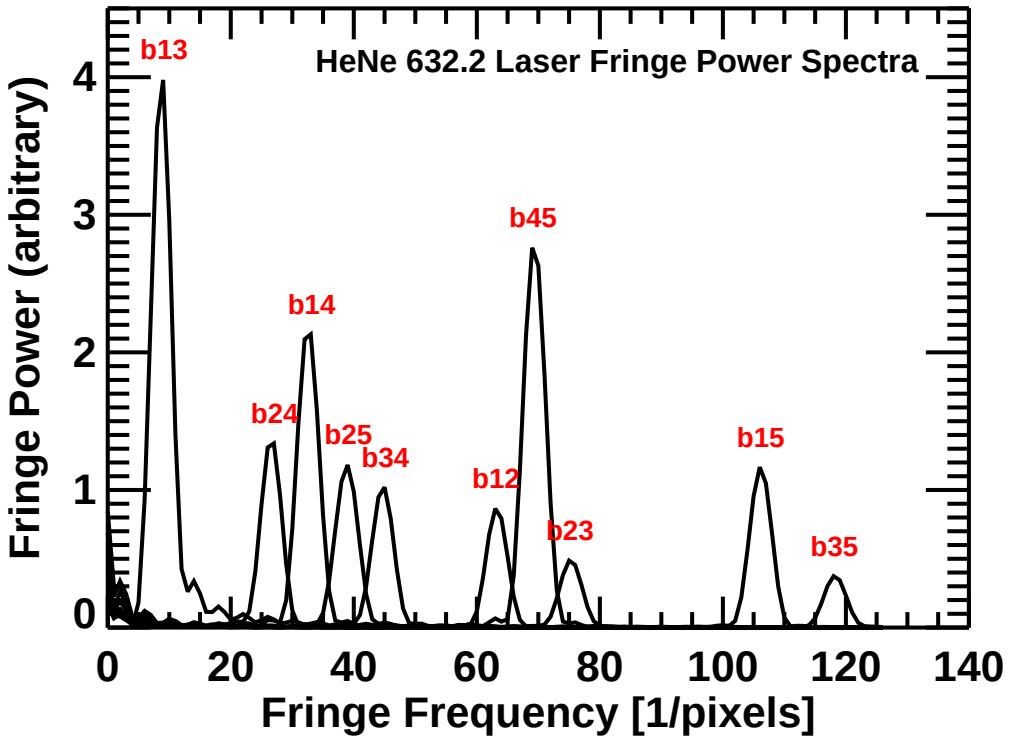


Figure 24: The unique fringe frequencies for each beam pair combination for beams 1-5 for VISION as measured using an in-laboratory 632.8 nm HeNe laser source. At fixed wavelength, the fringe frequency increases with increased distance between the fibers on the V-groove array. The peaks in the power spectra for each beam pair are well isolated resulting in very low cross talk between the fringes. The label bAB is the power spectrum peak for a fringe resulting from combining beams A and B.

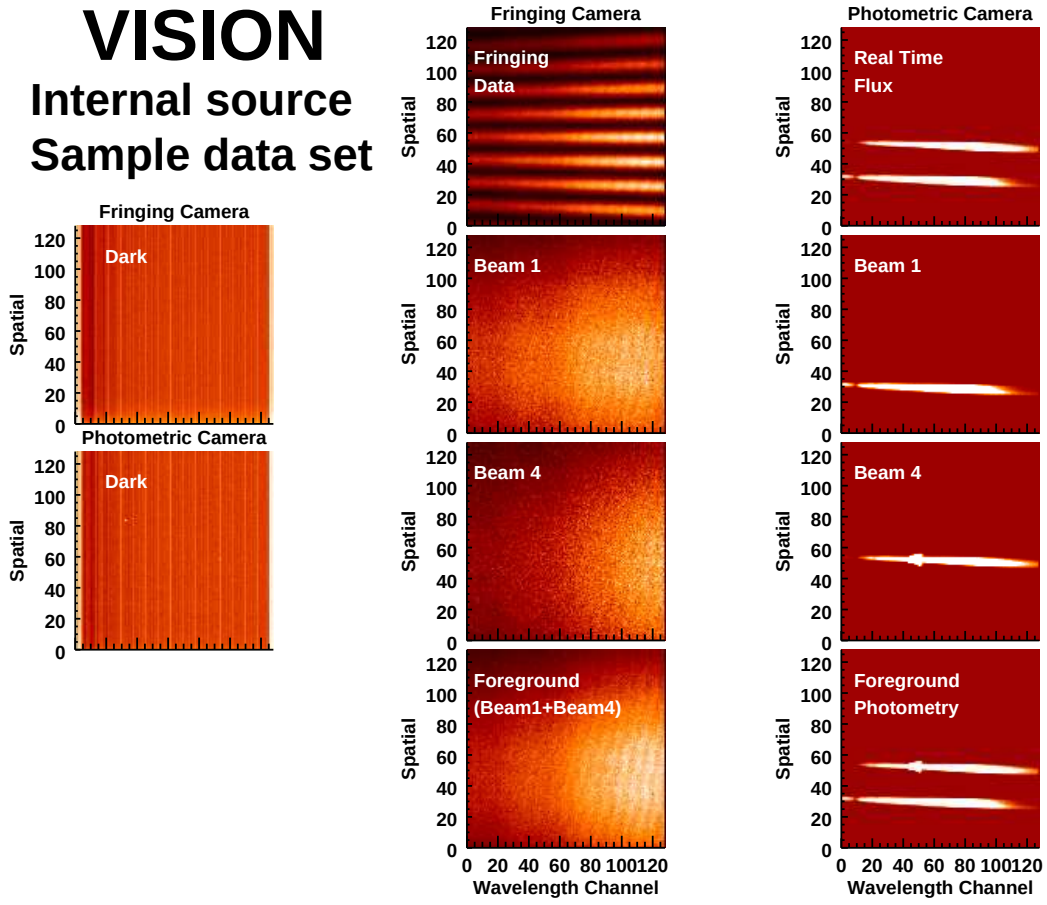


Figure 25: Sample VISION data set using an laboratory white light source with an $R = 1000$ spectrograph. A complete VISION data set to measure visibilities and closure phases includes (1) an average dark frame for both the fringing and photometric cameras to characterize the bias count structure across the EMCCDs, (2) the fringing data and simultaneous real-time flux measurements, (3) frames with light from each beam individually on the fringing and photometric cameras to measure the split of the light from the polarizing beam splitter, and (4) the foreground data to characterize the bias in the power spectrum (visibility bias) and the bispectrum. The small fringing seen in the foreground data is due to pixel-to-pixel sensitivity of the EMCCD chips. This pixel-to-pixel sensitivity only appears strongly after averaging at least 10 minutes of frames. The small point sources of light on the photometric camera frames are due to leakage of the laser metrology used by the delay line carts onto the EMCCDs.

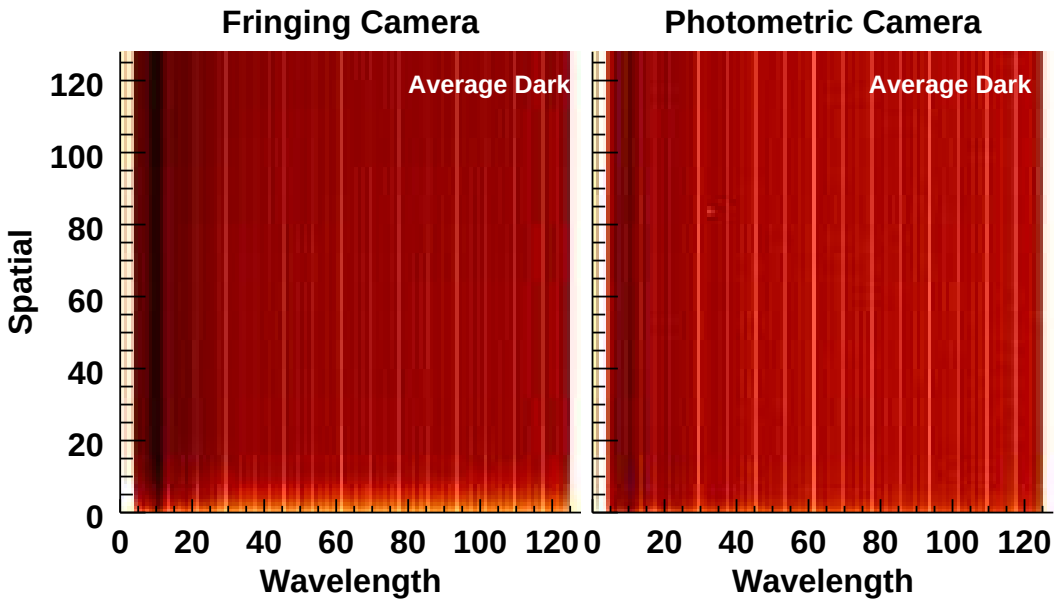


Figure 26: Thirty second time-averaged darks on the fringing and photometric cameras. There are variable bias counts across each EMCCD that must be subtracted off for each VISION data set. The maximum, median, and minimum for the average fringing camera dark are $\approx 87$, $\approx 91$ and $\approx 107$ counts respectively. The maximum, median, and minimum for the average photometric camera dark are $\approx 97$, $\approx 99$ and $\approx 109$ counts respectively.

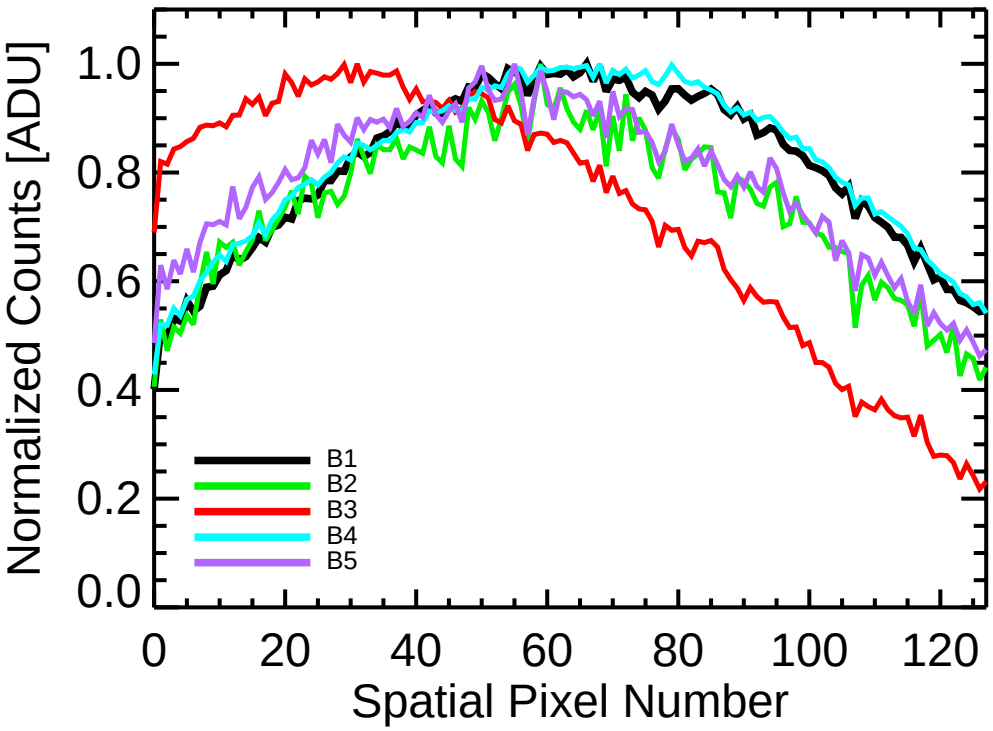


Figure 27: The wavelength averaged ($550 - 850$ nm) shape of the Gaussian beam profile outputs from the single mode fibers on the fringing camera (see §4.5.2). All five beams overlap well. A Gaussian shape is expected for the $LP_{01}$ mode of electric field that propagates through each single-mode fiber used for VISION. Beam 3 is offset from the center of fringing camera chip due the single mode fiber being slighlty misplaced in the V-groove array.

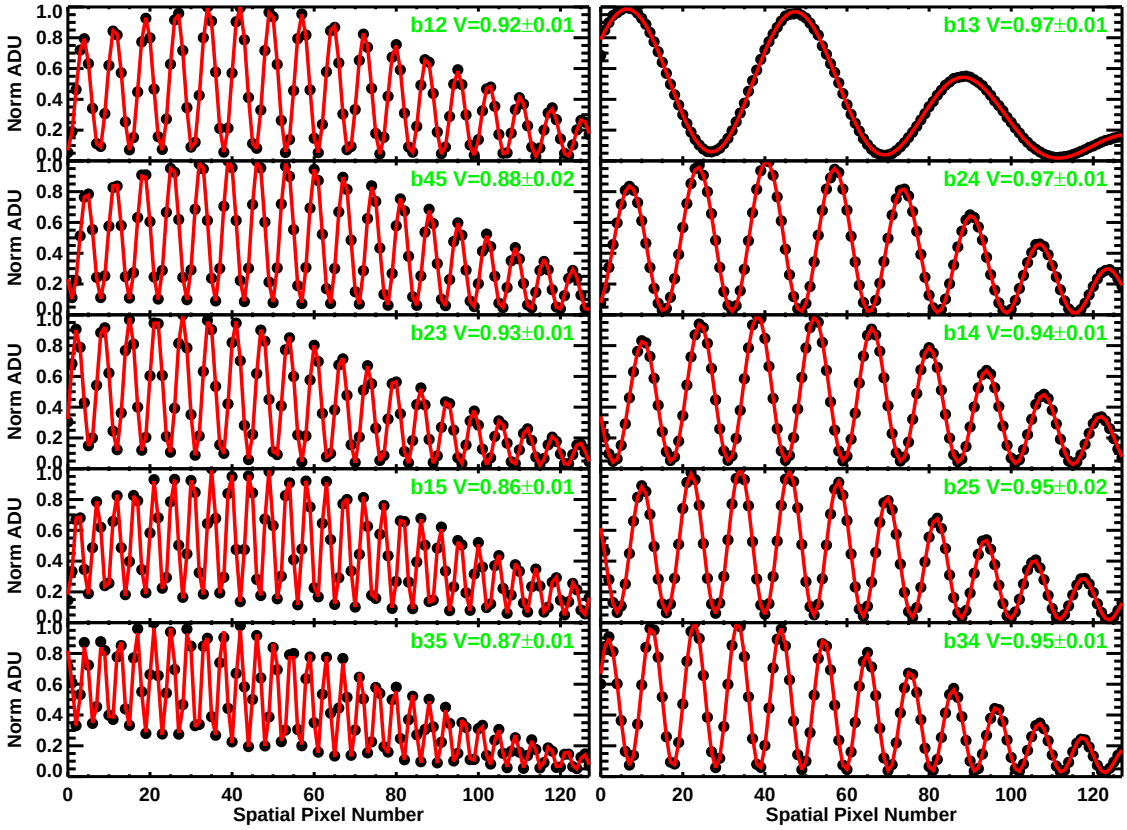


Figure 28: Interferograms using a 632.8 nm HeNe laser source and matched light paths for each beam pair for beams 1-5 (see §4.5.3). A fringe model was fit to each set of laser fringes for each beam pair using the fringe model Equation 20, and measure visibilities of 85-97%, which implies that the majority of light is interfering. The small visibility loss could be the result of polarization effects, beam intensity mismatch.

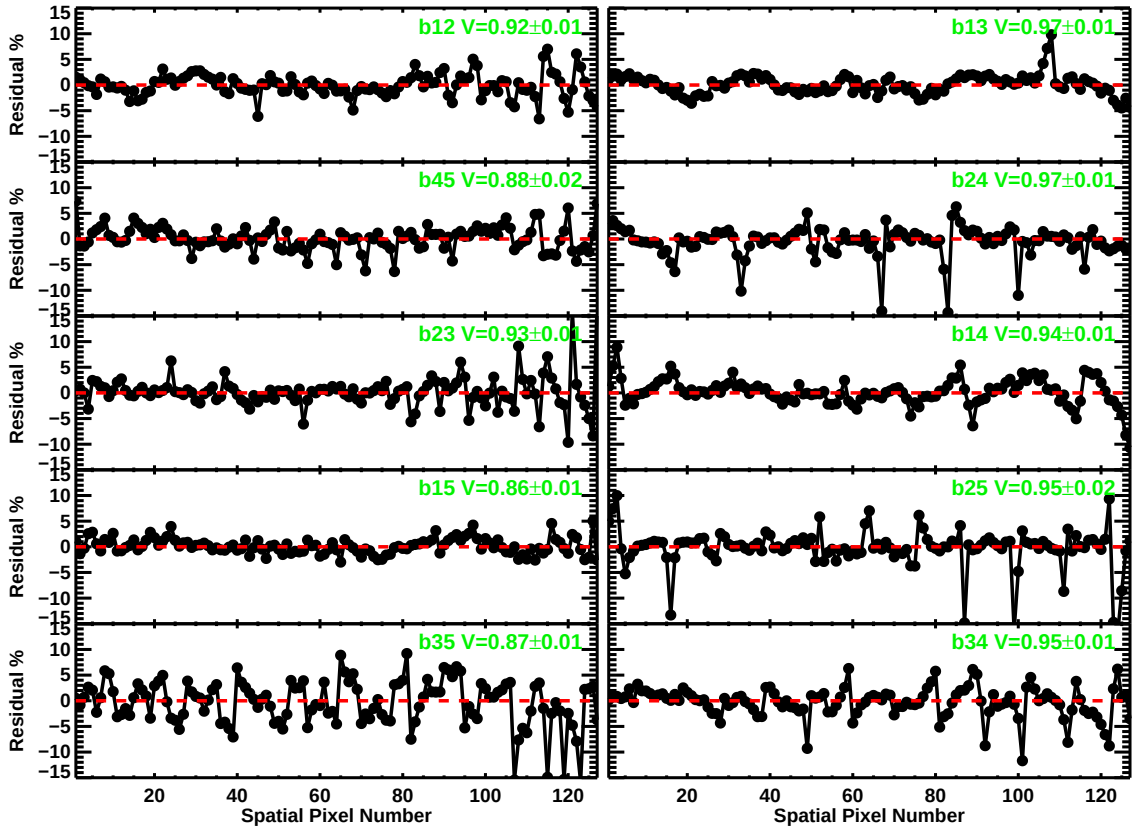


Figure 29: The residuals for figure 28.

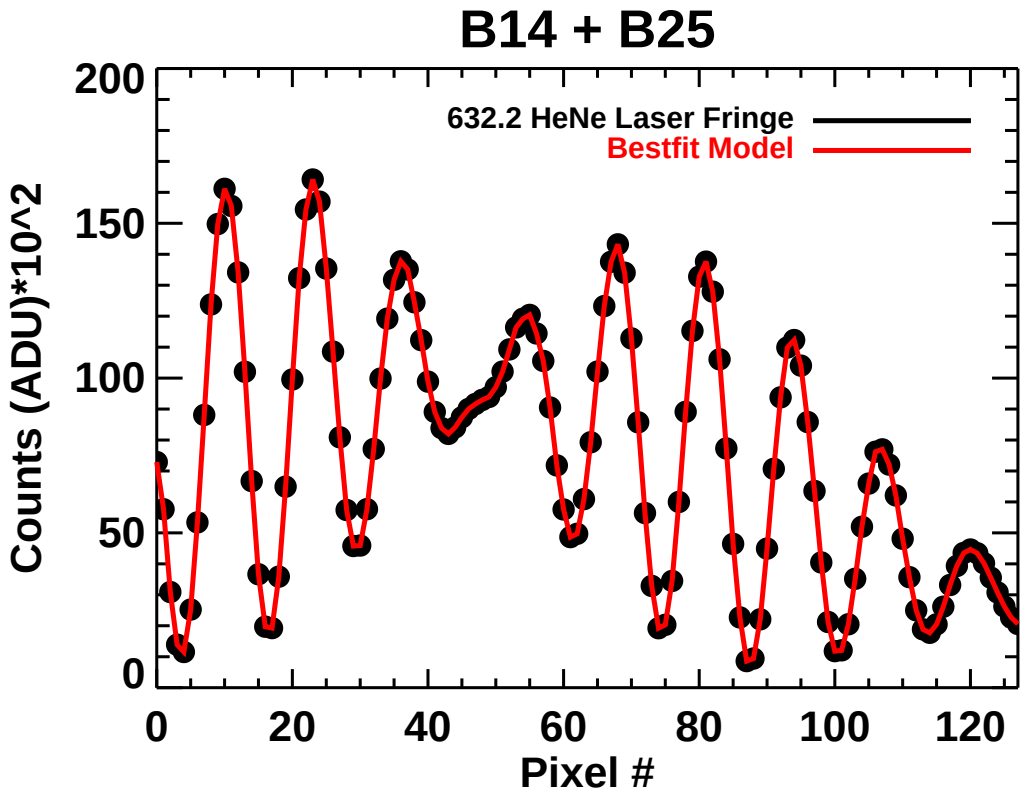


Figure 30: Laser fringe data from beam pair 1-4 and 2-5 added together on the detector, with the corresponding best fit model using Equation 18 in §4.5.4.

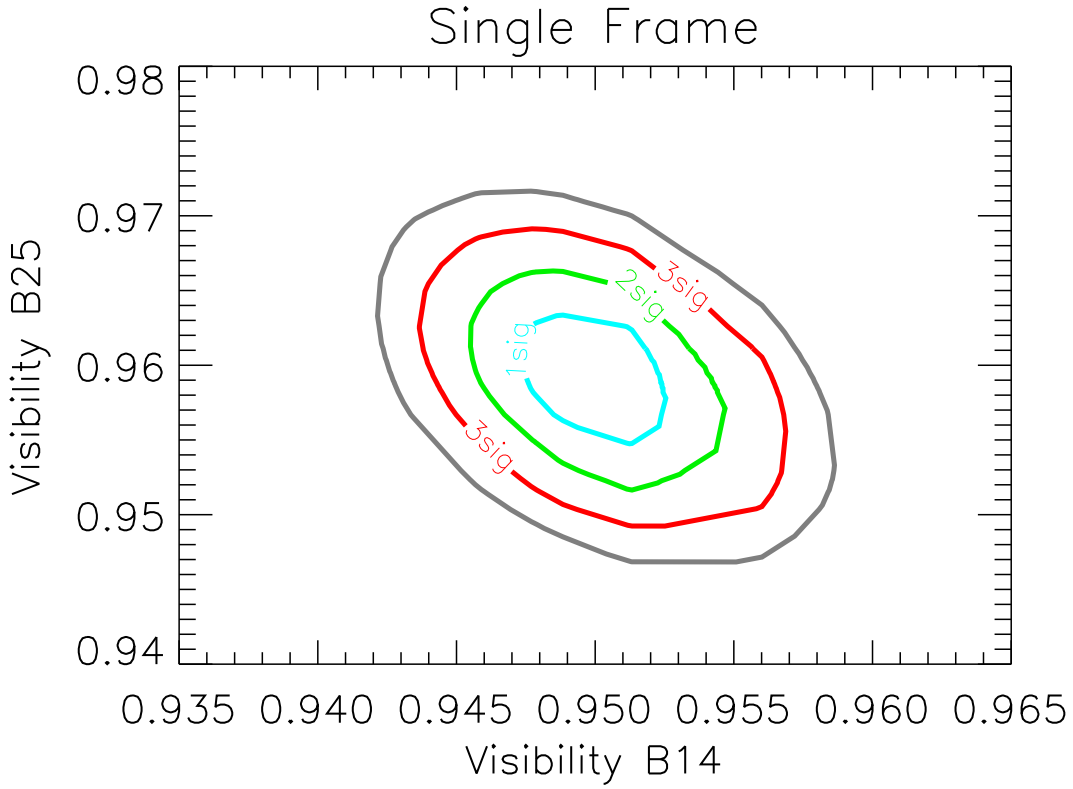


Figure 31: A map of $\chi^2$ space for the correlation between the visibility of beam pair 1-4 and beam pair 2-5, using co-added laser fringes. The confidence intervals correspond to $\Delta\chi^2 = \chi^2 - \chi^2_{\rm min} = 2.30$, 6.17 and 11.8 for $1\sigma$, $2\sigma$ and $3\sigma$ respectively for 2 parameters of interest (see §4.5.4, and also Press et al., 2002). The visibility parameters for either beam pair are correlated on the $\approx 2\%$ level for the $3\sigma$ confidence interval even for these very high signal-to-noise laser fringes. This suggests crosstalk is inherent to the instrument set up.

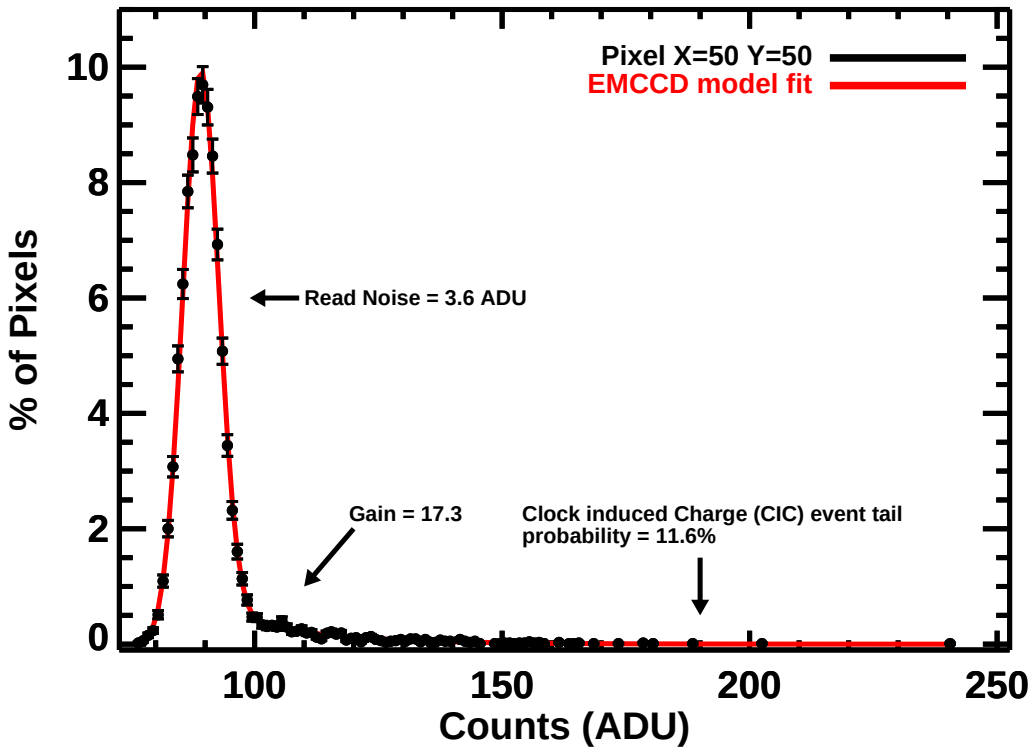


Figure 32: Sample fit to a histogram of a time series of $\approx 10^5$ dark frames for pixel $(50, 50)$, (black circles). The gain, read noise, and clock induced charge rate are derived by fitting an analytic EMCCD model to the data (red line). The analytic EMCCD model (see §4.6.1) is the convolution of the probability that a pixel only has read noise, or has read noise and a clock induced charge event.

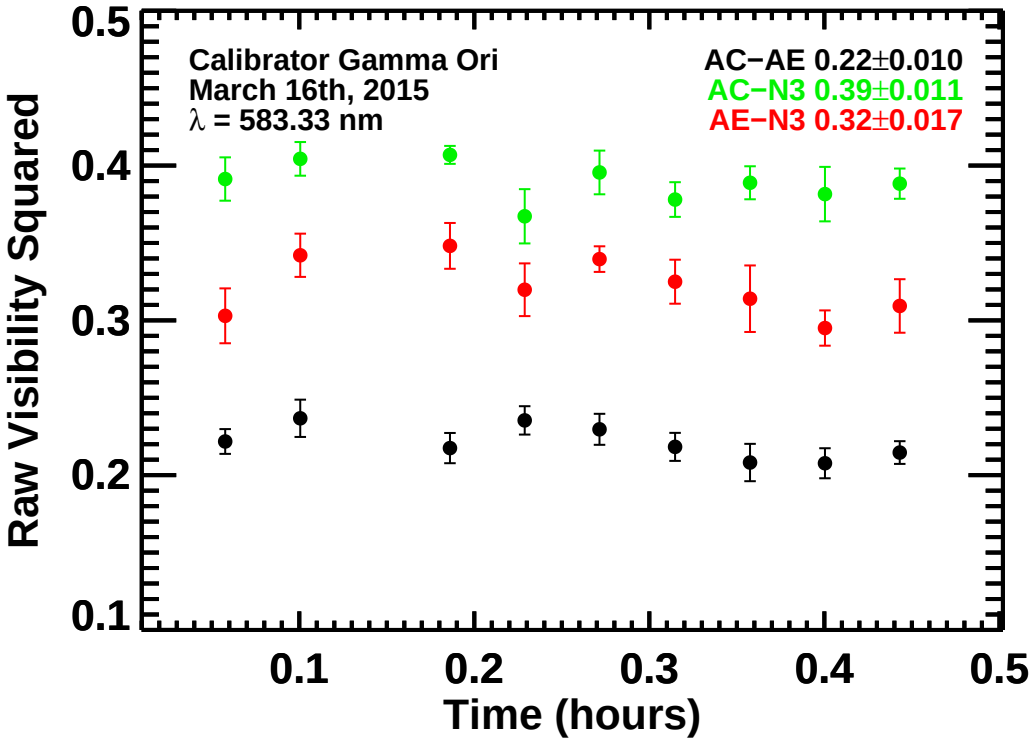


Figure 33: Beam intensity mismatch corrected squared visibilities vs time for observations of calibrator $\gamma$ Orionis during commissioning on March 16th, 2015 with stations AC, AE and N3. The system visibility drift is at max $0.01 - 0.02$ over half an hour for $\gamma$ Orionis.

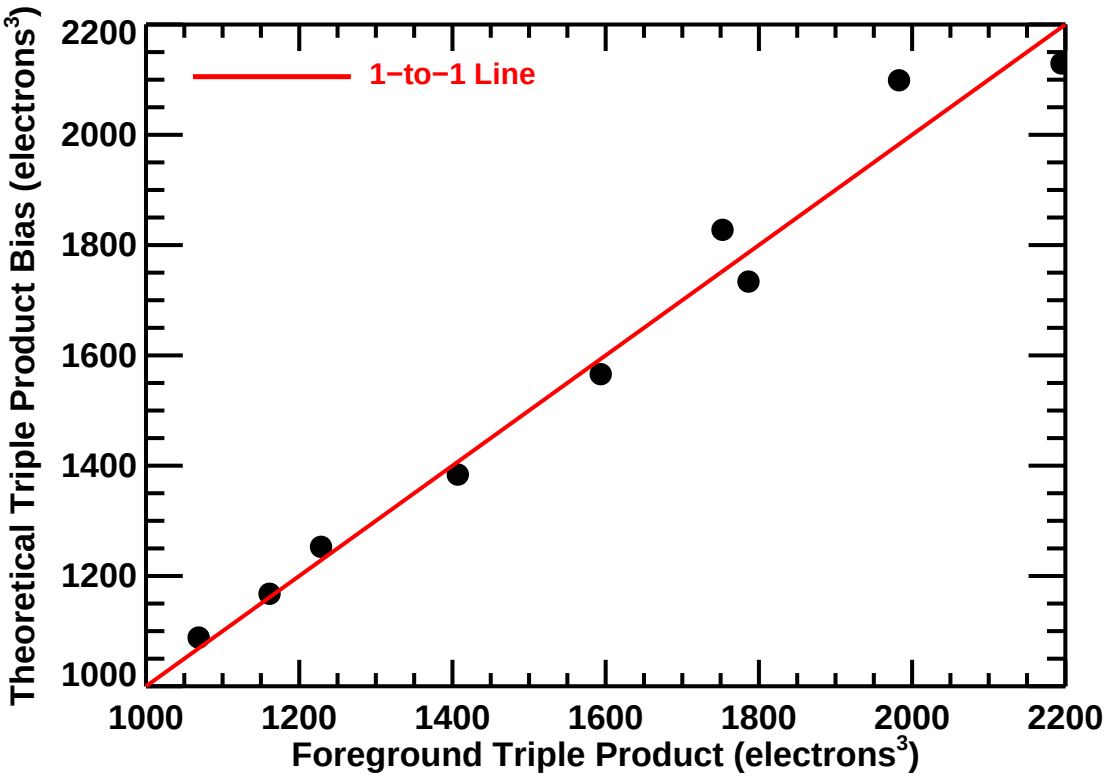


Figure 34: Triple Product Bias

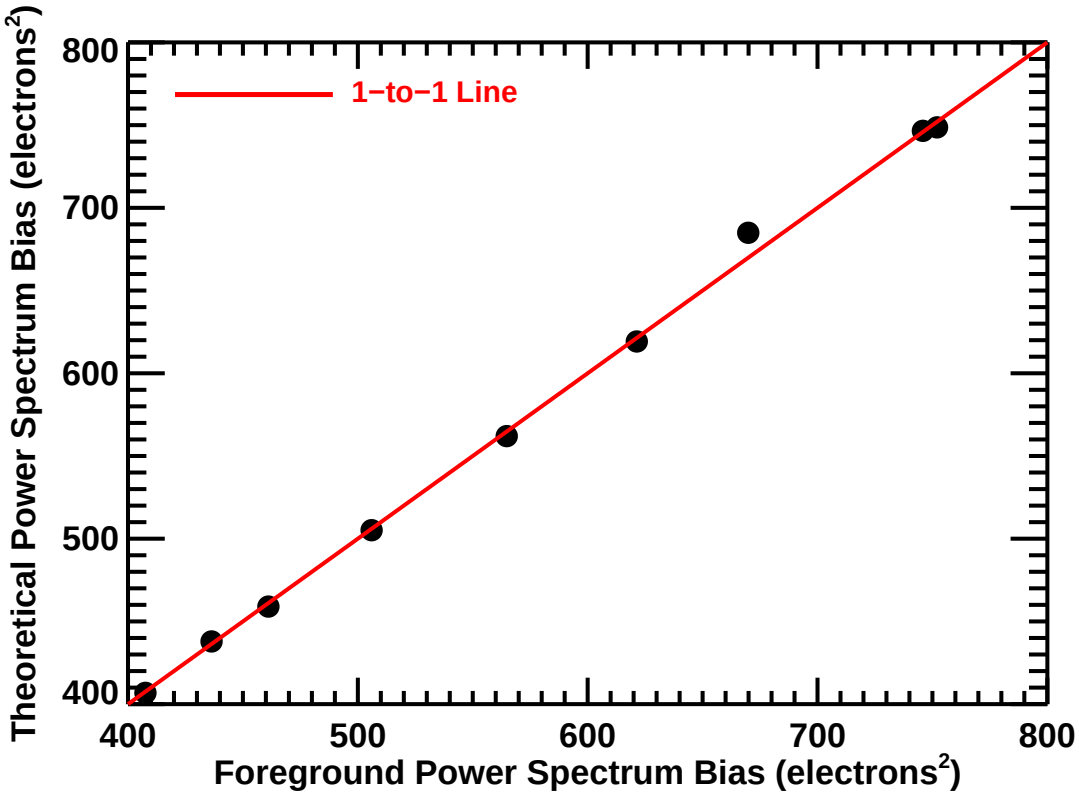


Figure 35: Power Spectrum Bias . The theoretical bispectrum and power spectrum bias match the amplitude of foreground bispectrum and foreground power spectrum for $\gamma$ Orionis, further verifying that the bias correction procedures in the data-processing pipeline are accurate. The foreground amplitude of the bispectrum and power spectrum were averaged over 15.36 seconds, using 6 ms exposure times.

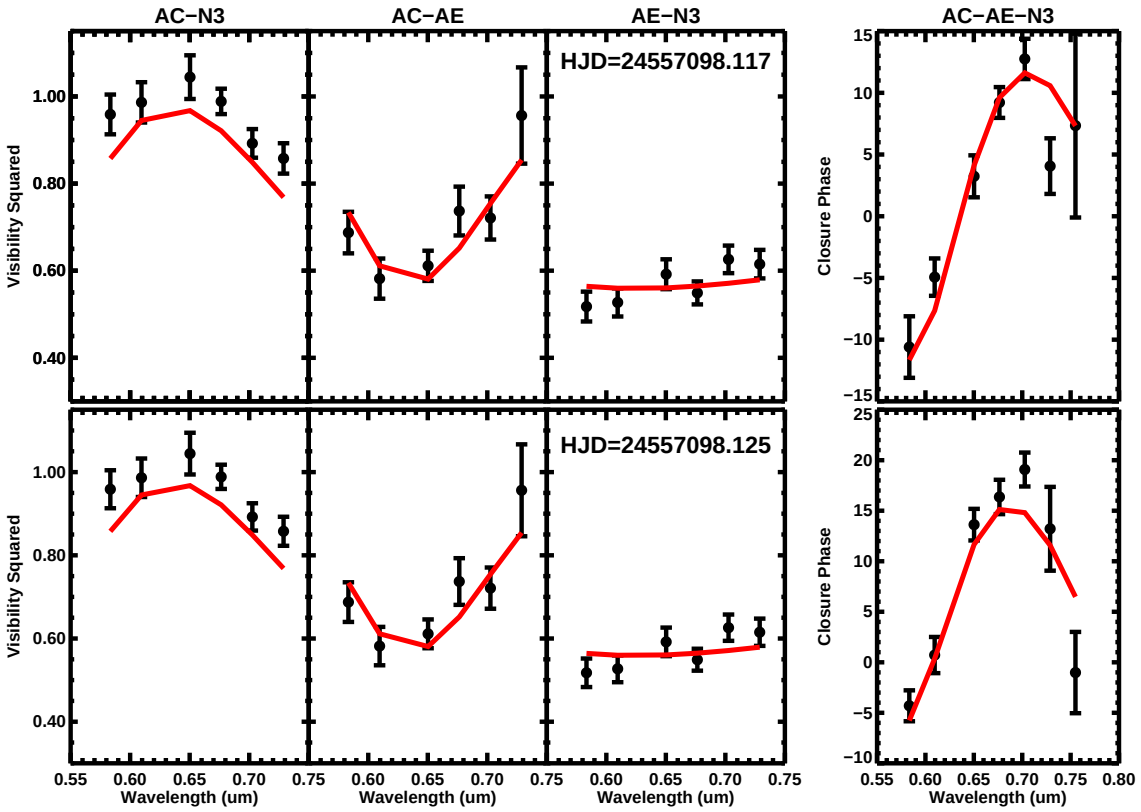


Figure 36: Sample calibrated squared visibilities and closure phase observations of $\zeta$ Orionis on UT 03152016 at two different times of the night. The red solid line is the best fit model to the data. the best fit model for this binary star at the epoch the observations yields a separation of $40.6 \pm 1.8$ mas, a position angle of $223.9 \pm 1.0°$ for observations from $580 - 750$ nm, in good agreement with the predicted separation of $40.1 \pm 1.0$ mas and position angle $223.2 \pm 2.3$ mas from Hummel et al. (2013). The observed flux ratio of $2.18 \pm 0.13$ mag is also in good agreement with the flux ratio $2.2 \pm 0.1$ mag from Hummel et al. (2013). The AC-N3 visibilities have a small bias likely due possibly to imperfect photometric calibration.

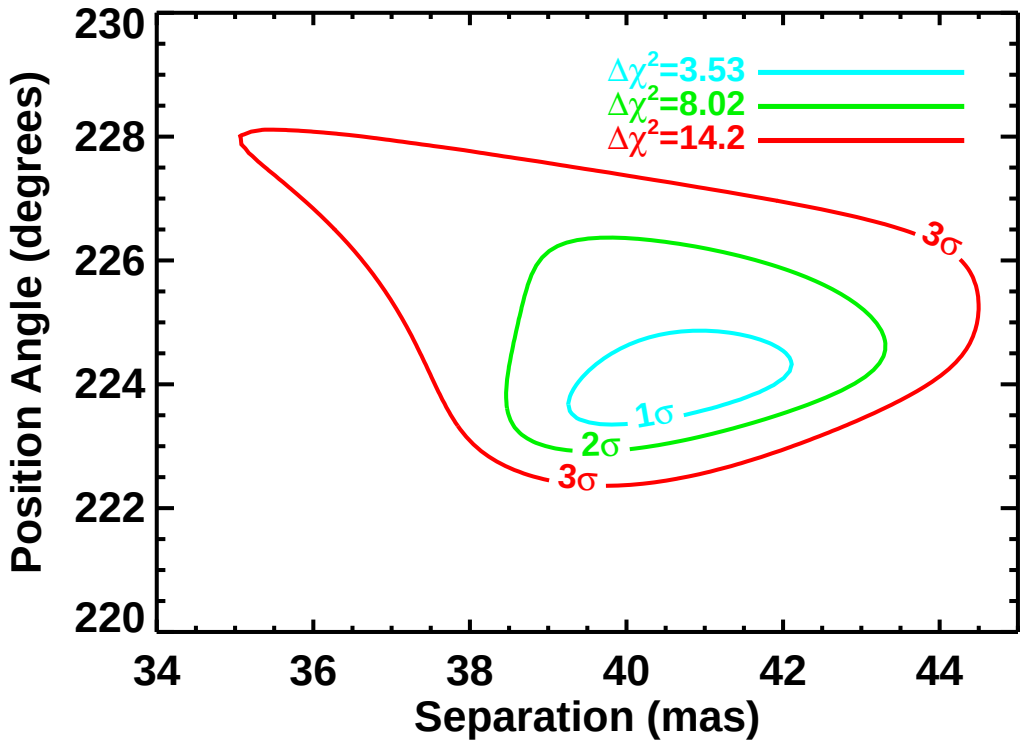


Figure 37: Confidence intervals for $1\sigma$ (blue line), $2\sigma$ (green line) and $3\sigma$ (red line) errors on the separation and position angle corresponding to $\Delta\chi^2 = \chi^2 - \chi^2_{\rm min}$ of 3.53, 8.02 and 14.03 respectively for 3 parameters of interest (Press et al., 2002). The minimum $\chi^2_{\rm min}$ corresponds to the best fit model (red solid line) in Figure 36.

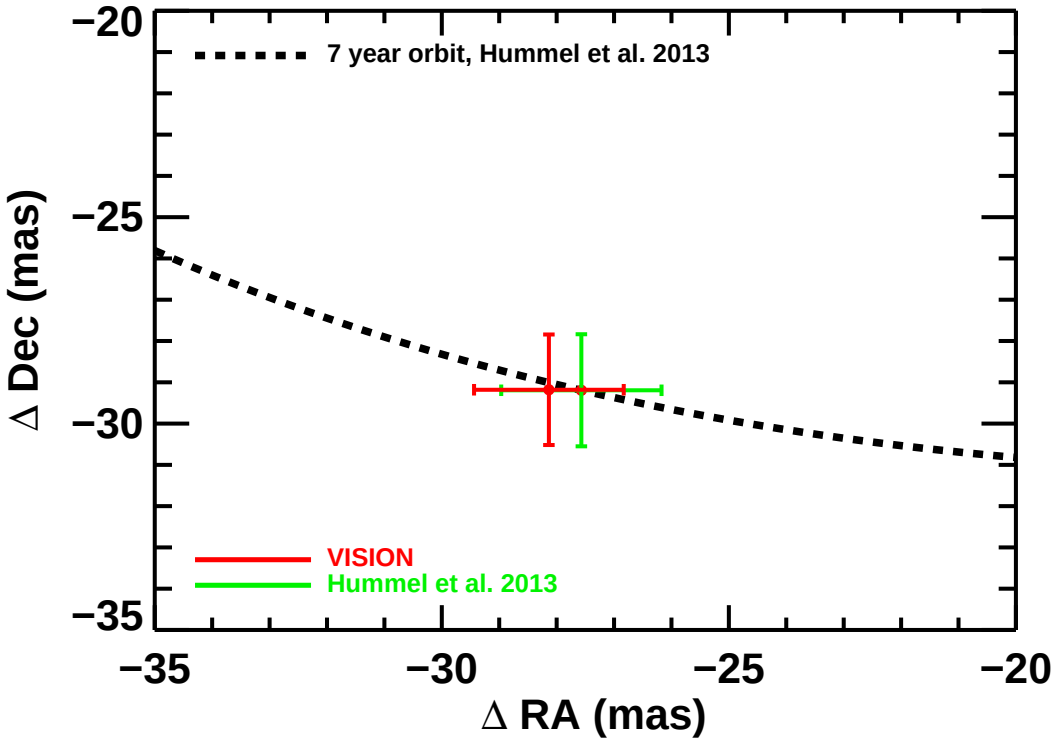


Figure 38: The observed position angle and separation for the binary $\zeta$ Orionis A (red) match the known orbit Hummel et al. (2013) (black line). The errors on the predicted $\Delta$RA and $\Delta$Dec (green) was calculated from the error on the orbital elements from Hummel et al. (2013).

# REFERENCES


Armstrong, J. T., Mozurkewich, D., Pauls, T. A., & Hajian, A. R. 1998, Proc. SPIE, 3350, 461

Armstrong, J. T., Mozurkewich, D., Rickard, L. J., et al. 1998, ApJ, 496, 550

Armstrong, J. T., Nordgren, T. E., Germain, M. E., et al. 2001, AJ, 121, 476

Armstrong, J. T., Jorgensen, A. M., Neilson, H. R., et al. 2012, Proc. SPIE, 8445, 84453K

Baines, E. K., Armstrong, J. T., & van Belle, G. T. 2013, ApJ, 771, L17

Baines, E. K., Armstrong, J. T., Schmitt, H. R., et al. 2014, ApJ, 781, 90

Baron, F., Monnier, J. D., Kiss, L. L., et al. 2014, ApJ, 785, 46

Basden, A. G., & Haniff, C. A. 2004, MNRAS, 347, 1187

Bazot, M., Ireland, M. J., Huber, D., et al. 2011, A&A, 526, L4

Berger, J.-P., Haguenauer, P., Kern, P. Y., et al. 2003, Proc. SPIE, 4838, 1099

Born, M., & Wolf, E. 1999, Principles of Optics, by Max Born and Emil Wolf and With contributions by A. B. Bhatia and P. C. Clemmow and D. Gabor and A. R. Stokes and A. M. Taylor and P. A. Wayman and W. L. Wilcock, pp. 986. ISBN 0521642221. Cambridge, UK: Cambridge University Press, October 1999.

Challouf, M., Nardetto, N., Mourard, D., et al. 2014, A&A, 570, A104

Che, X., Monnier, J. D., Zhao, M., et al. 2011, ApJ, 732, 68

Chiavassa, A., Plez, B., Josselin, E., & Freytag, B. 2009, A&A, 506, 1351

Chiavassa, A., Haubois, X., Young, J. S., et al. 2010, A&A, 515, A12

Chiavassa, A., Pasquato, E., Jorissen, A., et al. 2011, A&A, 528, A120

Chiavassa, A., Bigot, L., Kervella, P., et al. 2012, A&A, 540, A5

Coudé du Foresto, V., Ridgway, S., & Mariotti, J.-M. 1997, A&AS, 121, 379

Davis, J., Tango, W. J., Booth, A. J., et al. 1999, MNRAS, 303, 773

Davis, J., Tango, W. J., Booth, A. J., Thorvaldson, E. D., & Giovannis, J. 1999, MNRAS, 303, 783

Domiciano de Souza, A., Kervella, P., Jankov, S., et al. 2003, A&A, 407, L47

Domiciano de Souza, A., Hadjara, M., Vakili, F., et al. 2012, A&A, 545, A130

Ducati, J. R. 2002, VizieR Online Data Catalog, 2237, 0

Espinosa Lara, F., & Rieutord, M. 2011, A&A, 533, A43

Espinosa Lara, F., & Rieutord, M. 2013, A&A, 552, A35

Freytag, B., Höfner, S. 2008, A&A, 483, 571

Freytag, B., Steffen, M., & Dorch, B. 2002, Astronomische Nachrichten, 323, 213

The design and implementation of FFTW3.Proceedings of the IEEE, 93(2):216?231, 2005. Special issue on “Program Generation, Optimization, and Platform Adaptation.?

Ghasempour, A., Muterspaugh, M. W., Hutter, D. J., et al. 2012, Proc. SPIE, 8445, 84450M

Gordon, J. A., & Buscher, D. F. 2012, A&A, 541, A46

Harpsøe, K. B. W., Jørgensen, U. G., Andersen, M. I., & Grundahl, F. 2012, A&A, 542, A23

Haubois, X., Perrin, G., Lacour, S., et al. 2009, A&A, 508, 923

Huber, D., Ireland, M. J., Bedding, T. R., et al. 2012, ApJ, 760, 32

Huber, D., Ireland, M. J., Bedding, T. R., et al. 2012, MNRAS, 423, L16

Hummel, C. A., Mozurkewich, D., Armstrong, J. T., et al. 1998, AJ, 116, 2536

Hummel, C. A., Carquillat, J.-M., Ginestet, N., et al. 2001, AJ, 121, 1623

Hummel, C. A., Benson, J. A., Hutter, D. J., et al. 2003, AJ, 125, 2630

Hummel, C. A., Rivinius, T., Nieva, M.-F., et al. 2013, A&A, 554, A52

Ireland, M. J., Mérand, A., ten Brummelaar, T. A., et al. 2008, Proc. SPIE, 7013, 701324

Jamialahmadi, N., Berio, P., Meilland, A., et al. 2015, A&A, 579, A81

Jorgensen, A. M., Mozurkewich, D., Schmitt, H., et al. 2006, Proc. SPIE, 6268, 62681H

Jorgensen, A. M., Mozurkewich, D., & Hutter, D. 2014, Resolving The Future Of Astronomy With Long-Baseline Interferometry, 487, 303

Kloppenborg, B. K., Stencel, R. E., Monnier, J. D., et al. 2015, ApJS, 220, 14

Kok, Y., Ireland, M. J., Tuthill, P. G., et al. 2012, Proc. SPIE, 8445, 844521

Landavazo, M. I., Jorgensen, A. M., Sun, B., et al. 2014, Proc. SPIE, 9146, 914621

Maestro, V., Kok, Y., Huber, D., et al. 2012, Proc. SPIE, 8445, 84450G

Maestro, V., Che, X., Huber, D., et al. 2013, MNRAS, 434, 1321

Markwardt, C. B. 2009, Astronomical Data Analysis Software and Systems XVIII, 411, 251

Monnier, J. D., Berger, J.-P., Millan-Gabet, R., & ten Brummelaar, T. A. 2004, Proc. SPIE, 5491, 1370

Monnier, J. D., Pedretti, E., Thureau, N., et al. 2006, Proc. SPIE, 6268, 62681P

Monnier, J. D., Zhao, M., Pedretti, E., et al. 2007, Science, 317, 342

Monnier, J. D., Che, X., Zhao, M., et al. 2012, ApJ, 761, L3

Mourard, D., Perraut, K., Bonneau, D., et al. 2008, Proc. SPIE, 7013, 701323

Mourard, D., Clausse, J. M., Marcotto, A., et al. 2009, A&A, 508, 1073

Mourard, D., Bério, P., Perraut, K., et al. 2011, A&A, 531, A110

Mourard, D., Challouf, M., Ligi, R., et al. 2012, Proc. SPIE, 8445, 84450K

Mozurkewich, D. 1994, Proc. SPIE, 2200, 76

Muterspaugh, M. W., Lane, B. F., Konacki, M., et al. 2005, AJ, 130, 2866

Muterspaugh, M. W., Lane, B. F., Konacki, M., et al. 2006, A&A, 446, 723

Muterspaugh, M. W., Lane, B. F., Konacki, M., et al. 2006, ApJ, 636, 1020

Muterspaugh, M. W., Lane, B. F., Kulkarni, S. R., et al. 2006, ApJ, 653, 1469

Muterspaugh, M. W., Lane, B. F., Fekel, F. C., et al. 2008, AJ, 135, 766

Muterspaugh, M. W., Fekel, F. C., Lane, B. F., et al. 2010, AJ, 140, 1646

North, J. R., Tuthill, P. G., Tango, W. J., & Davis, J. 2007, MNRAS, 377, 415

North, J. R., Davis, J., Robertson, J. G., et al. 2009, MNRAS, 393, 245

Ohishi, N., Nordgren, T. E., & Hutter, D. J. 2004, ApJ, 612, 463

Patience, J., Zavala, R. T., Prato, L., et al. 2008, ApJ, 674, L97

Peterson, D. M., Hummel, C. A., Pauls, T. A., et al. 2006, Nature, 440, 896

Petrov, R. G., Malbet, F., Weigelt, G., et al. 2007, A&A, 464, 1

Press, W. H., Teukolsky, S. A., Vetterling, W. T., & Flannery, B. P. 2002, Numerical recipes in C++ : the art of scientific computing by William H. Press. xxviii, 1,002 p. : ill. ; 26 cm. Includes bibliographical references and index. ISBN : 0521750334,

Ragland, S., Traub, W. A., Berger, J.-P., et al. 2004, Proc. SPIE, 5491, 1390

Roettenbacher, R. M., Monnier, J. D., Henry, G. W., et al. 2015, ApJ, 807, 23

Roettenbacher, R., Monnier, J., Korhonen, H., et al. 2015, IAU General Assembly, 22, 57063

Rousselet-Perraut, K., Stadler, E., Feautrier, P., et al. 1999, Working on the Fringe: Optical and IR Interferometry from Ground and Space, 194, 344

Rousselet-Perraut, K., Haguenauer, P., Petmezakis, P., et al. 2000, Proc. SPIE, 4006, 1042

Schmitt, H. R., Pauls, T. A., Tycner, C., et al. 2009, ApJ, 691, 984

Shaklan, S., & Roddier, F. 1988, Appl. Opt., 27, 2334

Shaklan, S. B., Colavita, M. M., & Shao, M. 1992, European Southern Observatory Conference and Workshop Proceedings, 39, 1271

Sun, B., Jorgensen, A. M., Landavazo, M., et al. 2014, Proc. SPIE, 9146, 914620

Tango, W. J., Davis, J., Jacob, A. P., et al. 2009, MNRAS, 396, 842

ten Brummelaar, T. A., McAlister, H. A., Ridgway, S. T., et al. 2005, ApJ, 628, 453

Traub, W. A., Berger, J.-P., Brewer, M. K., et al. 2004, Proc. SPIE, 5491, 482

van Belle, G. T. 2012, A&A Rev., 20, 51

Wang, X., Hummel, C. A., Ren, S., & Fu, Y. 2015, AJ, 149, 110

Wenger, M., Ochsenbein, F., Egret, D., et al. 2000, A&AS, 143, 9

White, T. R., Huber, D., Maestro, V., et al. 2013, MNRAS, 433, 1262

Wirnitzer, B. 1985, Journal of the Optical Society of America A, 2, 14

Wittkowski, M., Hummel, C. A., Aufdenberg, J. P., & Roccatagliata, V. 2006, A&A, 460, 843

Zavala, R. T., Hummel, C. A., Boboltz, D. A., et al. 2010, ApJ, 715, L44

Zhang, X., Armstrong, J. T., Clark, J. A., III, et al. 2006, Proc. SPIE, 6268, 62683V

Zhao, M., Gies, D., Monnier, J. D., et al. 2008, ApJ, 684, L95